creative commons
COMMONS DEED

저작자표시-비영리-변경금지 2.0 대한민국

이용자는 아래의 조건을 따르는 경우에 한하여 자유롭게

- 이 저작물을 복제, 배포, 전송, 전시, 공연 및 방송할 수 있습니다.

다음과 같은 조건을 따라야 합니다:

저작자표시. 귀하는 원저작자를 표시하여야 합니다.

비영리. 귀하는 이 저작물을 영리 목적으로 이용할 수 없습니다.

변경금지. 귀하는 이 저작물을 개작, 변형 또는 가공할 수 없습니다.

- 귀하는, 이 저작물의 재이용이나 배포의 경우, 이 저작물에 적용된 이용허락조건을 명확하게 나타내어야 합니다.
- 저작권자로부터 별도의 허가를 받으면 이러한 조건들은 적용되지 않습니다.

저작권법에 따른 이용자의 권리는 위의 내용에 의하여 영향을 받지 않습니다.

이것은 이용허락규약(Legal Code)을 이해하기 쉽게 요약한 것입니다.

Disclaimer

dCollection

공학박사학위논문

Effects of Reinforcement on Ballistic Resistance of RC Targets

철근콘크리트 구조체의 방탄 성능에 철근보강이 미치는 영향

2023년 8월

서울대학교 대학원

건설환경공학부

안 진 호

Effects of Reinforcement on Ballistic Resistance of RC Targets

철근콘크리트 구조체의 방탄 성능에
철근보강이 미치는 영향

지도 교수 조 재 열

이 논문을 공학박사 학위논문으로 제출함
2023년 7월

서울대학교 대학원
건설환경공학부
안 진 호

안진호의 공학박사 학위논문을 인준함
2023년 7월

위 원 장 ______________________ (인)

부위원장 ______________________ (인)

위 원 ______________________ (인)

위 원 ______________________ (인)

위 원 ______________________ (인)

ABSTRACT

Effects of Reinforcement on Ballistic Resistance of RC Targets

Ahn, Jin-Ho

Department of Civil & Environmental Engineering

The Graduate School

Seoul National University

Reinforced concrete (RC) is a widely used construction material, renowned for its high strength and durability. Despite this, when subjected to high-velocity impacts, such as those from ballistic projectiles or blast loading, RC structures are prone to local failure. This can significantly damage their structural integrity, potentially leading to total failure. Therefore, understanding the failure behavior of RC structures under such impact loads is of critical importance.

The rebar ratio is one of the factors that affect the erosion behavior of RC targets. The rebar ratio refers to the proportion of rebar (reinforcing steel) in the RC target relative to the concrete. A higher rebar ratio is expected to result in higher resistance to local failure, as the rebar provides additional reinforcement to the concrete. The hardness of the projectile is another factor that affects the failure behavior of RC targets. An ogive-nose steel projectile is expected to cause more profound local failure than a soft-type projectile, as a projectile is a relatively minor projectile deformation after a collision.

In this study, a series of impact tests were performed on RC targets with different rebar ratios and impact velocities using ogive-nose steel projectile. The penetration depth, scabbing& perforation limit were measured and analyzed as a function of the rebar ran atio and impact velocity. The accuracy of existing empirical formulae recommended by various design standards for military and nuclear structures was verified using the results, and a modified empirical formula for predicting the penetration depth of RC targets subjected to impact loading was developed.

A total of 21 RC targets were tested in this study, with four different rebar ratios (0%, 1.6%, 2.5%, and 3.4%) and a constant target size of 600mm x 600mm x 500mm. The targets were made of normal-weight concrete with a compressive strength of 52 MPa. The rebar was made of high-strength steel with a yield strength of 470 MPa.

The impact tests were performed using a 60 mm single-stage gas gun in EPTC, in which an ogive-nose steel projectile was launched through helium gas pressure and collided with the RC target at the target speed. The impact velocity was varied from 550m/s to 850m/s in increments of 50m/s. The penetration depth, scabbing& perforation limit was measured after each impact test and recorded for analysis.

The results showed that the rebar ratio sig the local failure behavior of the RC targets. The targets with a higher rebar ratio (2.5% and 3.4%) showed less erosion than those with a lower rebar ratio (0% and 1.6%). The results also showed that the impact velocity sig the failure of the RC target, with higher impact velocities resulting in higher impact damage.

Based on the results, a modified empirical formula was suggested for predicting the impact damage of RC targets subjected to impact loading. The formula takes into account both the rebar ratio and impact velocity. Then, the validity of the proposed formula was verified by applying it to the existing experimental data of 153ea and FEA using the LS-Dyna program.

In conclusion, this study has investigated the impact response of reinforced concrete (RC) targets under various loading conditions, including different rebar ratios and striking velocities. The results have shown that the rebar ratio can significantly impact the RC target's response to impact loading. The modified empirical formula developed in this study provides a valuable tool for predicting the response of RC targets to impact loading. It can inform design and engineering decisions related to impact resistance.

Future work in this area could include further testing with a larger number of RC target specimens and developing more detailed numerical models better to understand the mechanisms of impact damage in RC targets. Additionally, it may be helpful to investigate the impact response of RC targets under more realistic loading conditions, such as those that incorporate dynamic loading and material nonlinearities.

Overall, this study has contributed to a deeper understanding of the impact response of RC targets and has provided valuable insights into the factors that can affect this response. This study's findings can inform the design and engineering of structures subjected to impact loading and ensure that these structures are adequately protected against impact damage.

Keywords: impact test, RC target, ballistic resistance, rebar ratio, ogive-nose steel projectile, modified empirical formula

Student Number: 2019-38662

TABLE OF CONTENTS

LIST OF TABLES

LIST OF FIGURES

NOTATIONS

Symbol	Definition and description
A	Cross-section area
A_{nose}	Area of surface of projectile nose
a	The maximum coarse aggregate size
c	Cracked-plastic boundary velocity
c_1	Elastic-cracked boundary velocity
d	Diameter of projectile
E	Elastic modulus of projectile
E_s	Elastic modulus of steel
f_c	Static compressive strength of concrete
f_t	Static tensile strength of concrete
f_y	Yield strength of reinforcing bar
h	Height of the projectile nose
h_{pen}	Depth of penetration
h_{per}	Depth of perforation limit
h_{scab}	Depth of scabbing limit
H	Thickness of the cone plug
H_0	Thickness of the concrete target
K	Bulk modulus
M	Mass of the projectile

N^*	Nose shape factor
P	Hydrostatic pressure
R_s	Radius of the projectile nose
S	Coefficient related to the slope of dynamic increase factor model
x	Current displacement of projectile
t	Time
V	Current velocity of projectile
V_0	Projectile impact velocity
V_c	Cavity expansion velocity
V_1	Velocity of projectile at the end of cratering zone
V_c	Cavity expansion velocity
γ	Dynamic increase factor
γ_{ACI349}	Dynamic increase factor of compressive strength in ACI 349-13
$\gamma_{ACI370R}$	Dynamic increase factor of compressive strength in ACI 370R-14
γ_{fib}	Dynamic increase factor of compressive strength in fib MC2010
γ_t	Dynamic increase factor of tensile strength
γ_y	Dynamic increase factor of yield strength of reinforcing bar
δ	Scaled damage measure in Karagozian and Case concrete model
δ_{ij}	Kronecker delta
$\dot{\varepsilon}$	Strain rate

η	Yield scale factor in Karagozian and Case concrete model
$\Delta\sigma$	Yield surface for deviatoric stresses
$\Delta\sigma_d$	Dynamic failure surface (or dynamic stress point)
$\Delta\sigma_s$	Static failure surface
λ	Damage function in Karagozian and Case concrete model
λ_m	Damage function value corresponding to $\eta = 1$
ν	Poisson's ratio
ξ	Non-dimensional variable of CET
σ	Stress matrix
σ_r	Radial stress in target medium
σ_θ	Hoop stress in target medium
σ_φ	Hoop stress in target medium
ρ	Current density of concrete
ρ_0	Initial density of concrete
ψ	Tensile-to-compressive meridian ratio in Karagozian and Case concrete model

1. Introduction

1.1. Research background

The protection of military facilities and social infrastructure against missile attacks and blast loads has long been a critical concern for defense planners and engineers. Reinforced concrete is commonly used for constructing such facilities due to its high strength, durability, and resistance to impact and blast loads. However, even reinforced concrete structures can suffer local damage when subjected to missile impacts or blast loads, which can compromise their performance and put the lives of military personnel at risk.

The local damage caused by missile impacts and blast loads can have a significant impact on the structural integrity and overall performance of structures. Extreme loadings, including impact and blast loadings, are characterized by their time-dependent nature and large amplitude, which are applied for a very short duration.

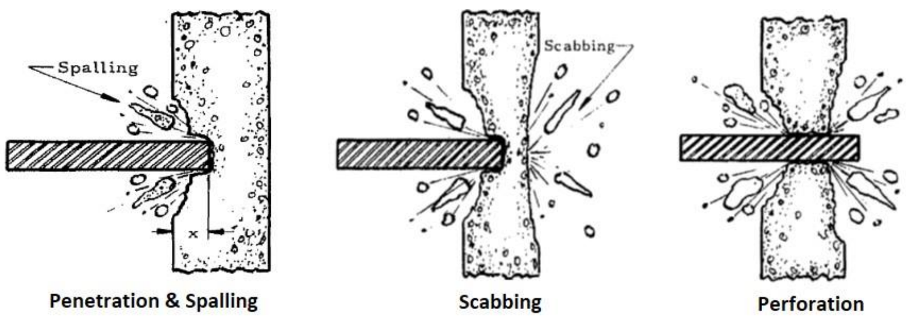

Figure 1.1 Projectile impact phenomena (Kennedy, 1976)

When a structure is subjected to extreme loading, it undergoes localized damage around the impact site and experiences general behavior, such as deflection. The failure modes for this localized damage include penetration, scabbing, and perforation, as shown in Figure 1.1.

Even if a structure does not collapse entirely, local effects such as scabbing can cause damage to its interior. Furthermore, perforation caused by projectiles entering the structure can also result in fragments of the structure becoming dislodged and potentially causing further damage, as shown in Figure 1.2.

Most facility standards that consider extreme events currently require structures to have sufficient wall thickness to prevent localized damage. In the case of the Korean military, the Defense Military Facilities Criteria (DMFC, 2017) recommends the use of experimentally based ACE (ACE, 1946) and Conwep (Hyde D, 1992) equations to predict the required wall thickness for design, as shown in Table 1.1. These equations estimate the penetration depth and determine the minimum wall thickness needed to prevent scabbing and perforation, the two limits considered in the design process.

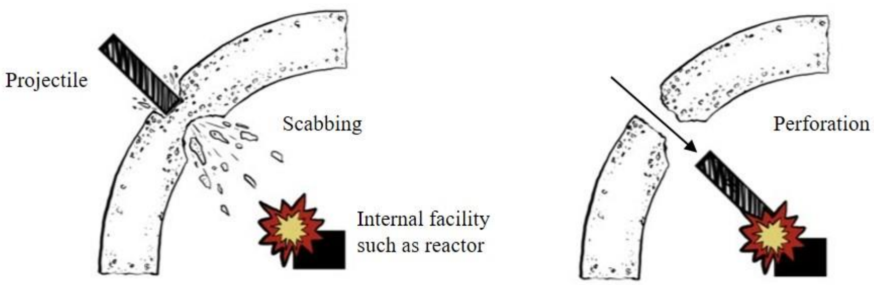

Figure 1.2 Local effects on structures: the impact of scabbing and perforation

The scabbing limit refers to the minimum wall thickness needed to prevent scabbing, while the perforation limit refers to the minimum thickness required to avoid perforation. Design standards in other countries may have slightly different recommended prediction equations. However, due to the mechanisms' complexity, empirical models based on experiments are commonly recommended by each design standard.

Table 1.1 Empirical formula model recommended by the DMFC(2017)

Formula	Depth of Penetration (h_{pen})	Scabbing limit (h_{scab})	Perforation limit (h_{per})
ACE (1946)	$\frac{h_{pen}}{d}=\frac{3.5\times10^{-4}}{\sqrt{f_{ck}}}\left(\frac{M}{d^3}\right)d^{0.215}V_0^{1.5}+0.5$	$\frac{h_{scab}}{d}=2.12+1.36\left(\frac{h_{pen}}{d}\right)$ for $0.65<\frac{h_{pen}}{d}\le11.75$ $\frac{h_{scab}}{d_{12.7mm}}=2.28+1.13\left(\frac{h_{pen}}{d_{12.7mm}}\right)$ for $0.65<\frac{h_{pen}}{d}\le11.75$	$\frac{h_{per}}{d}=1.32+1.24\left(\frac{h_{pen}}{d}\right)$ for $1.35<\frac{h_{pen}}{d}\le13.5$ $\frac{h_{per}}{d_{12.7mm}}=1.23+1.07\left(\frac{h_{pen}}{d_{12.7mm}}\right)$ for $1.35<\frac{h_{pen}}{d}\le13.5$
Conwep (1992)	$\frac{h_{pen}}{d}=2G^{0.5}\ (G\le1),\ \frac{h_{pen}}{d}=G+1\ (G>1)$ where $G=4.7\times10^{-5}\frac{N^*M}{d\sqrt{f_{ck}}}\left(\frac{V_0}{d}\right)^{1.8}$ • $N^*=0.72+0.25(CRH-0.25)^{0.5}$	$\frac{h_{scab}}{d}=7.91\left(\frac{h_{pen}}{d}\right)-5.06\left(\frac{h_{pen}}{d}\right)^2$ for $\frac{h_{pen}}{d}\le0.65$ $\frac{h_{scab}}{d}=2.12+1.36\left(\frac{h_{pen}}{d}\right)$ for $0.65<\frac{h_{pen}}{d}\le11.75$	$\frac{h_{per}}{d}=3.19\left(\frac{h_{pen}}{d}\right)-0.718\left(\frac{h_{pen}}{d}\right)^2$ for $\frac{h_{pen}}{d}\le1.35$ $\frac{h_{per}}{d}=1.32+1.24\left(\frac{h_{pen}}{d}\right)$ for $1.35<\frac{h_{pen}}{d}\le13.5$

At the Table 1.1, h_{pen} is the penetration depth, h_{scab} is the scabbing limit, and h_{per} is the perforation limit. f_c is the concrete compressive strength(MPa), d is the projectile's diameter(m), and M is the projectile's mass(kg). V_0 is the projectile impacting velocity(m/s).

However, there are several problems with using these empirical expressions. First, there are differences in the predictive accuracy of each equation, making it difficult to choose the appropriate empirical model. Figure 1.3 shows a comparison of the scabbing and perforation limits of the two empirical equations (ACE, 1946 and Conwep, 1992) recommended by the DMFC (2017) for the same projectile-target impact situation. The projectile assumed was a 37mm diameter ammunition with a mass of 0.85kg and gradually increasing impact velocity, while the target was a concrete wall with a compressive strength of 52MPa. The difference between the two equations increases as the impact velocity increases, with a maximum difference in thickness of 1.2 times.

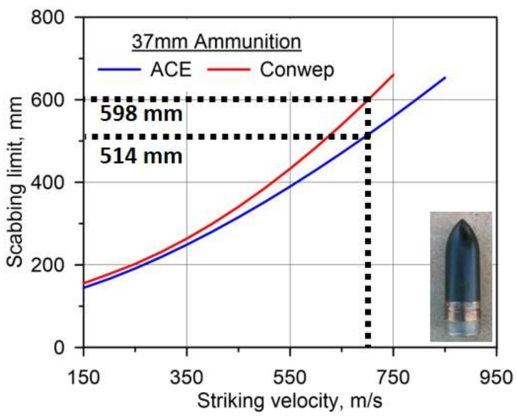

(a)

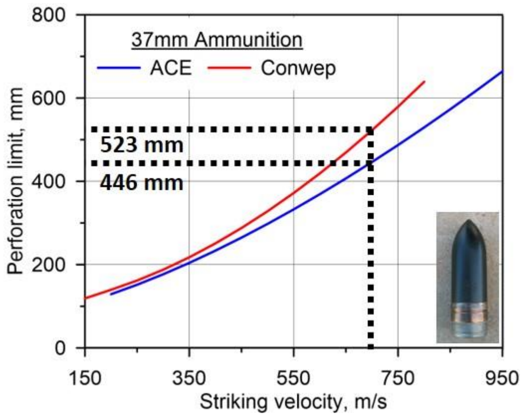

(b)

Figure 1.3 Comparison of scabbing & perforation limit using formulae

The investigation into these predictive equations originated from Petry's research in 1910 and has been continued by numerous researchers. Presently, the military is still using predictive equations that were proposed before and after World War II. However, the information and details regarding experiments are either too old or restricted for security reasons. Moreover, studies conducted after the 1970s focused mainly on nuclear power plants, and the extent to which the results apply to military weapons has not been thoroughly examined.

The second issue concerns the impact speed range. Experiments performed on nuclear power plant structures were primarily done at speeds of 300m/s or lower, which corresponds to aircraft impact speeds. Consequently, the adequacy of the suggested local damage prediction equation for military aircraft subjected to higher speed ranges and threats, as indicated in Figure 1.4, requires further examination.

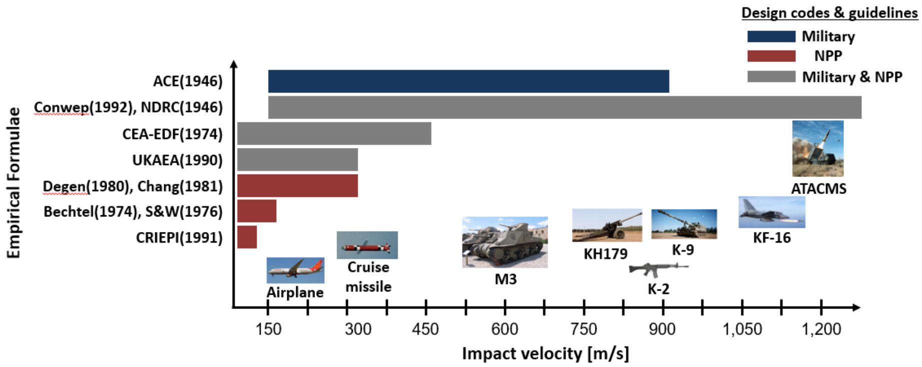

Figure 1.4 The applicable velocity range of empirical formulae

The precision of local damage prediction equations has been evaluated by several researchers (Kennedy, 1976; Sliter, 1980; Adeli-Amin, 1985) using crash test data collected from the United States and Europe. Nonetheless, the range of crash speeds used for these tests, as shown in Table 1.2, was restricted to speeds below 300m/s; hence, their accuracy at higher speeds cannot be guaranteed.

Table 1.2 Compare the accuracy of the existing prediction formula

Reference	Test (ea)	Projectile					Target			
		Velocity (m/s)	Weight (kg)	Diameter (mm)	Nose Shape	Type	Thickness (mm)	Rebar ratio (%)	Concrete strength (MPa)	Type
Kennedy (1976)	8	37-115	97	203	Flat	solid	305-610	0.4-0.6	30-40	RC
	9	40-145	60-95	203	Flat	pipe	305-610	0.4-0.6	30-40	RC
	3	90-150	90	203	Flat	wooden solid	305-610	0.6	30-40	RC
Sliter (1980)	102	27-312	0.109-343	20-305	-	Solid, pipe	75-610	-	22-49	RC
Adeli-Amin (1985)	87	22-309	20-300	100-305	Flat(87%), Cone(13%)	solid	104-600	-	33-50	RC

Researchers (Forrestal et al., 1994, 1996, 2005; Frew et al., 1998) have developed quasi-analytical equations for the depth of penetration (DOP) based on impact tests conducted up to 1 km/s, as shown in Table 1.3. However, these equations have a limitation as the thickness of the test specimens used were massive concrete blocks instead of typical members, and the scabbing and perforation limits were not examined separately. Therefore, experimental studies on wall thicknesses corresponding to actual members are necessary to predict the scabbing and perforation limits accurately.

Table 1.3 The study on DOP in high-speed collision situations

Reference	Test (ea)	Projectile					Target			Note
		Velocity (m/s)	Weight (kg)	Diameter (mm)	Nose Shape	Type	Thickness (mm)	Concrete strength (MPa)	Type	
	70	132-1050	0.064-485	12.9-76	Ogive	Solid	760-2,440	21.6-140	plain concrete	
Forrestal et al. (1994)	17	250-800	0.9-0.912	26.9	Ogive	Solid	760-1,830	32.5-108	plain concrete	Suggestion DOP formula
Forrestal et al. (1996)	24	450-1050	0.064-1.61	12.9-30.5	Ogive	Solid	760-2,440	13.5-62.8	plain concrete	Validation of suggested formula
Frew et al. (1998)	14	442-1009	0.478-1.62	20.3,30.5	Ogive	Solid	940-2,280	58.4	plain concrete	Validation of suggested Formula
Forrestal et al. (2003)	15	139-456	12.9-13.2	76	Ogive	Solid	1,220-1,830	23, 39	plain concrete	Validation of suggested formula

The third issue is that many of the significant predictive equations and the local damage prediction equations used in DMFC, such as ACE and Conwep, need to consider the effects of reinforcement when calculating. As shown in Table 1.1, these equations rely solely on the compressive strength of concrete to predict damage. However, rebar's presence can significantly impact structures' performance during impact events. The US Army's Technical Manual (TM 5-855-1, 1986) suggests that rebar located at the back of a wall can reduce scabbing and increase the scabbing limit. Unfortunately, the current predictive equations do not consider this performance improvement due to increased reinforcement.

Several studies (Sliter, 1980; Williams, 1994; Abdel-Kader et al., 2014; Lee et al., 2021) have shown that increased reinforcement can improve the scabbing limit and overall impact performance. Table 1.4 summarizes these findings. Therefore, further investigation is necessary to evaluate the impact of reinforcement on high-speed collision situations over 300m/s.

Table 1.4 Review of relation between rebar and local effect resistance

Reference	Year	Journal	Topic
Sliter	1980	ASCE	· **Normal reinforcement (0.3-1.5%)** does not significantly affect local damage including **scabbing** · **A large amount of steel(1.5-3%)** may enhance resistance to local effects**, especially for perforation**
Williams	1994	ACI	· For **penetration and scabbing, light or moderate reinforcement (~1.5%)** is likely to have **little effect** · **A heavy reinforcement(1.5% ~)** may improve performance, particularly **perforation resistance**
Abdel-Kader	2014	J. of Impact	· Test variable: 200-430m/s, 23mm Blunt, R. ratio 0.8-3.0% · **Reinforcement** had **little effect on DOP, but reduced scabbing area**
Lee et.al.	2021	J. of Impact	· The effect on **the strength and diameter** of the rebar was small · **Rebar spacing improves** impact resistance performance

1.2. Research objectives and scope

Several issues are related to the current predictive equations provided by local damage design criteria. Firstly, these equations vary in predictive values, making it challenging to select the appropriate one for a given situation. Secondly, there needs to be more experimental data on the actual member size in the high-impact speed range to account for speeds above 300 m/s, the impact speed of military weapons.

Furthermore, there are limitations to the availability of crash test data for military weapons due to security restrictions, and the available data is often outdated. Similarly, crash tests conducted on nuclear power plant structures have only been focused on relatively low speeds, limiting the available data's usefulness for military purposes. This lack of data makes it difficult to predict these structures' impact performance accurately.

Finally, it is worth noting that most prediction equations do not consider the effect of reinforcement, which can have a significant impact on the performance of these structures under impact conditions. As a result, they do not provide a quantitative measure of the impact of increasing reinforcement on impact performance. Addressing these issues is crucial for improving the accuracy of impact performance predictions and ensuring the safety of critical structures.

The primary objectives of this study are twofold. Firstly, to conduct an experimental investigation to verify the accuracy of the existing local damage prediction equation. Secondly, to propose a modified prediction equation that considers rebar's effect on the impact resistance of reinforced concrete (RC) targets.

To achieve these objectives, the study aims to verify the accuracy of the existing prediction equation by conducting collision experiments on RC targets in the high-speed collision range. The experiment seeks to derive the limit values for scabbing and perforation. Subsequently, the effect of rebar on the impact resistance performance is evaluated based on the experimental results. This study proposes a modified prediction equation for local damage that reflects the variables of rebar.

Finally, additional numerical analyses are conducted to further validate the proposed empirical model's utility. Overall, this study seeks to provide a more accurate and reliable prediction equation for local damage by considering the effect of rebar on the impact resistance of RC targets.

1.3. Organization

Chapter 1 shows the introduction of this study. The chapter covers the background of the study, the objectives of the research, and the scope of the study and provides an outline of the remaining chapters.

Chapter 2 overviews the design codes and guidelines currently applied to military facilities and nuclear power plants. Additionally, it presents a comprehensive literature review of prior research on this topic. This review includes two main types of formulae: (1) empirical formulae based on experiments and (2) analytical formulae based on theory.

Chapter 3 describes the test program conducted using a 60 mm single-stage gas gun in detail. The chapter provides a comprehensive account of the various test procedures, including preparing the test specimens and the execution of the impact tests. The data processing procedures used to analyze the resulting data are also presented.

In Chapter 4, a detailed discussion of the test results is provided. This includes an analysis of the damage and failure modes observed during the tests and an evaluation of the correlation between the experimental results and the existing prediction equations. Based on this analysis, modifications to the prediction equations are proposed to account for the effects of reinforcement. These proposed modifications are then validated against the experimental results. The outcomes of this chapter provide a critical contribution to developing more accurate and reliable prediction equations for localized damage in reinforced concrete structures.

Chapter 5 presents the numerical analysis program used for the impact test in this study, including the modeling procedure and FEA results. It also compares the numerical results with experimental data and discusses the validity of the modified prediction equation.

Lastly, Chapter 6 summarizes the study's conclusions, findings, and future research recommendations.

Appendices A and B include all experimental data not presented in Chapter 4 to maintain brevity.

2. Literature Review

2.1. Introduction

The design and construction of military facilities and nuclear power plants (NPPs) must adhere to strict regulations and guidelines to ensure their safety and durability. A crucial aspect of these regulations is the consideration of local damage effects on the overall structural integrity of these facilities. Such damage can arise from various external factors, including impacts from projectiles or other objects, and it can result in significant damage or even failure of the structure.

Researchers have developed empirical and analytical prediction equations to predict the behavior of these structures in such scenarios. Empirical equations are derived from experimental data, while analytical equations are based on theoretical models. These equations guide the necessary protective levels to withstand a given level of impact and are used to design structures that can withstand extreme conditions.

This research aims to investigate the accuracy of existing local damage prediction equations through experimental verification and to propose a modified equation that considers the effects of reinforcement on the impact resistance of reinforced concrete targets. To achieve this, this chapter reviews previous research on local damage prediction equations, discusses the design codes and guidelines applied to military facilities and NPP structures, and examines existing empirical and analytical formulae in this field.

2.2. Design codes & guideline for local effect

Design codes and guidelines for local effects refer to the set of rules and regulations that govern the design and construction of structures to withstand local damage caused by external factors such as impacts, explosions, or fires. These codes are essential for ensuring critical infrastructure assets' safety and structural integrity, including military facilities and nuclear power plants. They guide the necessary wall thickness to withstand a given level of local damage and help designers create structures that can withstand extreme conditions.

2.2.1. Military design codes & guidelines

Table 2.1 provides a comprehensive overview of various criteria and guidelines for designing military facilities, including recommended empirical formulas. These guidelines are essential to ensure critical assets' safety and structural integrity, such as military bases and installations. However, due to the complex nature of collision mechanisms, there are differences in the suggested prediction equations for each design criterion. As a result, both the Korean military and other nations' militaries recommend using experiment-based empirical models.

This approach provides a more accurate prediction of local damage effects, which can inform decisions on the wall thickness and reinforcement levels required to withstand different types and levels of impact. By using such empirical models, designers can create resilient structures that can withstand extreme conditions, which is essential for ensuring the safety of military personnel and infrastructure.

Table 2.1 Military design codes & guidelines for local effects

Organization		Design codes & guidelines	Empirical formulae		
			Penetration	Scabbing	Perforation
ROK Army		DMFC 2-20-10 (2017)	ACE, Conwep		
US (before 2002)	Army	TM 5-855-1 (1986)	ACE		
	Air Force	ESL-TR-87-57 (1987)	Modified NDRC	ACE	
	Navy	NP-3726 (1950)	Modified Petry		
	DDESB*	ARLCD-SP-84001 (1987)	Modified NDRC		
US military (after 2002)		UFC 3-340-01 (2002)	Unknown (Military secret)		
British Army		British Army Manual (1992)	UKAEA		CEA-EDF

*Department of Defense Explosive Safety Board

2.2.2. NPP design codes & guidelines

In Table 2.2, guidelines and empirical equations for calculating wall thicknesses to prevent localized damage can be found in the design standards of the American Concrete Institute, Department of Energy, and Nuclear Society. These guidelines ensure critical infrastructure assets' structural integrity and safety, such as military facilities and nuclear power plants. Using empirical equations, designers can determine the wall thicknesses needed to withstand potential localized damage from external factors such as impacts, explosions, or fires.

Table 2.2 NPP design codes & guidelines for local effects

Design codes	Empirical formulae		
	Penetration	Scabbing	Perforation
ACI 349-13 (2014)	-	Modified NDRC, Bechtel, Stone and Webster	Modified NDRC
DOE-STD-3014-2006 (2006)	Modified NDRC	Modified NDRC, Bechtel, Chang, CRIEPI	Modified NDRC, CEA-EDF, Chang, CRIEPI, Degen
NEI 07-13 (2009)	Modified NDRC	Chang	Degen

* ACI – American concrete institute
DOE – U.S. Department of Energy
NEI – Nuclear Energy Institute

2.3. Existing empirical formulae

The current section reviews the impact formula for penetration, scabbing, and perforation limit thickness. The aim is to evaluate the impact resistance of concrete by examining the existing impact formulae. The review is based on the work of previous researchers, including Kennedy (1976) and Li et al. (2005), who summarized the available formulae. This summary is critical for comprehending the existing impact formulae and developing a new formula using additional experimental data.

1) Penetration depth (h_{pen}) : This can be defined as measuring the depth to which a projectile penetrates the concrete from the point of contact. Although penetration is not guaranteed to occur in a single impact, multiple collisions at the same hit point can cause scabbing or perforation. Therefore, accurately predicting the penetration depth is a fundamental factor in assessing the impact resistance of concrete.

2) Scabbing limit thickness (h_{scab}) : This refers to the minimum thickness of a concrete target that prevents scabbing, a process in which fragments are ejected from the rear face of the target without complete perforation. Scabbing typically occurs when a projectile impact results in high-stress waves that exceed the material's tensile strength on the rear side. Therefore, accurately determining the scabbing limit thickness is crucial in designing reinforced concrete structures to withstand high-velocity impacts.

3) Perforation limit thickness (h_{per}) : This designates the minimum thickness of a concrete target necessary to prevent perforation, a condition where a projectile thoroughly penetrates the material and passes through it. Perforation typically occurs when the force of the projectile impact exceeds the overall resistance of the concrete target. Consequently, accurately determining the perforation limit thickness is a critical factor in designing reinforced concrete structures to withstand high-velocity impacts.

The current section reviews the impact formula for penetration, scabbing, and perforation limit thickness. The aim is to evaluate the impact resistance of concrete by examining the existing impact formulae. The review is based on the work of previous researchers, including Kennedy (1976) and Li et al. (2005), who summarized the available formulae. This summary is critical for comprehending the existing impact formulae and developing a new formula using additional experimental data.

This chapter has standardized the empirical formulae to the International System of Units (SI), even though they were originally expressed using different units. The notation used for symbols throughout the study, and their respective units in SI units is given in Table 2.3

Table 2.3 Physical quantities and their units used in empirical formulae

Symbol	Parameter	Units(SI)
h_{pen}	Penetration depth	m
h_{per}	Perforation limit	m
h_{scab}	Scabbing limit	m
E	Elasticity modulus of projectile	Pa
E_s	Elasticity modulus of steel	Pa
M	Mass of the projectile	kg
d	Diameter of the projectile	m
h	Height of the projectile nose	m
R_s	Radius of the projectile nose	m
H	Thickness of the cone plug	m
H_0	Thickness of the concrete target	m
f_t	Static tensile strength of concrete	Pa
f_c	Static compressive strength of concrete	Pa
a	The maximum coarse aggregate size	m
V_0	Projectile impacting velocity	m/s
$N*$	Nose shape factor	-
ρ_c	Density of the concrete	Kg/m^3
ψ	Caliber-radius-head	-
A	Cross sectional area	m^2

2.3.1. Modified Petry formula

The Petry penetration formula is the oldest available formula for predicting the penetration depth in an infinite concrete target. It was originally developed in 1910. In the US, the modified Petry formula is one of the most commonly used formulas to predict the penetration depth in a concrete target with infinite thickness.

$$\frac{h_{pen}}{d} = k\frac{M}{d^3}\log_{10}\left(1+\frac{V_0^2}{19{,}974}\right) \tag{2.1}$$
$$k = 6.34\times10^{-3}\exp(-0.2973\times10^{-7} f_c)$$

$$h_{scab} = 2.2\times h_{pen} \tag{2.2}$$

$$h_{per} = 2.0\times h_{pen} \tag{2.3}$$

For modified Petry II, the suggested values for k is determined by the strength of the concrete. Based on the penetration depth, Amirikian (1950) suggested the perforation and scabbing thicknesses. k is the modulus associated with concrete compressive strength f_c. d is the projectile's diameter, and M is the projectile's mass. V_0 is the projectile impacting velocity.

2.3.2. Ballistic Research Laboratory (BRL) formula

The BRL formula was developed in 1941 for calculating the depth of penetration in concrete when a rigid projectile strikes it. The Ballistic Research Laboratory (BRL) was a scientific research organization in the United States Army responsible for conducting research and development in the field of ballistics, with a focus on developing military weaponry and related technology.

$$\frac{h_{pen}}{d} = \frac{1.33\times10^{-3}}{\sqrt{f_c}}\left(\frac{M}{d^3}\right)d^{0.2}V_0^{1.33} \tag{2.4}$$

$$h_{scab} = 2.0\times h_{pen} \tag{2.5}$$

$$h_{per} = 1.3\times h_{pen} \tag{2.6}$$

2.3.3. Army corps of engineers (ACE) formula

The ACE formula for penetration depth was developed by ACE based on experimental results before 1943 from the Ordnance Department of the US Army and the BRL. The term M/d^3 is called the missile caliber density. The formulae for perforation and scabbing limits were based on the penetration depth given by the ACE formula. The perforation and scabbing formulae are based on regression analyses of data from ballistic tests on 37, 75, 76.2, and 155 mm steel cylindrical missiles. Additional data for 12.7mm were obtained in 1944, and the formulae were modified. Eq. 2.10 and 2.11 differ only slightly from Eq. 2.8 and 2.9.

$$\frac{h_{pen}}{d} = \frac{3.5\times10^{-4}}{\sqrt{f_c}}\left(\frac{M}{d^3}\right)d^{0.215}V_0^{1.5} + 0.5 \tag{2.7}$$

$$\frac{h_{scab}}{d} = 2.12 + 1.36\left(\frac{h_{pen}}{d}\right) \text{ for } 0.65 < \frac{h_{pen}}{d} \le 11.75 \tag{2.8}$$

$$\frac{h_{per}}{d} = 1.32 + 1.24\left(\frac{h_{pen}}{d}\right) \text{ for } 1.35 < \frac{h_{pen}}{d} \le 13.5 \tag{2.9}$$

$$\frac{h_{scab}}{d_{12.7mm}} = 2.28 + 1.13\left(\frac{h_{pen}}{d_{12.7mm}}\right) \text{ for } 0.65 < \frac{h_{pen}}{d} \le 11.75 \tag{2.10}$$

$$\frac{h_{scab}}{d_{12.7mm}} = 1.23 + 1.07\left(\frac{h_{pen}}{d_{12.7mm}}\right) \text{ for } 1.35 < \frac{h_{pen}}{d} \le 13.5 \tag{2.11}$$

2.3.4. Modified NDRC formula

The US National Defense Research Committee introduced this formula in 1946, building on the ACE formulae, additional testing data, and a penetration model for a rigid projectile penetrating a massive concrete target. The formula assumes that the contact force increases linearly to a constant maximum value when the penetration depth is small. The NDRC formula was initially developed by equating the following G-function:

$$G = \frac{KN * M}{d}\left(\frac{V_0}{1000d}\right)^{1.8} \text{ (US, Original formula)} \tag{2.12}$$

The Eq. 2.12 includes the nose shape factor $N*$ and the concrete penetrability factor K, both of which are dependent on concrete strength. The nose shape factor $N*$ is 0.72, 0.84, 1.0, and 1.14 to flat, hemispherical, blunt, and very sharp noses, respectively (Li et al., 2005).

The factor K was not fully defined in the NDRC study due to declining interest in projectile penetration of concrete after 1946, but was later determined by Kennedy (1966) based on experimental data. The present modified NDRC penetration formula uses K equal to 180 divided by $\sqrt{f_c}$ and is defined by a new G-function as shown in Eq. 2.13 -2.14.

$$G = 3.8 \times 10^{-5} \frac{N*M}{d\sqrt{f_c}} \left(\frac{V_0}{d} \right)^{1.8} \tag{2.13}$$

• $N*$(Flat)=0.72, $N*$(Blunt)=0.84, $N*$(Spherical)=1.0, $N*$(Sharp)=1.14

$$\frac{h_{pen}}{d} = 2G^{0.5} \quad (G \le 1) \tag{2.14a}$$

$$\frac{h_{pen}}{d} = G + 1 \quad (G > 1) \tag{2.14b}$$

By extending the ACE formulae to thin targets, the limits of perforation and scabbing can be predicted, respectively.

$$\begin{aligned} \frac{h_{scab}}{d} &= 7.91\left(\frac{h_{pen}}{d}\right) - 5.06\left(\frac{h_{pen}}{d}\right)^2 \quad \text{for } \frac{h_{pen}}{d} \le 0.65 \\ \frac{h_{scab}}{d} &= 2.12 + 1.36\left(\frac{h_{pen}}{d}\right) \quad \text{for } 0.65 < \frac{h_{pen}}{d} \le 11.75 \end{aligned} \tag{2.15}$$

$$\frac{h_{per}}{d} = 3.19\left(\frac{h_{pen}}{d}\right) - 0.718\left(\frac{h_{pen}}{d}\right)^2 \quad \text{for } \frac{h_{pen}}{d} \leq 1.35$$
$$\frac{h_{per}}{d} = 1.32 + 1.24\left(\frac{h_{pen}}{d}\right) \quad \text{for } 1.35 < \frac{h_{pen}}{d} \leq 13.5 \tag{2.16}$$

2.3.5. Kar formula

In the post-war period, the impact effects on concrete became a crucial safety concern for nuclear power plants. To address this, Kar revised the NDRC formula and used regression analysis to incorporate the type of missile material in terms of Young's modulus E. The resulting empirical formula is Eq. 2.17.

$$\frac{h_{pen}}{d} = 2G^{0.5} \quad (G \leq 1), \quad \frac{h_{pen}}{d} = G + 1 \quad (G > 1)$$
$$\text{where} \quad G = 3.8 \times 10^{-5}\left(\frac{E}{E_s}\right)^{1.25} \frac{N * M}{d\sqrt{f_c}}\left(\frac{V_0}{d}\right)^{1.8} \tag{2.17}$$

• $N*$(Flat)=0.72, $N*$(Blunt)=0.84, $N*$(Spherical)=1.0, $N*$(Sharp)=1.14

The empirical formula takes into account the Young's moduli of both the projectile and steel, denoted by E and E_s, respectively. The determination of the perforation and scabbing limits depends on two factors: the size of aggregates a and the Young's modulus of the projectile E_s. Eq. 2.18-2.19 expresses the perforation and scabbing limit.

$$\frac{h_{scab}-a}{d}\left(\frac{E_s}{E}\right)^{0.2}=7.91\left(\frac{h_{pen}}{d}\right)-5.06\left(\frac{h_{pen}}{d}\right)^2 \text{ for } \frac{h_{pen}}{d}\le 0.65$$
$$\frac{h_{scab}-a}{d}\left(\frac{E_s}{E}\right)^{0.2}=2.12+1.36\left(\frac{h_{pen}}{d}\right) \text{ for } 0.65<\frac{h_{pen}}{d}\le 11.75 \tag{2.18}$$

$$\frac{h_{per}-a}{d}=3.19\left(\frac{h_{pen}}{d}\right)-0.718\left(\frac{h_{pen}}{d}\right)^2 \text{ for } \frac{h_{pen}}{d}\le 1.35$$
$$\frac{h_{per}-a}{d}=1.32+1.24\left(\frac{h_{pen}}{d}\right) \text{ for } 1.35<\frac{h_{pen}}{d}\le 13.5 \tag{2.19}$$

When the material of the projectile is steel, the prediction formula for penetration depth is identical to the modified NDRC formula.

2.3.6. CEA-EDF formula

In 1974, CEA and EDF in France initiated a comprehensive program to enhance the reliability of predictions concerning the ballistic behavior of reinforced concrete slabs upon impact by missiles. After performing a series of drop-weight and air gun tests, CEA-EDF proposed a formula for the perforation limit. CEA stands for Commissariat à l'énergie atomique et aux énergies alternatives, which is the French Alternative Energies and Atomic Energy Commission. EDF stands for Électricité de France, the French electricity generation and distribution company.

$$\frac{h_{per}}{d}=0.82\frac{M^{0.5}V_0^{0.75}}{\rho_c^{0.125}f_c^{0.375}d^{1.5}} \tag{2.20a}$$

$$V_p = 1.3\rho_c^{1/6} f_c^{0.5} \left(\frac{dH_0^2}{M} \right)^{2/3} \tag{2.20b}$$

$$V_p = 1.3\rho_c^{1/6} f_c^{0.5} \left(\frac{dH_0^2}{M} \right)^{2/3} (\gamma + 0.3)^{0.5} \tag{2.20c}$$

V_p is the ballistic limit, H_0 is the thickness of the target, and γ is the percentage of reinforcement described by the percentage each way in each face (%, EWEF). Fullard et al. (1991) extended Eq. 2.20b to non-circular missile cross-section and reinforced concrete, as shown in Eq. 2.20c.

2.3.7. UKAEA formula

Barr (1990) proposed a modification to the NDRC formula based on extensive research on protecting nuclear power plant structures in the UK. This modification was mainly aimed at lower impact velocities, which are more relevant to the nuclear industry.

$$\frac{h_{pen}}{d} = 0.275 - [0.0756 - G]^{0.5} \quad (G \le 0.0726) \tag{2.21a}$$

$$\frac{h_{pen}}{d} = [4G - 0.242]^{0.5} \quad (0.0726 < G \le 1.0605) \tag{2.21b}$$

$$\frac{h_{pen}}{d} = G + 0.9395 \quad (G > 1.065) \tag{2.21c}$$

$$G = 3.8\times10^{-5}\frac{N^{*}M}{d\sqrt{f_c}}\left(\frac{V_0}{d}\right)^{1.8} \tag{2.22}$$

N^{*}(Flat)=0.72, N^{*}(Blunt)=0.84, N^{*}(Spherical)=1.0, N^{*}(Sharp)=1.14

This formula has been evaluated for its accuracy in predicting penetration within the specific parameter ranges: striking velocities between 25 to 300 m/s, concrete compressive strength between 22 to 44 MPa, and M/d^3 between 5000 to 200,000 kg/m^3. The prediction accuracy for the normalized depth of penetration (h_{pen}/d) is within -20 to +20% for h_{pen}/d values between 0.4 and 0.75 and within -50 to +100% for h_{pen}/d values below 0.75.

$$\frac{h_{scab}}{d} = 5.3G^{0.33} \tag{2.23}$$

The accuracy of this formula has been evaluated within the parameter ranges of 29 to 238 m/s for striking velocity, 26 to 44 MPa for concrete compressive strength, and 3,000 to 222,200 kg/m^3 for M/d^3. The prediction accuracy for the dimensionless parameter 2.0 < h_{scab}/d < 5.56 is within -40 to +40%.

2.3.8. Bechtel formula

Bechtel Power Corporation created the scabbing limit formula presented here, and its development was based on recent test data related to missile impacts on nuclear-plant structures. It applies only to rigid projectiles, such as solid steel slugs or rods, and may be used cautiously for hollow pipe projectiles. The predictions derived from the Bechtel formula are generally consistent with those obtained from the Stone and Webster formula.

$$\frac{h_{scab}}{d} = 38.98\left(\frac{M^{0.4}V_0^{0.5}}{f_c^{0.5}d^{1.2}}\right) \tag{2.24}$$

2.3.9. Stone and Webster formula

This formula is proposed to predict the scabbing limit. The value of the dimensional coefficient C varies based on the ratio of the target thickness to the projectile diameter.

$$\frac{h_{scab}}{d} = \left(\frac{MV_0^2}{Cd^3}\right)^{1/3} \tag{2.25}$$

For solid projectiles, C varies from 0.35 to 0.37 when H_0/d varies from 1.5 to 3.0.

$$C = 0.013(H_0/d) + 0.330 \tag{2.26}$$

The formula has been tested for a range of parameters between 20.7(MPa) < f_c < 31.0(MPa), and 1.5 < h_s / d < 3.0.

2.3.10. Degen formula

Degen proposed the following formula to determine the perforation limit based on a statistical analysis of the experimental data.

$$\frac{h_{per}}{d} = 2.2\left(\frac{h_{pen}}{d}\right) - 0.3\left(\frac{h_{pen}}{d}\right)^2 \quad \text{for } \frac{h_{pen}}{d} < 1.52 \tag{2.27a}$$

$$\frac{h_{per}}{d} = 0.69 + 1.29\left(\frac{h_{pen}}{d}\right) \quad \text{for } 1.52 \le \frac{h_{pen}}{d} \le 13.42 \tag{2.27b}$$

This perforation formula is applicable within the valid ranges of 28.4 ≤ f_c ≤ 43.1 MPa, 25.0 ≤ V_0 ≤ 311.8 m/s, 0.15 ≤ H_0 ≤ 0.61 m, and 0.10 ≤ d ≤ 0.31 m, where h_{pen} is determined using the modified NDRC formula.

2.3.11. Haldar-Hamieh formula

Haldar and Hamieh suggested the use of an impact factor I_a, defined by Eq. 2.28 to predict the penetration depth, i.e.

$$I_a = \frac{MN * V_0^2}{d^3 f_c} \tag{2.28}$$

$$\frac{h_{pen}}{d} = -0.0308 + 0.2251 I_a \text{ for } (0.3 \le I_a \le 4.0) \quad (2.29a)$$

$$\frac{h_{pen}}{d} = 0.6740 + 0.0567 I_a \text{ for } (4.0 < I_a \le 21.0) \quad (2.29b)$$

$$\frac{h_{pen}}{d} = 1.1875 + 0.0299 I_a \text{ for } (21.0 < I_a \le 455) \quad (2.29c)$$

The formula includes the nose shape factor N^*, as defined in the modified NDRC formula, and the dimensionless parameter I_a. Any set of consistent units for the variables M, V_0, d and f_c can be used in this formula. Using the penetration depth formula described above Eq. 2.29, it was proposed that the perforation limit could be determined using the NDRC formula. For the scabbing limit, the NDRC formula is used when I_a is less than 21. If I_a exceeds this value, Eq. 2.30 should be employed.

$$\frac{h_{scab}}{d} = 3.3437 + 0.0342 I_a \text{ for } (21 \le I_a \le 385) \quad (2.30)$$

2.3.12. Adeli-Amin formula

Adeli and Amin utilized the impact factor I_a, as defined by Haldar and Hamieh, to fit Sliter's data on penetration, perforation, and scabbing.

$$\frac{h_{pen}}{d} = -0.0416 + 0.1698 I_a - 0.0045 I_a^2 \text{ for } (0.3 \le I_a \le 4.0) \quad (2.31a)$$

$$\frac{h_{pen}}{d} = 0.0123 + 0.196 I_a - 0.008 I_a^2 + 0.0001 I_a^3 \quad \text{for } (0.3 \leq I_a \leq 4.0) \tag{2.31b}$$

According to the impact factor proposed by Haldar and Hamieh and discussed above in Eq. 2.28, the Eq. 2.32-2.33 was proposed as a means to determine the scabbing and perforation limit.

$$\frac{h_{scab}}{d} = 0.9060 + 0.3214 I_a - 0.0106 I_a^2 \quad \text{for } (0.3 \leq I_a \leq 21) \tag{2.32}$$

$$\frac{h_{per}}{d} = 1.8685 + 0.4035 I_a - 0.0114 I_a^2 \quad \text{for } (0.3 \leq I_a \leq 21) \tag{2.33}$$

2.3.13. Hughes formula

Hughes (1984) assumed that the resistance to penetration initially increased linearly, similar to the assumption used in the NDRC formulas, and subsequently decreased in a parabolic manner with increasing penetration depth. Based on this, Hughes proposed the following Eq. 2.34 for calculating penetration depth.

$$\frac{h_{pen}}{d} = 0.19 \frac{N_h I_h}{S} \tag{2.34}$$

N_h(Flat)=1.0, N_h(Blunt)=1.12, N_h(Spherical)=1.26, N_h(Sharp)=1.39

The projectile nose shape coefficient, N_h, takes a value of 1.0, 1.12, 1.26, and 1.39 for flat, blunt, spherical, and very sharp noses, respectively. I_h is a non-dimensional “impact factor” defined by Eq. 2.35.

$$I_h = \frac{MV_0^2}{d^3 f_t} \tag{2.35}$$

The value of I_h was derived via dimensional analysis, and any set of units that are consistent for M, V_0, d, and f_t can be used. While many equations use the compressive strength of concrete to calculate penetration resistance, Eq. 2.35 expresses the penetration resistance using the tensile strength of concrete instead of the compressive strength.

Hughes incorporated the effect of strain rate on the tensile strength of concrete by introducing a dynamic increase factor (DIF) S. Consequently, the tensile strength f_t was replaced by Sf_t in his model. To obtain the dynamic compressive strength, the dynamic tensile strength was multiplied by a constant coefficient.

$$S=1+12.3\ln(1+0.03I_h) \tag{2.36}$$

The perforation and scabbing limits are predicted by Eq. 2.37-2.38 where h_{pen}/d is determined by Eq. 2.34.

$$\frac{h_{scab}}{d} = 5.0\left(\frac{h_{pen}}{d}\right) \text{ for } (\frac{h_{pen}}{d} < 0.7) \tag{2.37a}$$

$$\frac{h_{scab}}{d} = 1.74\left(\frac{h_{pen}}{d}\right) + 2.3 \text{ for } (\frac{h_{pen}}{d} \geq 0.7) \tag{2.37b}$$

$$\frac{h_{per}}{d} = 3.6\left(\frac{h_{pen}}{d}\right) \quad \text{for } \left(\frac{h_{pen}}{d} < 0.7\right) \qquad (2.38a)$$

$$\frac{h_{per}}{d} = 1.58\left(\frac{h_{pen}}{d}\right) + 1.4 \quad \text{for } \left(\frac{h_{pen}}{d} \geq 0.7\right) \qquad (2.38b)$$

These equations were verified within the range of available test data for $I_h < 3500$, they are considered conservative for values of $I_h < 40$ and $H_o / d < 3.5$.

2.3.14. CRIEPI formula

CRIEPI stands for Central Research Institute of Electric Power Industry. It is a research and development organization located in Japan that promotes the safe and efficient use of electric power. The penetration depth, scabbing limit, and perforation limit are given by Eq. 2.39-2.41.

$$\frac{h_{pen}}{d} = \frac{0.0265N * Md^{0.2}V_0^2(114 - 6.83\times10^{-4} f_c^{2/3})}{f_c^{2/3}}\left[\frac{(d+1.25H_r)H_r}{(d+1.25H_0)H_0}\right] \qquad (2.39)$$

$$\frac{h_{scab}}{d} = 1.75\left(\frac{61}{V_0}\right)^{0.13}\left(\frac{MV_0^2}{d^3 f_c}\right)^{0.4} \qquad (2.40)$$

$$\frac{h_{per}}{d} = 0.6\left(\frac{61}{V_0}\right)^{0.25}\left(\frac{MV_0^2}{d^3 f_c}\right)^{0.5} \qquad (2.41)$$

In Eq. 2.39, $H_r = 0.2$ m means the reference thickness of the slab.

2.3.15. Conwep formula

Conwep (Conventional Weapons Effects Program) is a program developed by the US Department of Defense to simulate and calculate the effects of conventional weapons, such as explosives, on various types of targets. The formula used in Conwep (1992) is shown below in Eq. 2.42-2.43, an updated version from the one used in TM 5-855-1 (Hansson, 2003).

$$G = 4.7 \times 10^{-5} \frac{N^* M}{d\sqrt{f_c}} \left(\frac{V_0}{d}\right)^{1.8} \tag{2.42}$$

$$N^* = 0.72 + 0.25(CRH - 0.25)^{0.5}$$

$$\frac{h_{pen}}{d} = 2G^{0.5} \quad (G \le 1) \tag{2.43a}$$

$$\frac{h_{pen}}{d} = G + 1 \quad (G > 1) \tag{2.43b}$$

By using the NDRC formula, the limits of scabbing and perforation be predicted respectively.

$$\begin{aligned} \frac{h_{scab}}{d} &= 7.91\left(\frac{h_{pen}}{d}\right) - 5.06\left(\frac{h_{pen}}{d}\right)^2 \quad \text{for } \frac{h_{pen}}{d} \le 0.65 \\ \frac{h_{scab}}{d} &= 2.12 + 1.36\left(\frac{h_{pen}}{d}\right) \quad \text{for } 0.65 < \frac{h_{pen}}{d} \le 11.75 \end{aligned} \tag{2.44}$$

$$\begin{aligned} \frac{h_{per}}{d} &= 3.19\left(\frac{h_{pen}}{d}\right) - 0.718\left(\frac{h_{pen}}{d}\right)^2 \quad \text{for } \frac{h_{pen}}{d} \le 1.35 \\ \frac{h_{per}}{d} &= 1.32 + 1.24\left(\frac{h_{pen}}{d}\right) \quad \text{for } 1.35 < \frac{h_{pen}}{d} \le 13.5 \end{aligned} \tag{2.45}$$

2.4. Existing analytical formulae

2.4.1. Dynamic cavity expansion theory for concrete material

The cavity expansion theory has been an important area of research in impact mechanics. Bishop et al. (1945) conducted a pioneering study on this theory, developing quasi-static equations for expanding a cavity generated by a wedge-shaped penetrator that was slowly punched into a metal target. These equations were then used to estimate the resistance force applied to the penetrator. Building on this work, Hill (1948) and Hopkins (1960) further developed the dynamic cavity expansion theory, which is applicable when a penetrator has momentum and is punched into a target. The dynamic cavity expansion theory has since been widely used in the study of impact mechanics.

In later years, Forrestal & Tzou (1997) developed a penetration model for concrete targets using dynamic cavity expansion theory. They applied this theory to concrete targets and found that it represented the penetration process well. Kong et al. (2017) further improved upon this model by suggesting an extended penetration model that utilized a yield surface for concrete of hyperbolic function form and the Murnaghan equation of state, which is a general form of the Mohr-Coulomb yield surface and linear equation of state adopted in Forrestal & Tzou (1997). As a result, the dynamic cavity expansion theory, using the general form suggested by Kong et al. (2017), is explained in detail in this chapter.

The penetration model suggested by the dynamic cavity expansion theory is based on several assumptions.

1. Target medium has an infinite radius and thickness

2. Cavity is expanded radially from the penetrated projectile surface and is spherically symmetric

3. Velocity of a projectile on the penetrated surface is equal to the particle velocity of the cavity surface

In the penetration model based on the dynamic cavity expansion theory, the expansion of the cavity at a constant velocity V_c leads to the formation of plastic, cracked, and elastic response regions, as depicted in Figure 2.1. When the velocity of the projectile is extremely high, the value of c is more significant than c_1 causing the cracked response region to disappear. Where r is the radial Eulerian coordinate, t is times, c and c_1 are interface velocities, and c_d is the elastic, dilatation velocity.

However, in most cases of aircraft impact, which occurs in the low-velocity range of 100-250 m/s, c_1 is larger than c resulting in the presence of the cracked response region.

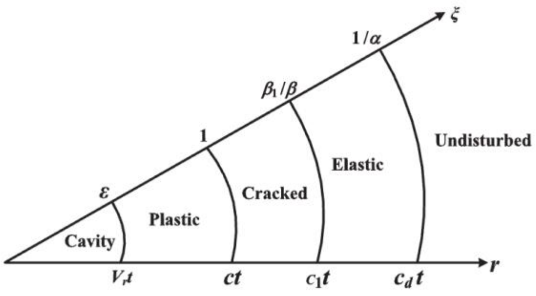

Figure 2.1 Response regions for concrete material (Forrestal et al., 1997)

2.4.1.1. Plastic region

The behavior of concrete material in the plastic region is under triaxial compression condition, which results in compressive behavior following the compressive meridian of the yield surface expressed by a hyperbolic function, as demonstrated in Eq. 2.46 and Eq. 2.47. The assumption of a spherically symmetric condition leads to the hoop components of Cauchy stress in spherical coordinates being the same, as presented in Eq. 2.48. Thus, the yield surface for the deviatoric stresses can be expressed as shown in Eq. 2.49.

$$\Delta\sigma = a_0 + \frac{P}{a_1 + a_2 P} \tag{2.46}$$

$$P = (\sigma_r + \sigma_\theta + \sigma_\varphi)/3 \tag{2.47}$$

$$\sigma_\theta = \sigma_\varphi \tag{2.48}$$

$$\Delta\sigma = \sqrt{3J_2} = |\sigma_r - \sigma_\theta| \tag{2.49}$$

The concrete material in the plastic region can be assumed to exhibit nonlinearly compressive behavior, which can be expressed by the Murnaghan equation of state as shown in Eq. 2.50.

$$P = \frac{K}{\gamma}\left[\left(\frac{\rho}{\rho_0}\right)^{\gamma} - 1\right] \tag{2.50}$$

Assuming the plastic region of the target medium is described by the equations of momentum and mass conservation in Eulerian coordinates, the equations governing the motion of a compressible concrete material are given by Eq. 2.51 and Eq. 2.52.

$$\frac{\partial \sigma_r}{\partial r} + \frac{2(\sigma_r - \sigma_\theta)}{r} = -\rho\left(\frac{\partial v}{\partial t} + v\frac{\partial v}{\partial t}\right) \tag{2.51}$$

$$\rho\left(\frac{\partial v}{\partial r} + \frac{2v}{r}\right) = -\left(\frac{\partial \rho}{\partial t} + v\frac{\partial \rho}{\partial r}\right) \tag{2.52}$$

The non-dimensional variables are used to transform Eq. 2.51-2.52 to Eq. 2.53-2.54, and Eq. 2.46-2.46 to Eq. 2.55-2.56.

$$f(T)\, f_c \frac{dT}{d\xi} + \frac{2g(T)}{\xi} = \beta^2 E_c \left(Tf_c \frac{\gamma}{K} + 1\right)^{\frac{1}{\gamma}} \frac{d\mathrm{U}}{d\xi}(\xi - U) \tag{2.53}$$

$$\frac{d\mathrm{U}}{d\xi} + 2\frac{\mathrm{U}}{\xi} = \frac{f_c}{K + Tf_c\gamma}(\xi - U)\frac{dT}{d\xi} \tag{2.54}$$

$$f(T) = \frac{1}{3}\frac{3a_1^2 + 3(a_2 Tf_c)^2 + 6a_1 a_2 Tf_c + 2a_1}{(a_1 + a_2 Tf_c)^2} \tag{2.55}$$

$$g(T) = a_0 + \frac{Tf_c}{a_1 + a_2 Tf_c} \tag{2.56}$$

The system of differential equations shown in Eq. 2.57-2.58 is obtained by solving for derivative terms in Eq. 2.53-2.54. To numerically solve Eq. 2.57-2.58, the boundary conditions of Eq. 2.59, U_2, T_2 are needed, and the calculation procedure starts from $\xi = 1$ to $\xi = \varepsilon$ using the Runge-Kutta method. As a result, solving the system of differential equations yields the values of U, T at the surface of the cavity (when $\xi = \varepsilon$).

$$\frac{d\mathrm{U}}{d\xi} = \frac{2Uf(T)(K + Tf_c\gamma) + 2g(T)(\xi - U)}{\xi\beta^2 E_c \left(\frac{K + Tf_c\gamma}{K}\right)^{\frac{1}{\gamma}} (\xi - U)^2 - \xi f(T)(K + Tf_c\gamma)} \tag{2.57}$$

$$\frac{d\mathrm{U}}{d\xi} = \frac{2\beta^2 E_c \left(\frac{K + Tf_c\gamma}{K}\right)^{\frac{1}{\gamma}} U(K + Tf_c\gamma)(\xi - U) + 2g(T)(K + Tf_c\gamma)}{f_c\xi\beta^2 E_c \left(\frac{K + Tf_c\gamma}{K}\right)^{\frac{1}{\gamma}} (\xi - U)^2 - f_c\xi f(T)(K + Tf_c\gamma)} \tag{2.58}$$

$$U(\xi = \varepsilon) = \varepsilon \tag{2.59}$$

The equation for the relationship between S and T, Eq. 2.60, is derived from Eq. 2.46-2.49. By substituting the value of T at the cavity surface into Eq. 2.60, the value of S at the cavity surface can be obtained. From this, the stress applied on the penetrated surface of the projectile, which is equal to the σ_r at the cavity surface, can be calculated.

$$S = \frac{1}{3f_c} \frac{3Tf_c a_1 + 3a_2(Tf_c)^2 + 2a_0 a_1 + 2a_0 a_2 Tf_c + 2Tf_c}{a_1 + a_2 Tf_c} \tag{2.60}$$

2.4.1.2. Cracked-elastic region

The behavior of the elastic region is determined by the elastic wave equation with Hooke's law, as shown in Eq. 2.61-2.63. The dilatational velocity is given by Eq. 2.64. Non-dimensional variables are used to express Eq. 2.61, as shown in Eq. 2.65. The solution of Eq. 2.65 is given by Eq. 2.66, and A_0 and B_0 in Eq. 2.66 are determined by the boundary conditions of Eq. 2.67-2.68. The value of U in the elastic region can be obtained by Eq. 2.69, and the value of S in the elastic region can be derived from Eq. 2.62 using non-dimensional variables, as shown in Eq. 2.70. Therefore, by substituting $\xi = \beta_1 / \beta$ for the cracked-elastic interface into Eq. 2.69 and Eq. 2.70, S_3 and βU_3 can be calculated.

$$\frac{\partial^2 u}{\partial r^2} + \frac{2}{r}\frac{\partial u}{\partial r} - \frac{2u}{r^2} = \frac{1}{c_d^2}\frac{\partial^2 u}{\partial t^2} \tag{2.61}$$

$$\sigma_r = -\frac{E_c}{(1+v)(1-2v)}\left[(1-v)\frac{\partial u}{\partial r} + 2v\frac{u}{r}\right] \tag{2.62}$$

$$\sigma_\theta = -\frac{E_c}{(1+v)(1-2v)}\left(v\frac{\partial u}{\partial r} + \frac{u}{r}\right) \tag{2.63}$$

$$c_d^2 = \frac{E_c(1-v)}{(1+v)(1-2v)\rho_0} \tag{2.64}$$

$$(1-\alpha^2\xi^2)\frac{d^2\bar{u}}{d\xi^2} + \frac{2}{\xi}\frac{d\bar{u}}{d\xi} - \frac{2\bar{u}}{\xi^2} = 0 \tag{2.65}$$

$$\bar{u} = A_0 \alpha\xi - B_0 \frac{1-3\alpha^2\xi^2}{3\alpha^2\xi^2} \tag{2.66}$$

$$\bar{u}(\xi = 1/\alpha) = 0 \tag{2.67}$$

$$\sigma_\theta(\xi = \beta_1/\beta) = -f_t \tag{2.68}$$

$$U = \bar{u} - \xi d\bar{u}/d\xi \tag{2.69}$$

$$S = -\frac{E_c}{f_c(1+v)(1-2v)}\left[(1-v)\frac{\partial\bar{u}}{\partial\xi} + 2v\frac{\bar{u}}{\xi}\right] \tag{2.70}$$

The cracked-elastic surface is characterized by a discontinuity in the hoop components of Cauchy stress due to the absence of tensile stress in the cracked region. As a result, the values of S_4 and βU_4 at this interface can be determined using the Hugoniot jump conditions, which are based on momentum and mass conservation, as shown in Eq. 2.71-2.72.

$$S_4 = S_3 + \frac{f_t}{f_c}\frac{2(\beta_1 - \beta U_3)^2}{3-(\beta_1 - \beta U_3)^2} \tag{2.71}$$

$$\beta U_4 = \beta U_3 + \frac{6 f_c (1-2v)(\beta_1 - \beta U_3)}{[3-(\beta_1 - \beta U_3)^2]E_c} \tag{2.72}$$

The concrete material in the cracked region is considered to be linearly compressible because the hoop components of Cauchy stress become zero($\sigma_\theta = 0$). The solutions for S and U in the cracked region were proposed by Forrestal & Tzou (1997) and are given by Eq. 2.73 – 2.74. The integration coefficients D_0 and E_0 are determined by the values of S_4 and U_4, which are calculated from Eq. 2.71 – 2.72 and serve as the boundary conditions at the cracked-elastic interface, as shown in Eq. 2.75 – 2.76. At the cracked-plastic interface, the radial stress in the cracked region is equal to the unconfined compressive strength f_c. Thus, the equation for calculating β given in Eq. 2.77 can be obtained by solving the quadratic equation obtained by substituting Eq. 2.73 into the boundary conditions at the cracked-plastic interface.

$$S(\xi) = \frac{E_0}{\beta\xi} + D_0\left[1 + \frac{3}{(\beta\xi)^2}\right] \tag{2.73}$$

$$U(\xi) = \frac{-3f_c(1-2v)}{2E_c\beta}\left[\frac{E_0}{3} + \frac{E_0}{(\beta\xi)^2} + \frac{4D_0}{\beta\xi}\right] \tag{2.74}$$

$$D_0 = \frac{-6\beta_1^2[2\beta_1 f_c S_4 + E_c(\beta_1^2+3)(\beta U_4)/\{3(1-2v)\}]}{f_c(\beta_1^2-3)^2} \tag{2.75}$$

$$E_0 = \frac{\beta_1^2[f_c S_4 + 2E_c\beta_1(\beta U_4)/(1-2v)]}{f_c(\beta_1^2-3)^2} \tag{2.76}$$

$$\beta = \frac{E_0 + \sqrt{E_0^2 + 12D_0(1-D_0)}}{2(1-D_0)} \tag{2.77}$$

The values of S_1, T_1, and U_1 for the cracked-plastic interface can be derived by substituting β obtained from Eq. 2.77 and setting $\xi = 1$ in Eq. 2.78-2.80.

$$S_1 = \frac{f_c}{f_c} = 1 \tag{2.78}$$

$$T_1 = \frac{f_c}{3f_c} = \frac{1}{3} \tag{2.79}$$

$$U_1 = \frac{-f_c(\beta^2+3)(1-2v)E_0}{2E_c\beta^3} - \frac{6f_cD_0(1-2v)}{E_c\beta^2} \tag{2.80}$$

The boundary conditions of Eq. 2.78 – 2.80 are utilized to compute the boundary conditions of U_2 and T_2, which are essential to solve Eq. 2.57 – 2.58. In the cracked region, the concrete material is assumed to be linearly compressible, so the equation of state at the cracked-plastic interface is given by Eq. 2.81. On the other hand, in the plastic region, the equation of state can be derived from Eq. 2.49 and is expressed as shown in Eq. 2.82. Consequently, the values of U_2 and T_2 can be determined by using Hugoniot jump conditions and by applying Eq. 2.81 – 2.82, as demonstrated in Eq. 2.83 – 2.84.

$$T_1 f_c = \frac{E_c}{3(1-2v)}\left(1-\frac{\rho_0}{\rho_1}\right) \tag{2.81}$$

$$\rho_2 = \rho_0\left(T_2\frac{\gamma f_c}{K}+1\right)^{\frac{1}{\gamma}} \tag{2.82}$$

$$U_2 = 1 - \frac{\rho_1}{\rho_2}\left(1 - U_1\right) \tag{2.83}$$

$$S_1 f_c + \rho_1 U_1 c(U_1 c - c) = S_2 f_c + \rho_2 U_2 c\left(U_2 c - c\right) \tag{2.84}$$

2.4.1.3. Inverse calculation procedure

As explicit solutions for U and T at the cavity surface are difficult to obtain, a numerical inverse procedure is required to obtain them. The following steps describe the procedure:

1. Choose a value of β_1 and use bisection method to determine β that satisfies Eq. 2.77.
2. Calculate U_1, T_1, S_1, and use bisection method to determine U_2, T_2 that satisfy Eq. 2.84 using Eq. 2.81-2.83.
3. Determine ε that satisfies Eq. 2.59 using bisection method, then calculate a value of U at the cavity surface by solving Eq. 2.57-2.58 using the Runge-Kutta method from $\xi = 1$ to $\xi = \varepsilon$.
4. Calculate S at the cavity surface using Eq. 2.60 and V_c from the equation $V_c = \beta \varepsilon c_p$. Repeat the procedure for other values of β_1 to obtain the relationship between S at the cavity surface and V_c.

2.4.1.4. Results of the previous studies

Forrestal & Tzou (1997) obtained the relation between S at the cavity surface using the Mohr-Coulomb yield surface and linear equation of state derived from the triaxial compressive test of concrete conducted by Joy and Ehrgott (1993), as depicted in Figure 2.2. In contrast, Kong et al.(2017) utilized the hyperbolic yield surface obtained from Hanchak et al.(1992) and the Murnaghan equation of state derived from Gebbeken et al.(2006) to derive the relation between S at the cavity surface, as shown in Figure 2.3.

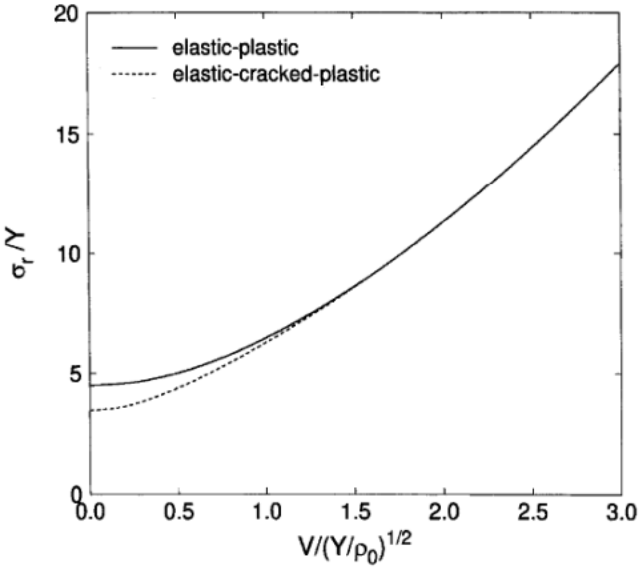

Figure 2.2 Radial stress versus cavity expansion velocity from Forrestal & Tzou (1997)

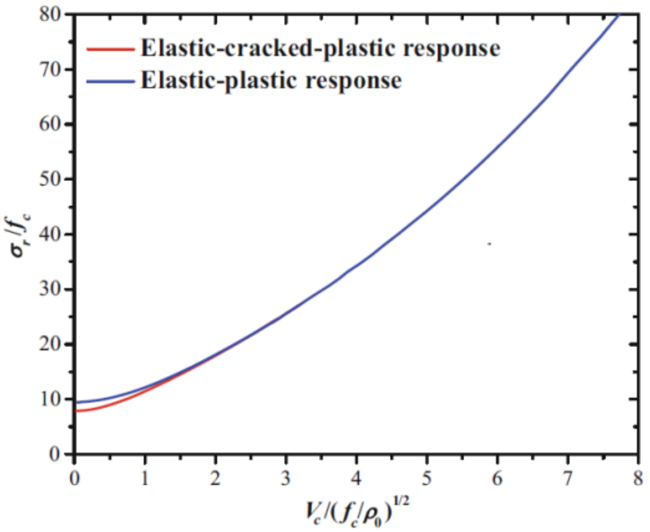

Figure 2.3 Radial stress versus cavity expansion velocity from Kong et al. (2017)

Forrestal & Tzou (1997) obtained the relation between S at the cavity surface using the Mohr-Coulomb yield surface and linear equation of state derived from the triaxial compressive test of concrete conducted by Joy and Ehrgott (1993), as depicted in Figure 2.2. In contrast, Kong et al.(2017) utilized the hyperbolic yield surface obtained from Hanchak et al.(1992) and the Murnaghan equation of state derived from Gebbeken et al.(2006) to derive the relation between S at the cavity surface, as shown in Figure 2.3.

$$\frac{\sigma_r}{f_c} = A + B\left(\frac{V_c}{f_c / \rho_0}\right)^2 \tag{2.85}$$

2.5. Concluding remarks

In this chapter, the range of design codes and guidelines commonly used in military and nuclear power plant (NPP) applications has been explored. Additionally, existing empirical and analytical formulae recommended in various design standards have been investigated. The investigation revealed that the proposed formulae incorporate a wide spectrum of variables.

Furthermore, it became clear that most of the proposed formulae need more capability to incorporate the influence of reinforcement on the behavior of concrete structures. This is a significant drawback, as reinforcement can significantly impact the structural response under loading conditions. Hence, there is a need for more accurate and reliable prediction formulae that can account for the influence of reinforcement. DMFC (2017) provides only wall thickness to protect structures from explosion and impact, and details about RC structure are specified to comply with KDS 14 20 00 (2021) criteria.

An analytic model using infinite plain concrete blocks is an approach that uses a theoretically simplified model as a proxy for a physical structure. However, it is difficult to fully model the complexity and variety of factors in a real structure like panels.

To address this issue, the next chapter will involve conducting impact testing and comparing the results with those predicted by the existing formulae. It is intended to verify the accuracy of these formulae and propose a more suitable formula that considers the influence of reinforcement.

3. Impact Test

3.1. Introduction

This chapter conducted a series of impact tests on RC targets to investigate the effect of rebar ratio on their behavior under high-velocity impacts over 300m/s. The tests were conducted using a 60 mm single-stage gas gun in the Extreme Performance Testing Center (EPTC). The test variables included specimen rebar ratio, projectile diameter, and impact velocity. A part of the reinforced concrete defense barrier was designed as a test specimen, and the specimens were prepared with different rebar ratios.

The test used two types of projectiles with diameters of 12.7mm and 37mm, with impact velocities ranging from 550m/s to 850m/s. The nose shape of the projectiles was modeled as an ogive. The bullets used in the study were designed to simulate those used in actual military operations. The projectile is made of hardened steel to simulate hard-type ammunition that deforms less after a collision. The penetration depth, scabbing limit, perforation limit, and failure mode were measured.

In data acquisition, various parameters were measured using a high-speed camera, including impact velocity and residual velocity. The mass change of the test specimens before and after impact and the mass and length change of the projectile before and after impact were also recorded. Additionally, rebar strain was measured using a rebar strain gauge.

3.2. Test variables

The test variables were determined for the current study to investigate the effect of rebar ratio on their behavior under high-velocity impacts over 300m/s. The overall identical designation is shown in Figure 3.1.

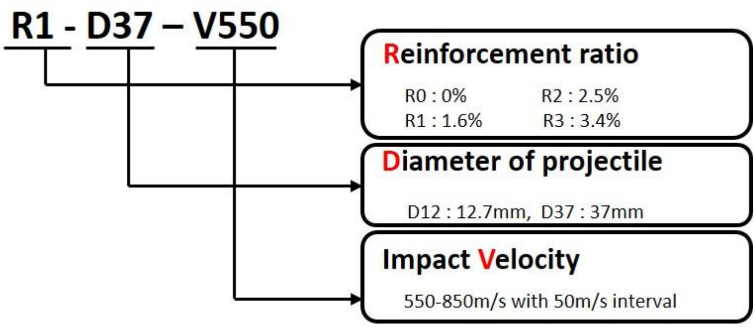

Figure 3.1 Identical designation

First, the rebar ratio was selected to assess the effect of the rebar ratio on the impact resistance performance. The RC target was designed by gradually increasing the rebar ratio from unreinforced concrete to the rebar ratio of the nuclear power plants, which shows the highest rebar ratio among ground structures. In this study, the specimens were categorized into four groups based on their rebar ratios, which R0, R1, R2, and R3 were denoted, corresponding to reinforcement rates of 0%, 1.6%, 2.5%, and 3.4%, respectively.

Next, the projectile's diameter was selected as the experimental variable to determine the difference in impact resistance performance based on the size of the projectile. In this study, two types of projectiles with diameters of 12.7mm and 37mm were adopted as experimental variables. D12 and D37 were denoted, corresponding to projectile diameters of 12.7mm and 37mm, respectively. The test was designed to utilize a 37mm projectile as the primary test variable and a 12.7mm projectile as a secondary variable to examine the effect of projectile size.

Based on MIL-STD-662F (1997) in Table 3.2, the impact velocity was chosen as the final experimental variable. This variable was selected to assess the effect of impact velocity on the impact resistance performance of the RC targets. In addition, this impact speed range was planned to be relatively high to account for the range of speeds used by military projectiles beyond the typical airplane impact speed range.

The impact velocity represents the remaining velocity at a specific distance according to the US Department of Defense test method standard ranging from 550m/s to 850m/s in increments of 50m/s for 6 cases. The test standard defines the projectile ranges from 100m to 1,000m. The impact velocity of 550, 600, 650, 700, 750, and 850 m/s were labeled V550, V600, V650, V700, V750, and V850, respectively.

Table 3.1 Remaining velocity at specific distance (MIL-STD-662F, 1997)

Distance (m)		0	100	200	300	400	500	600	700	800	900	1000
Velocity (m/s)	37mm AP M74	884	841	802	765	727	692	658	628	596	567	538
	Cal.50 AP M2	896	853	817	780	745	707	670	640	606	573	543

The following Table 3.2 shows the total test program. A total of 24 tests were planned for six different impact velocities and four different rebar ratios. For the D37 projectile, tests were planned for impact velocity ranging from 550 m/s to 750 m/s, and for the D12 projectile, tests were planned for a single section speed of 850 m/s.

Table 3.2 Test program

No	I.D.	Rebar ratio (%)	Projectile Velocity (m/s)	EA	No	I.D.	Rebar ratio (%)	Projectile Velocity (m/s)	EA
1	R0-D37-V550	0	550	4	13	R0-D37-V700	0	700	4
2	R1-D37-V550	1.6			14	R1-D37-V700	1.6		
3	R2-D37-V550	2.5			15	R2-D37-V700	2.5		
4	R3-D37-V550	3.4			16	R3-D37-V700	3.4		
5	R0-D37-V600	0	600	4	17	R0-D37-V750	0	750	4
6	R1-D37-V600	1.6			18	R1-D37-V750	1.6		
7	R2-D37-V600	2.5			19	R2-D37-V750	2.5		
8	R3-D37-V600	3.4			20	R3-D37-V750	3.4		
9	R0-D37-V650	0	650	4	21	R0-D37-V850	0	850	4
10	R1-D37-V650	1.6			22	R1-D37-V850	1.6		
11	R2-D37-V650	2.5			23	R2-D37-V850	2.5		
12	R3-D37-V650	3.4			24	R3-D37-V850	3.4		

3.2.1. Projectile preparation

Projectiles were designed by simulating the kinetic energy ammunitions considered ogive-nose steel projectiles. Table 3.3 presents a list of the primary kinetic energy projectiles used in the military, ordered by diameter. Generally, projectiles with a diameter of 40 mm or greater are intended to cause damage through gunpowder explosions. In contrast, those utilizing pure kinetic energy are used with a diameter of 40 mm or less. For this reason, in the present study, the 37 mm projectile, which is a large diameter kinetic energy projectile and is known to be used in the ACE test, as well as the 12.7 mm projectile, were selected to examine the test object conditions according to projectile size.

Table 3.3 Types of kinetic energy ammunitions

Diameter [mm]	Representative firearms		Max. velocity [m/s]	Note
5.56		K-1, K-2, SCAR-L	820	-
7.62		DD-5, M-60	884	-
12.7		K-6(K200)	928	ACE test, MIL-STD-662F
20		M61(K263)	1,050	MIL-STD-662F
30	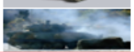	K-30	1,080	-
37		M1	850	ACE test, MIL-STD-662F
40		K21, K-4	1,005	APFSDS(Kinetic E.)

The design of the projectile was based on TM 9-1904 (1944), and it takes the form of a cylinder to simulate the body of the Cal.50 AP M2 and 37mm AP M74. The cylinder-type dimensions are Ø10.9 × 43.4 mm and Ø37 × 123 mm for the 12.7 mm and 37 mm projectiles, respectively, as depicted in Figure 3.2. To ensure similarity with a hard-type armor-piercing bullet, the bullets were made of AISI 4340 steel, using Forrestal et al. (1996) as a reference for their properties. The final product is presented in Figure 3.3. Both projectiles feature an ogive nose shape with a CRH value of approximately 3, "Caliber Radius Head." This type of nose shape reduces air resistance during high-speed flight, thus enhancing the projectile's flight distance and accuracy. Such conditions are commonly used in high-speed flight vehicles like missiles.

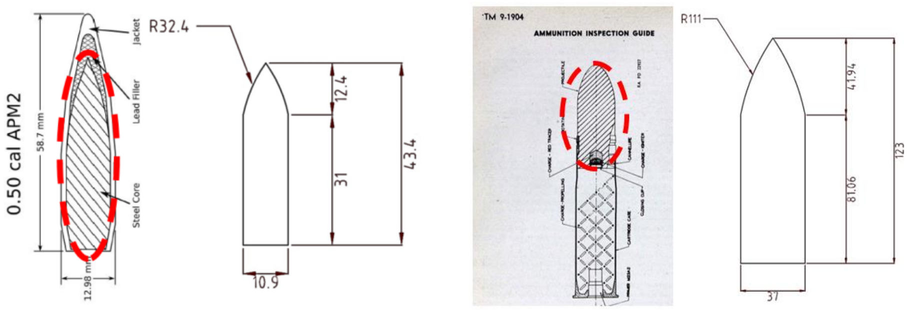

(a) (b)

Figure 3.2 Design of projectile

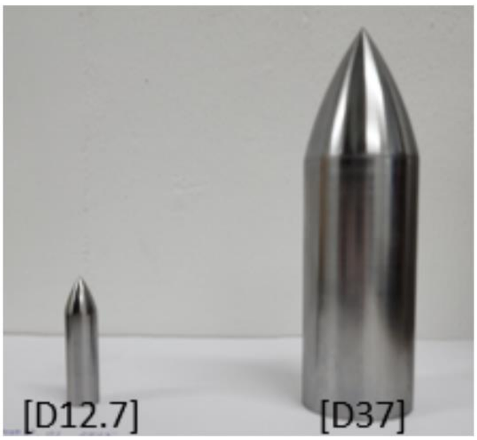

Figure 3.3 Manufactured and processed projectile

A sabot is necessary to ensure that the projectile remains on course despite the difference in diameter between it and the launch tube of a 60mm gas gun. However, the sabot colliding with the steel separator in the blast tank can negatively impact the projectile's trajectory. Therefore, an alternative approach is necessary to minimize the sabot's impact on the projectile during separation, allowing it to maintain its straightness. This study utilized a five-piece detachable polycarbonate sabot made of polycarbonate material, as depicted in Figure 3.4. The design allowed the projectile-sabot to break into five pieces through resistance to the air medium inside the blast tank, with the sabot separating before colliding with the steel separator, thus minimizing the impact on the projectile's straightness. The drawing design for this is shown in Figure 3.5.

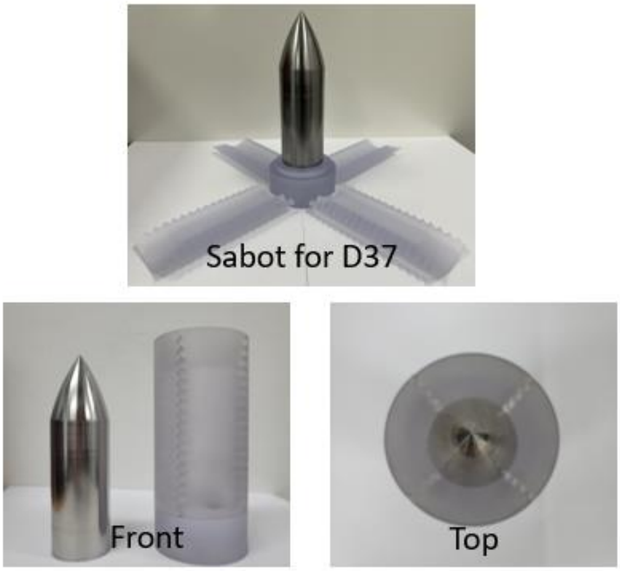

Figure 3.4 Manufactured and processed 5-piece sabot

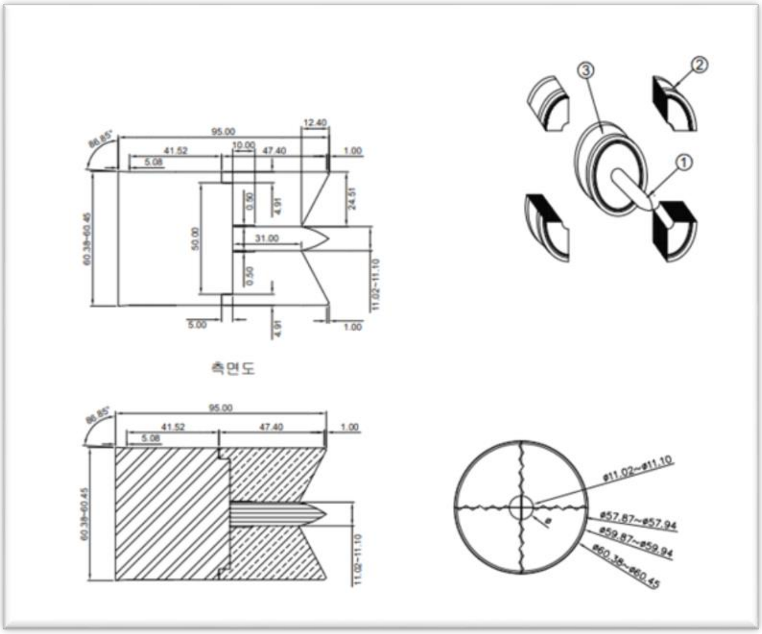

(a)

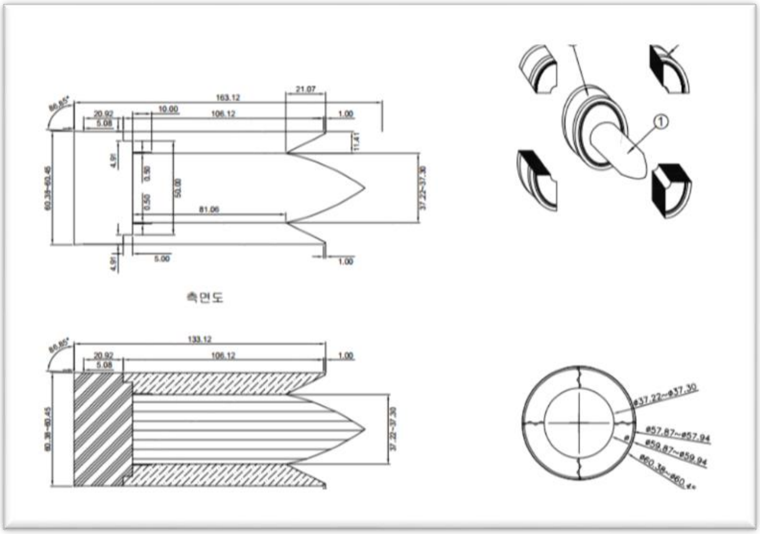

(b)

Figure 3.5 Design drawing of sabot for projectile

3.2.2. Specimen preparation

The RC targets were designed by simulating a protective reinforced concrete wall. As shown in Figure 3.6, the test specimens were each 600 mm long by 600 mm wide, the maximum size of a specimen that can settle in the target tank of a 60 mm single-stage gas gun.

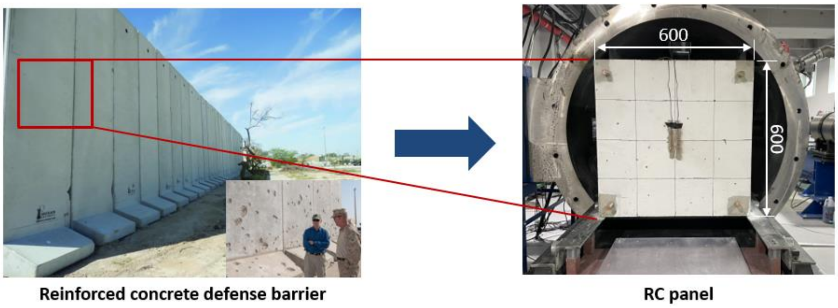

Figure 3.6 Test configuration of RC target

In the Korean military, the Defense Military Facilities Criteria (DMFC 2-20-10, 2017) only specifies the required wall thickness for achieving blast and impact resistance. For more detailed specifications, such as steel reinforcement, it is recommended to refer to the Korean Design Standards for Concrete Structures (KDS 14 20 00: 2021). These standards provide more specific and detailed guidelines for designing and constructing reinforced concrete structures that meet safety requirements.

To set the validity of the wall thickness, the major local damage prediction equations were applied, and the expected failure modes were derived. As the impact velocity increased, the thickness of the wall was set to allow for the progressive occurrence of the destruction modes 'penetration-scabbing-perforation.'

Table 3.4 Predicted failure mode of 500mm RC target for 37mm projectile

Striking Velocity (m/s)	Expected destruction mode								
	Military				Non-military				
	ACE	Conwep	UKAEA	NDRC	CEA-EDF	Chang	CRIEPI	Degen	Bechtel
650	Pen.	Scabbing	Pen.	Pen.	-	Pen.	Pen.	-	Pen.
700	Scabbing	Perf.	Pen.	Pen.	-	Pen.	Pen.	-	Pen.
750	Scabbing	Perf.	Pen.	Scabbing	-	Pen.	Pen.	-	Pen.
800	Perf.	Perf.	Pen.	Perf.	-	Pen.	Pen.	-	Pen.
850	Perf.	Perf.	Pen.	Perf.	No Perf.	Pen.	Pen.	Perf.	Pen.

Table 3.4 presents the predicted failure modes for a 37 mm projectile impacting a reinforced concrete target with a thickness of 500 mm and a concrete compressive strength of 52 MPa, categorized by impact velocity. In the prediction equations recommended by NPP design standards such as CEA-EDF(Berriaud C et al., 1978), Chang(1978), and CRIEPI(Kojima, 1991), the expected failure mode was mostly penetration even as the impact velocity increased, but in the equations recommended by military design standards such as ACE(1946), Conwep(Hyde D, 1992), and NDRC(1946), a gradual failure mode was expected to occur as the impact velocity increased from low to high for a 37mm projectile when the wall thickness was set to 500mm. Therefore, the thickness of the RC target to be applied in the experiment was determined to be 500mm.

Finally, four specimens were designed with a 600×600×500mm dimension, as shown in Figure 3.7. The compressive strength of concrete was set at 52.5 MPa, while the rebar ratio ranged from 0 to 3.4%. The rebar ratio is expressed as a percentage, representing the ratio of the cross-sectional area of the reinforcement to the cross-sectional area of the concrete, as shown Table 3.5. The yield strength of the rebar was 464 MPa, with a diameter of 19mm. The concrete and rebar strengths were referenced from the APR 1400 properties. The projectiles were aimed away from direct contact with the rebar to conduct experiments in critical impact situations. Before the concrete was poured, eight rebar strain gauges were attached to the front and rear of the test specimen, four each, to obtain the strain time history of the rebar by projectile impact.

Table 3.5 Details of reinforcement steel (D19, SD400)

Contents	Rebar ratio 1.6%		Rebar ratio 2.5%		Rebar ratio 3.4%	
	Horizontal	Vertical	Horizontal	Vertical	Horizontal	Vertical
Diameter, mm	19.05	19.05	19.05	19.05	19.05	19.05
Area of rebar, mm^2	285.02	285.02	285.02	285.02	285.02	285.02
Target depth, Mm	500	500	500	500	500	500
Quantity of Rebar	4	4	6	6	8	8
Rebar spacing, mm	160	160	100	100	75	75
1-layer rebar ratio(EWEF), %.	0.404	0.404	0.647	0.647	0.863	0.863
ρ_{total}	1.62		2.59		3.45	

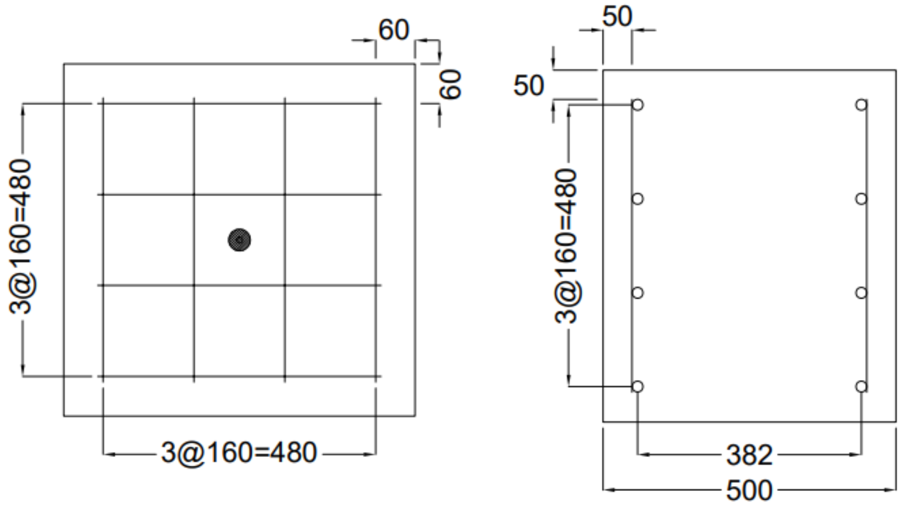

(a) Rebar ratio 1.6%

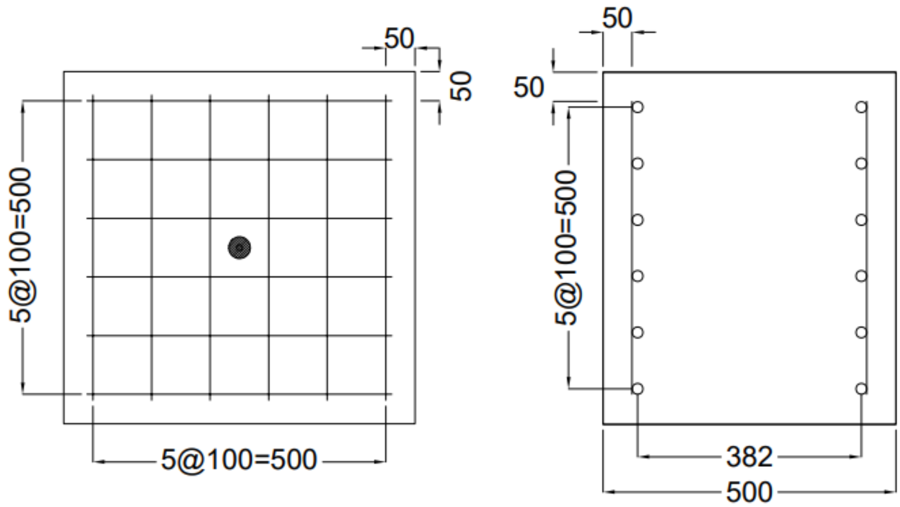

(b) Rebar ratio 2.5%

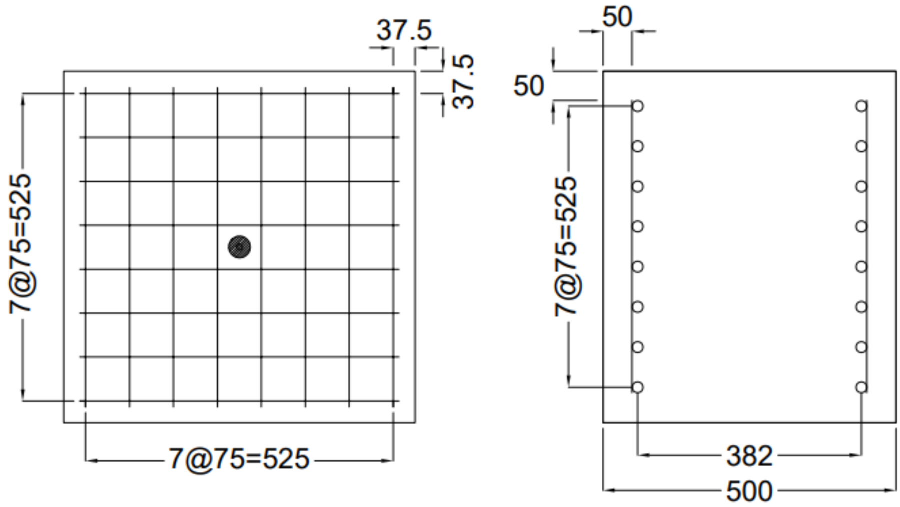

(c) Rebar ratio 3.4%

Figure 3.7 Design of RC target

In this study, the specimens were assembled for each rebar ratio according to the design presented in Figure 3.8. The concrete was poured and cured following the procedure illustrated in Figure 3.09. Finally, the specimens were fabricated by the process shown in Figure 3.10.

Figure 3.8 Rebar assembly

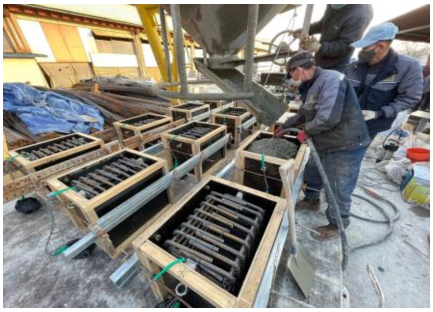

(a) Concrete pouring

(b) Concrete curing

Figure 3.9 Concrete pouring and curing

Figure 3.10 Creation and setting of test specimens

3.3. Material tests

3.3.1. Concrete

The mix proportion of concrete is presented in Table 3.6, which specifies the use of Type I Portland cement and a maximum aggregate size of 25mm. The water-cement ratio employed was 0.3, while the average slump was 160mm. Concrete cylinders with dimensions of 150x300mm were placed on site and air-cured under conditions similar to those of the RC beams. Compression tests were then carried out following the standard test method (ASTM C39, 2014).

The compression test was performed using the Universal Testing Machine (UTM) located at Seoul National University, as illustrated in Figure 3.11. During the test, the concrete cylinders with dimensions of 150x300mm were placed between the compression plates of the UTM, which exerted a compressive force on the specimens until they failed.

The test results were recorded in Table 3.7, which provides information about the compressive strength and modulus of elasticity of the concrete. The elastic modulus was determined by measuring the slope of a line drawn from zero stress to 0.45 times the compressive strength of the concrete, using the stress-strain curve as specified in the ACI 318-19 standard (2019).

Figure 3.11 Compression test of concrete cylinder

Table 3.6 Mix proportion of concrete

f_{ck} (MPa)	Unit weight (kg/m^3)					
	Water	Cement	Fine aggregate	Coarse aggregate	Admixture	Air content (%)
42	167	540	681	993	4.59	3.5

The concrete's average compressive strength was measured and found to be 52.5MPa. To obtain this value, the displacement of the concrete in response to the applied load was measured using Linear Variable Differential Transducers (LVDTs). Subsequently, the strains were calculated in the Bernoulli region (B-region) range, where the discontinuity region (D-region) could be excluded from consideration.

Table 3.7 Compression tests result of concrete cylinder(f_{ck} = 42MPa)

Test Date (Age)	f_{cu} (MPa)				E_c (MPa)
	#1	#2	#3	Average	
21.12.14 (7)	30.8	31.3	31.2	31.1	17,278
22.1.7 (31)	44.3	44.1	155	43.7	21,455
22.2.10 (65)	53.7	52.9	52.9	53.2	20,469
22.2.23 (78)	51.8	52.2	52.9	52.3	19,914
22.3.10 (93)	52.9	53.3	52.3	52.8	20,270
22.3.28 (111)	51.8	53.4	52.3	52.5	19,995
22.4.15 (129)	52.2	51.9	52.6	52.2	20,301

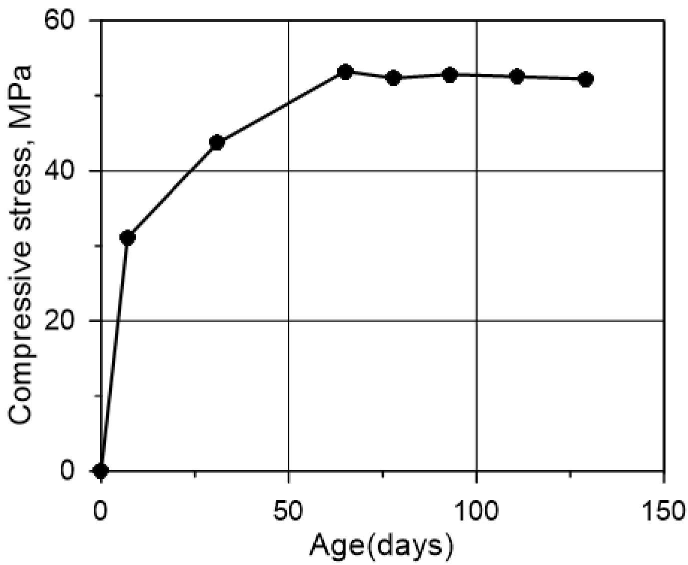

Figure 3.12 Compression strength by age

Because the impact test lasted for a considerable period, the concrete compressive strength tests were conducted every two weeks to monitor changes in the concrete's strength over time. The results of these tests revealed that, on average, the concrete's compressive strength was consistently 52.5 MPa after reaching a day of 65, as depicted in Figure 3.12.

Table 3.8 Static material properties of concrete

Compressive strength, MPa	Elastic modulus, MPa	Poisson’s ratio	Density, kg/m^3
52.5	20189	0.18	2350

3.3.2. Reinforcing steel bars

The RC targets were fabricated using deformed reinforcing steel bars of SD400 grade with a diameter of 19mm (D19), selected from standard products. The material properties of these bars were determined following ASTM 370-18 (2019) test method.

Three specimens were subjected to tension tests to evaluate their performance under uniaxial tension, as depicted in Figure 3.13. These tests were carried out using a Universal Testing Machine (UTM) at Seoul National University, and strain measurements were obtained using a Video Extensometer machine.

The loading rate was set at 1mm/min, as per the standard test method. The tests were conducted until the bars ruptured, and the results, as presented in Table 3.9 and Figure 3.14, were analyzed.

Table 3.9 Tension tests result of reinforcing steel bars

Diameter	f_y (MPa)				ε_y	f_u (MPa)	E_s (MPa)
	#1	#2	#3	Avg.			
D19	459	467	467	464	0.0023	595	200,000

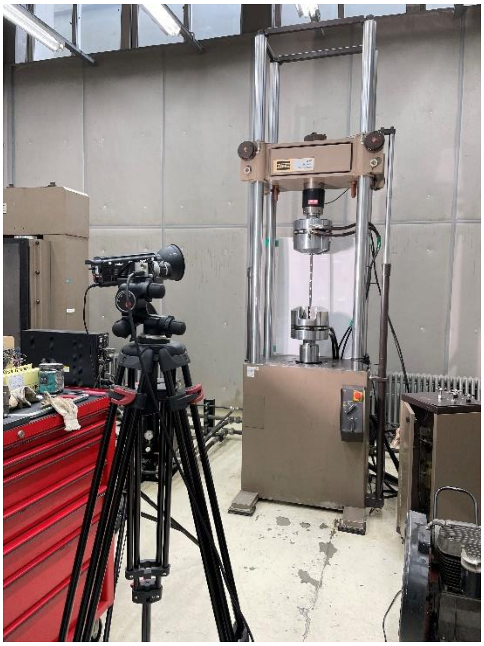

Figure 3.13 Uniaxial tension test of reinforcing steel bars

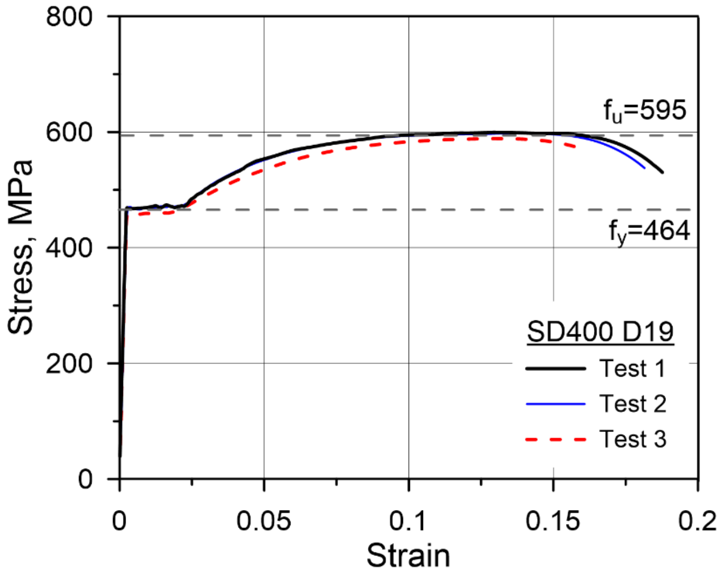

Figure 3.14 Stress-strain curve of reinforcing bars: D19-SD400

3.4. Test procedures

3.4.1. Test setup

This study conducted impact tests on the RC targets and the projectile at the Extreme Performance Testing Center (EPTC) located at Seoul National University, using a 60 mm Single Stage Gas Gun (SSGG). As depicted in Figure 3.15, this particular SSGG model can perform impact tests within a range of projectile diameters less than 60 mm, projectile masses less than 5 kg, and impact velocities less than 1,200 m/s.

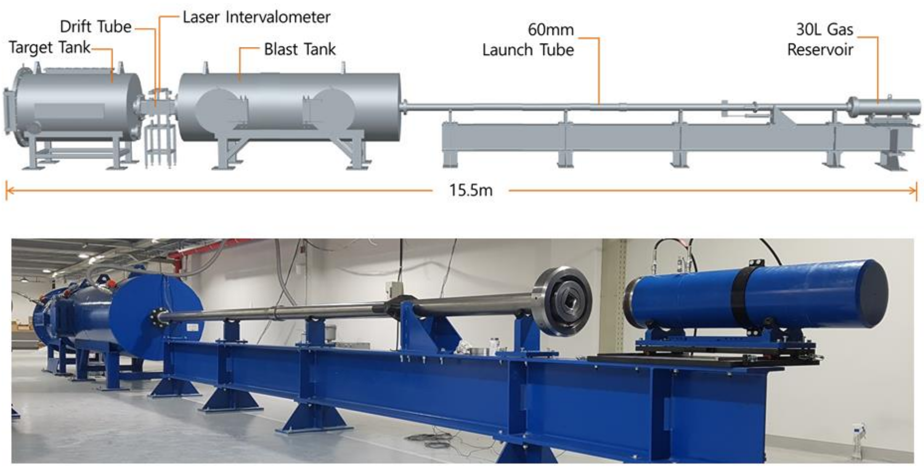

Figure 3.15 60mm single stage gas gun in EPTC

The procedure for conducting an impact test using the 60 mm SSGG is outlined in Figure 3.15. To begin, the projectile is installed with a sabot, which helps to maintain its trajectory when launched by the 60 mm SSGG. The projectile-sabot combination is then inserted into the launch tube. Compressed air in the 30L gas reservoir accelerates the projectile until it reaches the desired impact velocity as it passes through the launch tube. Upon reaching the blast tank, the sabot is separated from the projectile by colliding with the sabot separator, a steel plate with a hole sized between the projectile's diameter and the sabot's diameter. The projectile's velocity is measured between the blast tank and the target tank using laser interrupt equipment after the sabot is separated. Finally, the projectile passes through the drift tube and collides with the RC targets fixed in the target tank. Furthermore, to observe the collision position, speed, and angle of the RC targets and projectile, a high-speed camera is installed in the observation window of the target Tank.

The jig for fixing the test specimens inside the target tank of the high-speed gas gun equipment should be easy to install, and select the test piece variably according to the thickness of the specimen. It should not interfere with the shooting path with a high-speed camera. For this purpose, a 4 point fixed jig that holds the four corners of the test piece was utilized, as shown in Figure 3.16. The final setup of the specimen inside the target tank is shown in Figure 3.17.

Figure 3.16 Specimen Fixture Jigs

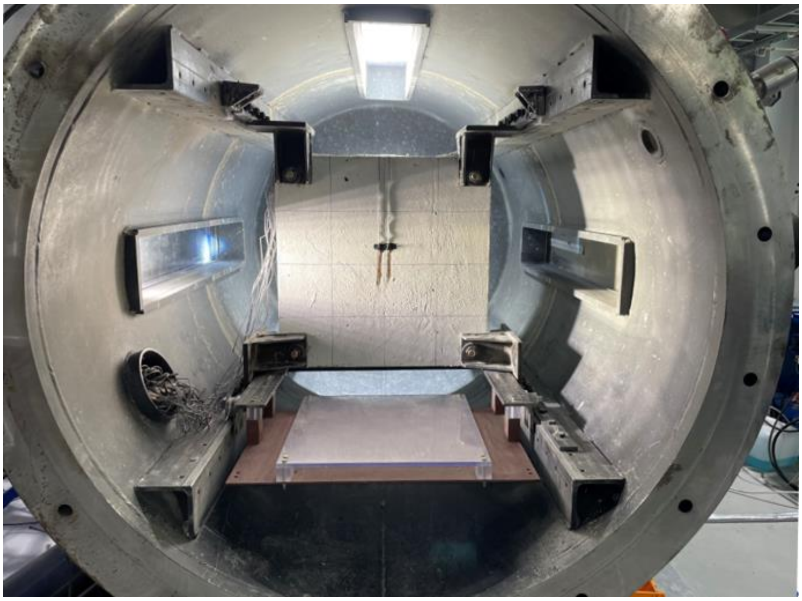

Figure 3.17 Specimen fixation inside the target tank: 4 point fixed

3.4.2. Measurement and data acquisition

Various parameters were measured during data acquisition, such as failure mode, depth of penetration, impact velocity and residual velocity, the mass change of the test specimens before and after impact, and the mass and length change of the projectile before and after impact. Additionally, rebar strain was also measured.

3.4.2.1 Impact and residual velocity

The impact velocity was measured using a laser interferometer and a high-speed camera system. First, a laser interferometer was installed in the drift tube between the blast tank and the target tank to measure the time difference between the projectile's passage through each laser, as shown in Figure 3.18. This information was then used to calculate the projectile's velocity by dividing the time difference by the distance between the lasers.

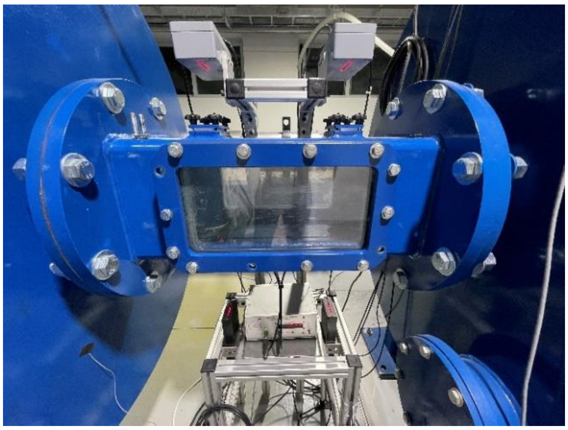

Figure 3.18 The laser interferometer system

Figure 3.19 High-speed camera settings

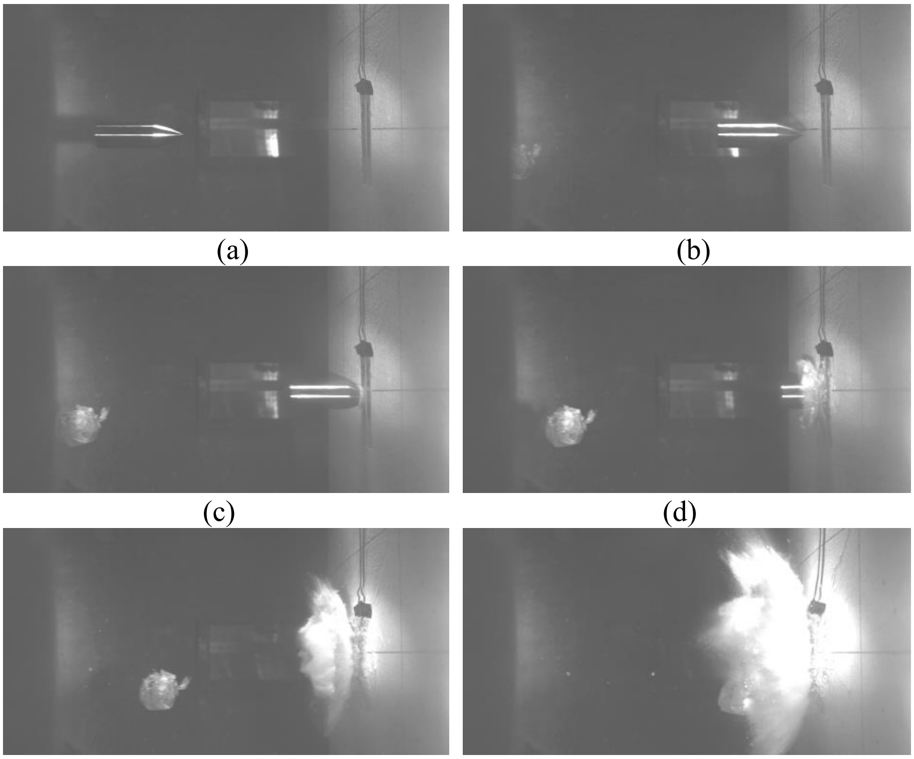

(a) (b)

(c) (d)

(e) (f)

Figure 3.20 High-speed camera images: impact velocity

Moreover, the high-speed camera system was installed in the target tank's observation window to capture the projectile's passage and record its velocity, as shown in Figure 3.19. The laser interferometer system was also programmed to transmit a trigger signal to the high-speed camera when the projectile passed through the drift tube, allowing for simultaneous measurement of impact velocity using both systems. By sending a trigger signal to the high-speed camera, images at 0.1 msec intervals are captured, as demonstrated in Figure 3.20. The time per frame and the distance traveled by the projectile are then calculated to determine the impact velocity of the projectile through a similar process.


(a)


(b)

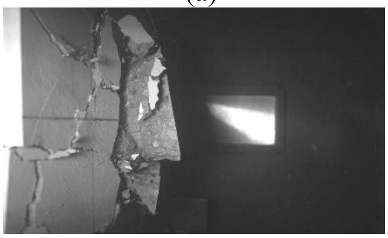
(c)

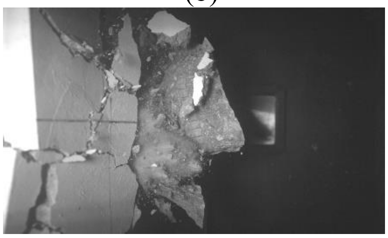
(d)

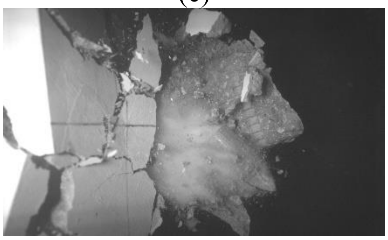
(e)

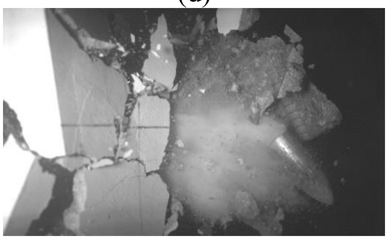
(f)

Figure 3.21 High-speed camera images: residual velocity

In the measurement of post-penetration residual velocity, a high-speed camera was placed behind the test specimen, as shown in Figure 3.21. Upon receiving a trigger signal, the camera captured images, and the residual velocity of the projectile was calculated by analyzing the time per frame and the distance traveled by the projectile, using a similar method as the one employed in estimating the impact velocity.

However, measuring the residual velocity through high-speed cameras can be challenging due to debris, such as dust or concrete fragments generated after penetration, which can obscure the projectile and make it difficult to obtain accurate measurements. The residual velocity was also measured using a Flash X-ray device to overcome this issue, as shown in Figure 3.22. The flash X-ray equipment emits short bursts of X-rays that can penetrate through objects and capture images of their internal structures. The collision velocity of the objects can be calculated by analyzing the time intervals between two pictures of the things at different positions.

Figure 3.22 Flash X-ray system

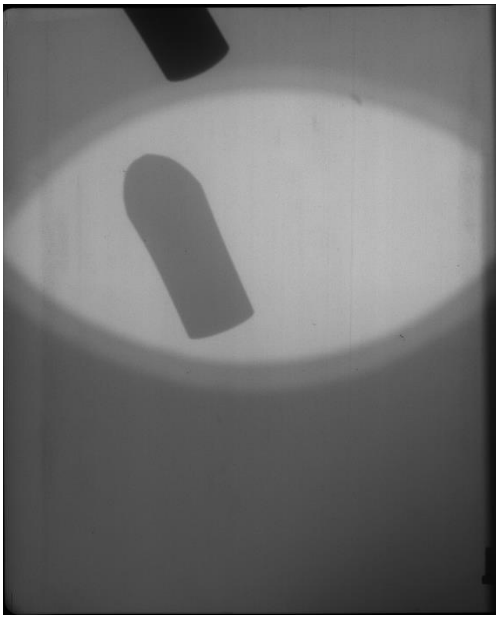

Figure 3.23 Flash X-ray image: residual velocity

Impact velocity imaging using Flash X-ray equipment has the advantage of seeing through the object and capturing the shape of the projectile among many debris. However, compared to high-speed cameras that can keep the aperture open for an extended period, Flash X-ray equipment has a limitation where capturing the target object is challenging since the shutter must be triggered by precisely capturing the moment when the projectile passes.

3.4.2.2. Failure mode and penetration depth

Penetration depth is significant in assessing the resistance of concrete to localized damage such as impact. By measuring the penetration depth, researchers can obtain a better understanding of the damage mechanisms that are occurring within the concrete. This information can then be used to improve the durability and performance of the concrete and to develop effective protective measures to prevent damage.

In addition, penetration depth measurements can be used to evaluate the performance of different types of concrete. For example, the penetration depth of concrete samples with varying strengths, compositions, or curing conditions can be measured and analyzed to determine their relative resistance to localized damage.

In this study, the depth of penetration was measured using a caliper and a laser pointer ruler, as shown in Figures 3.24-3.25.

Figure 3.24 Measurement of penetration depth: Caliper

Figure 3.25 Measurement of penetration depth: Laser pointer ruler

3D scanners have emerged as a valuable tool for measuring failure modes in local damage of concrete. 3D scanners can capture detailed images of concrete surfaces and provide high-resolution data on the geometry and topography of the surface. This capability accurately measures the depth and extent of damage sustained by the concrete in three dimensions.

The advantage of 3D scanners is particularly pronounced in measuring localized damage failure modes such as cracking or spalling. These forms of damage are difficult to measure accurately using traditional methods such as visual inspection or two-dimensional imaging techniques. However, 3D scanners allow researchers to capture detailed images of the surface and accurately measure the depth, width, and length of individual cracks and the extent of spalling or other forms of damage.

In addition to providing precise damage measurements, 3D scanners enable researchers to create digital models of concrete surfaces and analyze the data using advanced computational methods. This allows for greater insight into the underlying mechanisms of failure and identifying factors contributing to the development and propagation of local damage.

Overall, the use of 3D scanners is a powerful tool for measuring local damage failure modes in concrete, as shown in Figure 3.26. It enables accurate and detailed damage measurements and provides a valuable platform for advanced computational analysis of the underlying failure mechanisms.

Figure 3.26 Measurement of failure mode: 3D scanner

The process of using a 3D scanner to obtain information on failure mode and depth of penetration is as follows.

1) The first step is to acquire data by scanning the object or surface of interest using a 3D scanner, as shown in Figure 3.27. The scanner uses laser or light-based technology to capture high-resolution data points

on the surface, creating a point cloud. This study collected data from six stations during each measurement cycle.

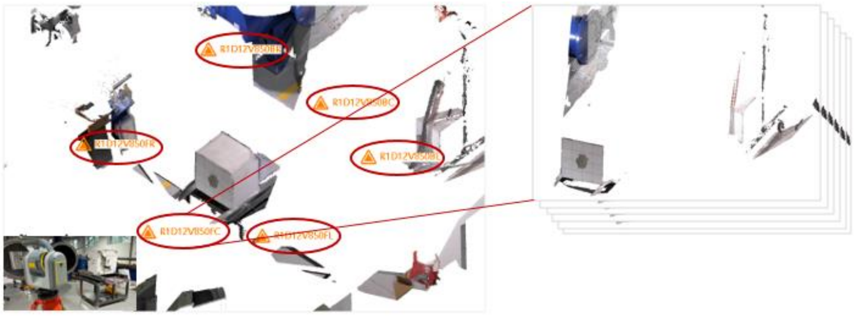

Figure 3.27 Acquisition of scanned data using 3D scanner

2) Matching scanned data and creating point clouds: Next, the data acquired from the scanner is matched and assembled to create a complete point cloud. This point cloud provides a detailed 3D representation of the surface being scanned.

Figure 3.28 Matching scanned data and creating point clouds

3) Matching scanned data before & after the impact test: If the surface is being tested for damage, such as in an impact test, the point cloud

acquired before the test is compared to the point cloud obtained after the test to identify any changes in the surface.

4) Comparative analysis of scanned data before and after shooting: The final step involves a comparative analysis of the scanned data before and after the impact test, as shown in Figure 3.29. This analysis can quantify the extent of damage sustained by the surface and provide insights into the underlying failure mechanisms.

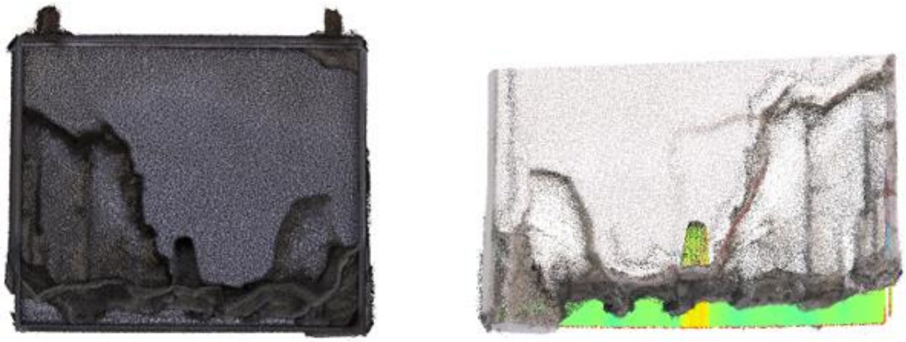

Figure 3.29 Matching scanned data and creating point clouds

Overall, using 3D scanners is a powerful tool for measuring local damage failure modes in concrete. The precise measurement procedure enables accurate and detailed damage measurements and provides a valuable platform for advanced computational analysis of the underlying failure mechanisms.

3.4.2.3. Mass of specimen

The mass of the specimen was measured before and after impact, allowing for a quantitative assessment of the mass loss incurred during the test. The method involved measuring the mass of the specimen before and after the impact, and the difference between the two measurements was used to calculate the mass loss.

The mass of each specimen was measured before and after the impact test using a digital scale, as shown in Figure 3.30. The results showed that the method could provide important information for evaluating the extent of damage caused by impact loading.

Figure 3.30 Mass of specimen measurement after impact

3.4.2.4. Mass and length of projectile

The study conducted quantitative measurements on the changes in mass and length of the projectile after the impact test, which was influenced by the impact velocity and rebar ratio. The data obtained from these measurements were then used to determine the extent of loss experienced by the projectile after the collision. It was important to verify that the hard-type projectiles made of steel did not undergo significant changes after the collision, as indicated by theoretical considerations.

A scale was used to measure the change in mass, as illustrated in Figure 3.31, while a caliper, shown in Figure 3.32, was utilized to measure the change in length.

Figure 3.31 Mass of projectile measurement after impact

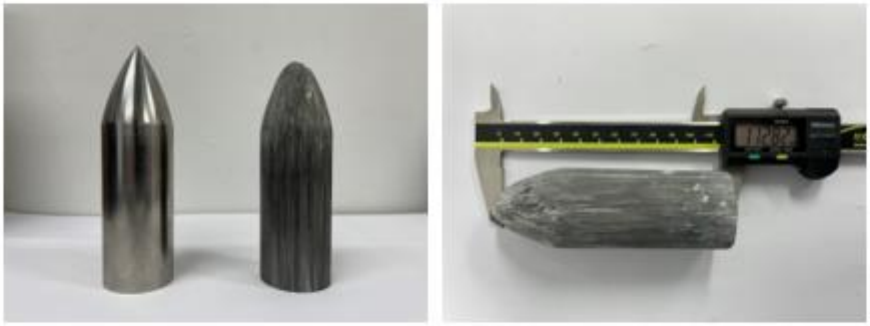

Figure 3.32 Mass of projectile measurement after impact

3.4.2.5. Strain of rebar

To measure the deformation of the rebar over time during impact testing, eight strain gauges were installed on each test piece; four on the front and four on the back, as depicted in Figure 3.33. The strain gauges were used to collect data on the strain of the rebar at different time points during the test.

The collected data was then analyzed using Debetron equipment to obtain the time-dependent strain of the rebar, as illustrated in Figure 3.34. Debetron is a brand of equipment used for measuring dynamic strain in materials under high strain rates. It uses strain gauges, sensors that measure a material's deformation by detecting changes in electrical resistance, to capture data during an impact test. The data is then used to analyze the strain and deformation of the material over time.

Figure 3.33 Strain gauge attachment

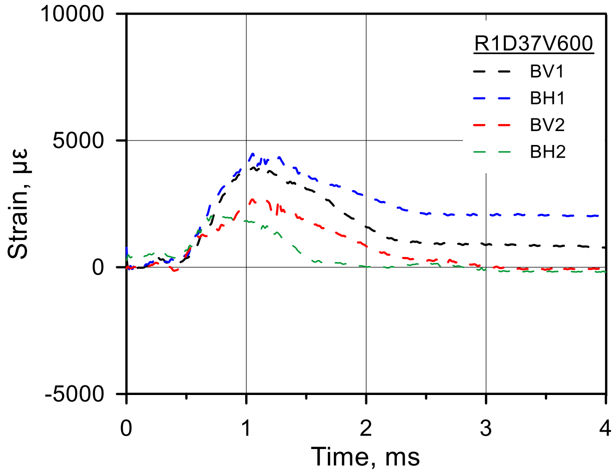

Figure 3.34 Strain of rebar by impact test: R1D37V600

3.5. Concluding remarks

This chapter provides a detailed description of the experimental programs conducted in this study. The experimental design process began with identifying the test variables and testing conditions, followed by the design of the test specimen. The impact test program was then developed, and preparations for the test were made, including preparing the projectiles and the specimens themselves. Material tests were conducted to ensure the quality and consistency of the specimens.

The test procedures were then carried out following the test program, and measurements and data acquisition were performed using the designated equipment. A detailed explanation of the test setup was also provided to help readers understand the experimental process.

This chapter aims to provide a detailed overview of the experimental procedures used in this study, to facilitate a clear understanding of the methodology.

4. Test results and discussion

4.1. Introduction

This chapter presents an experimental analysis of the impact resistance performance of reinforced concrete targets. The impact test was conducted to measure various parameters, including the yawing angle, impact velocity, failure mode, mass loss of specimen and projectile, penetration depth, scabbing limit, perforation limit, and residual velocity of the projectile. The experimental variables were varied to analyze their influence on the impact resistance performance of the targets. The results of the collision test were summarized in Table 4.1-4.2, providing a comprehensive understanding of the performance of the reinforced concrete targets under impact loading.

This includes an analysis of the damage and failure modes observed during the tests and an evaluation of the correlation between the experimental results and the existing prediction equations. Based on this analysis, modifications to the prediction equations are proposed to account for the effects of reinforcement. These proposed modifications are then validated against the experimental results.

The findings of this study can be useful for advancing the development of localized damage prediction equations for reinforced concrete structures that are more precise and dependable.

Table 4.1 Result of impact test for 37mm projectile

Designation		Yaw (°)	Striking Velocity(m/s)			Failure mode				Specimen mass(kg)			DOP (mm)	Residual Velocity (m/s)
			Target	Cal.	Measure	Empirical Formula			Test	Before (A)	After (B)	|B-A| /A, %		
						ACE	Conwep	NDRC						
#1	R0D37V550	1.3u	550	512	535	Pen.	Pen.	Pen.	Pen.	419.0	destroyed	X	X	-
#2	R1D37V550	6.4d			533				Pen.	441.5	366.5	17.0	233	-
#3	R2D37V550	5.1u			535				Pen.	454.5	389.5	14.3	212	-
#4	R3D37V550	0.9d			536				Pen.	472.5	420.0	11.1	217	-
#5	R1D37V600	1.6u	600	575	600	Pen.	Pen.	Pen.	Pen.	438.0	339.0	22.6	281	-
#6	R2D37V600	1.4u			600				Pen.	452.0	388.5	14.1	278	-
#7	R3D37V600	0			596				Pen.	468.0	420.5	10.1	254	-
#8	R0D37V650	-	650	630	672	Pen.	Scab.	Pen.	Scab.	414.0	destroyed	X	X	-
#9	R1D37V650	0.9u			672				Scab.	441.5	330.8	25.1	376	-
#10	R2D37V650	3.9d			667				Pen.	453.5	395.8	12.7	339	-
#11	R3D37V650	0			667				Pen.	467.0	424.0	9.2	334	-
#12	R1D37V700	0	700	669	713	Pen.	Scab.	Pen.	Perf.	441.5	311.0	29.6	500	45.12
#13	R2D37V700	1.4u			713				Scab.	454.0	331.0	27.1	382	-
#14	R3D37V700	1.4d			712				Scab	467.0	399.5	14.5	366	-
#15	R1D37V750	1.9u	750	722	767	Scab.	Perf.	Scab.	Perf.	439.5	139.0	68.4	500	X
#16	R2D37V750	0			772				Perf.	453.5	289.0	36.3	500	X
#17	R3D37V750	0			765				P.Limit	467.5	363.0	22.4	415	0

Table 4.2 Result of impact test for 12.7mm projectile

Designation		Yaw (°)	Striking Velocity(m/s)			Failure mode				Specimen mass(kg)			DOP (mm)	Residual Velocity (m/s)
			Target	Cal.	Measure	Empirical Formula			Test	Before	After	|B-A| /A, %		
						ACE	Conwep	NDRC						
#18	R0D12V850	0	850	827	851	Pen.	Pen.	Pen.	Pen.	418.5	417.5	0.2	118	-
#19	R1D12V850	9.6d			852				Pen.	436	435	0.2	120	-
#20	R2D12V850	0			852				Pen.	450	449	0.2	118	-
#21	R3D12V850	1.7d			851				Pen.	467.5	466.5		73	-

4.2. Damage assessment

4.2.1. Failure mode

This chapter presents the results of a collision experiment conducted to investigate the failure modes of test specimens with varying rebar ratios. The impact speed was gradually increased from 550 m/s to 850 m/s, with intervals of 50 m/s, and the exit and impact surfaces of the specimens were analyzed using images. The findings provide insights into the effect of rebar ratios on the failure modes of the specimens under high-speed impact loading.

At the lowest impact speed of 550 m/s, penetration was observed in all rebar ratios of the test specimens, but no scabbing was observed on the rear

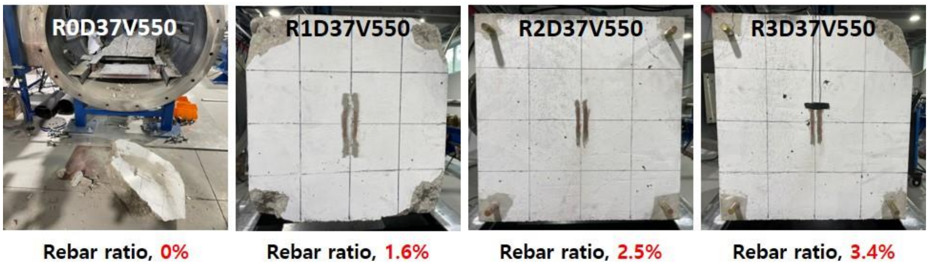

(a)

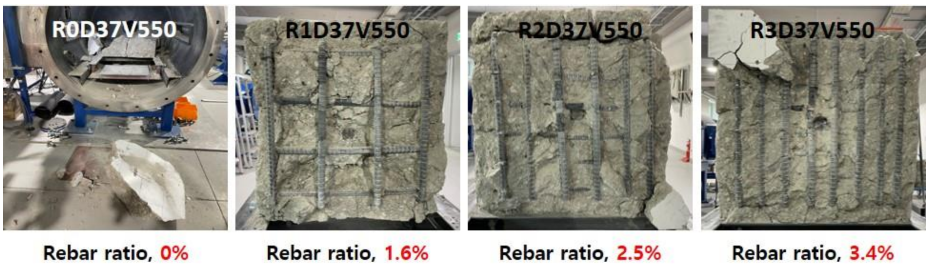

(b)

Figure 4.1 Failure mode (V=550m/s): (a) Exit surface; (b) Impact surface

surface, as shown in Figure 4.1. Since even plain concrete specimens exhibited total destruction at the lowest speed, collision tests for plain concrete specimens at higher speed ranges were omitted as it is expected that total destruction would also occur.

In addition, despite being the lowest speed, spalling occurred across the entire front surface of the test specimens, in contrast to the rear surface. This suggests the possibility that the spalling damage area may exceed the test specimen size of 600 mm.

At the impact velocity of 600 m/s, penetration was observed in all rebar ratios of the test specimens, but no scabbing was observed on the rear surface, as shown in Figure 4.2.

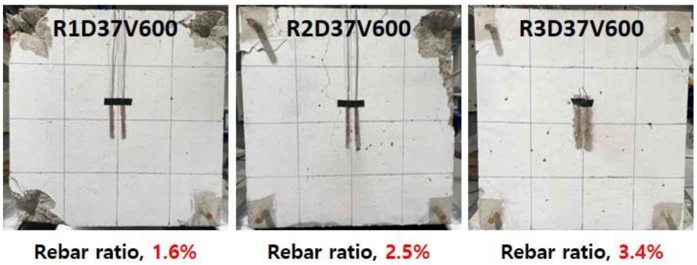

(a)

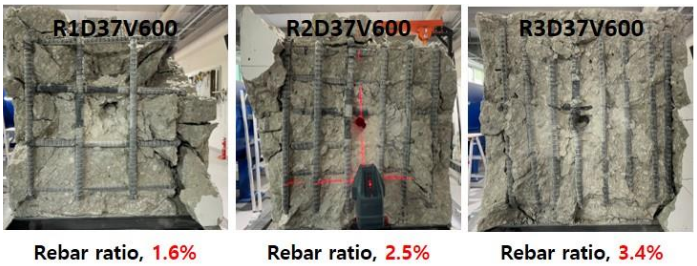

(b)

Figure 4.2 Failure mode (V=600m/s): (a) Exit surface; (b) Impact surface

In addition, spalling occurred across the entire front surface of the test specimens, in contrast to the rear surface, even at this collision speed.

At the impact velocity of 650 m/s, the failure mode of the test specimens differed depending on the rebar ratio for the first time as shown in Figure 4.3. Scabbing was observed at the rear of the specimen for rebar ratios of 1.6% or less, but penetration occurred for rebar ratios above 1.6%. This suggests that the impact resistance performance of RC targets varies depending on the rebar ratio.

At this impact velocity, spalling occurred over the entire front surface of the specimens, unlike the rear surface.

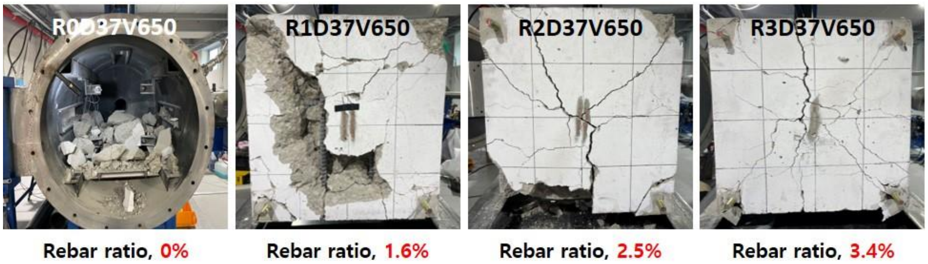

(a)

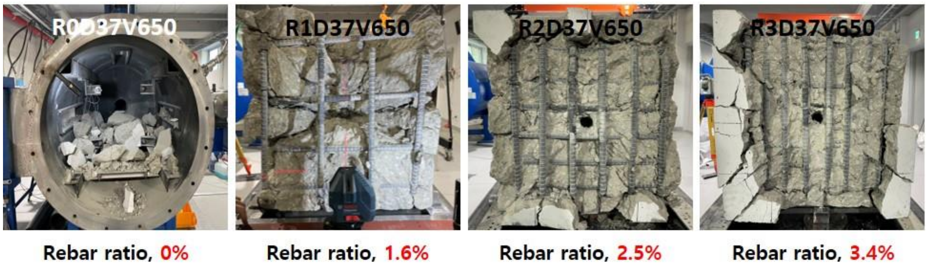

(b)

Figure 4.3 Failure mode (V=650m/s): (a) Exit surface; (b) Impact surface

At the impact velocity of 650 m/s, the test specimen's failure modes of penetration and scabbing were different depending on the rebar ratio. And at the impact velocity of 700 m/s, the failure modes of scabbing and perforation of the test specimen were different depending on the rebar ratio, as shown in Figure 4.4. At the Rebar ratio of 1.6% or less, perforation was observed at the rear of the test specimen, but at higher rebar ratios, the failure mode was scabbing. This suggests a difference in the impact resistance of RC targets depending on the rebar ratio.

Also, at this impact velocity, spalling occurred over the entire front of the test specimen, unlike the rear surface.

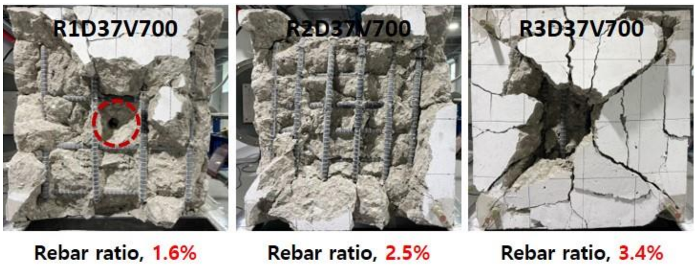

(a)

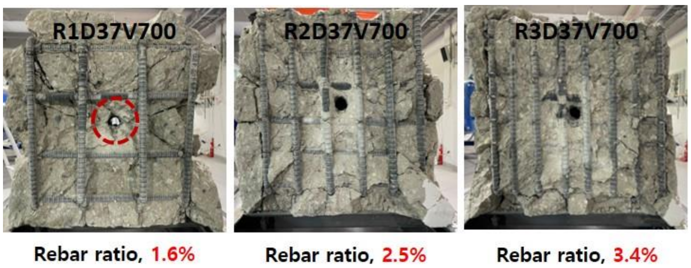

(b)

Figure 4.4 Failure mode (V=700m/s): (a) Exit surface; (b) Impact surface

At this impact velocity of 750m/s, the failure mode of the test specimen to the perforation-perforation limit differed depending on the rebar ratio. At a rebar ratio of 2.5% or less, perforation was observed at the rear of the test specimen, but at a rebar ratio of 3.4%, the failure mode was at the perforation limit. In Figure 4.5, the projectile penetrated the exit surface at a rebar ratio of 3.4%, but did not completely pass through the specimen, leaving the warhead exposed, so the failure mode at that impact velocity was classified as perforation limit. It was confirmed that the impact resistance of RC targets varies depending on the rebar ratio in this speed range.

(a)

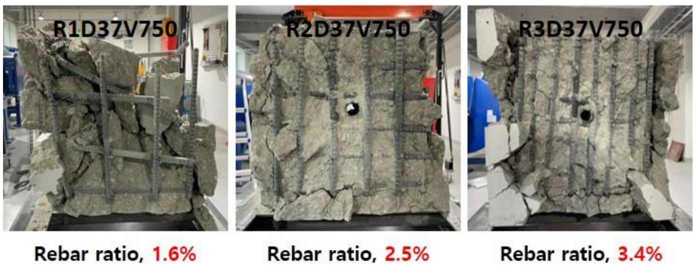

(b)

Figure 4.5 Failure mode (V=750m/s): (a) Exit surface; (b) Impact surface

The tests conducted at an impact velocity of 850 m/s were limited to 12.7 mm projectiles, in contrast to the previously tested 37 mm projectiles. As the mass and diameter of the projectile decreased, all failure modes were penetration, consistent with various empirical equations, and no scabbing was observed at the rear, as shown in Figure 4.6.

Additionally, unlike the results obtained with the 37 mm projectile, spalling was limited to a 300x300 mm² area in the front of the test specimen rather than occurring across the entire 600mm area. This suggests that the impact force needs to be reduced to detect a significant difference in the spalling area.

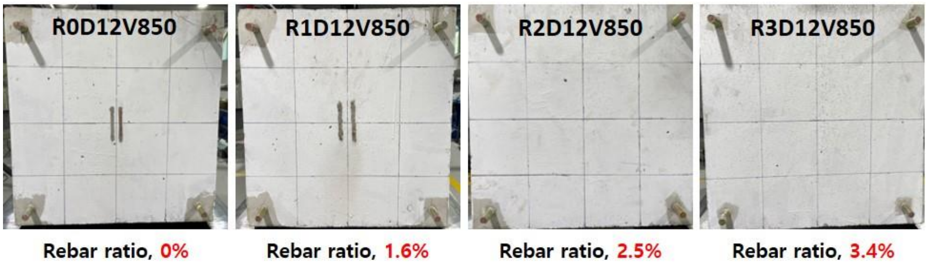

(a)

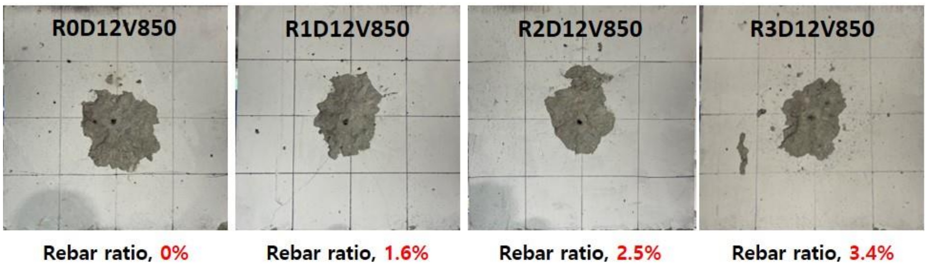

(b)

Figure 4.6 Failure mode (V=850m/s): (a) Exit surface; (b) Impact surface

Table 4.3 Result of failure mode

Striking Velocity(m/s)	Rebar ratio(%)			
	0	1.6	2.5	3.4
535	Penetration	Penetration	Penetration	Penetration
600	Penetration	Penetration	Penetration	Penetration
670	Scabbing	Scabbing	Penetration	Penetration
713	Perforation	Perforation	Scabbing	Scabbing
767	Perforation	Perforation	Perforation	Perforation limit

Table 4.3 presents a summary of the failure modes of the RC target during the 37mm projectile impact test across the entire velocity range. The 12.7mm projectile was not included in this table because there is insufficient data to observe the effect of increasing the rebar ratio on the penetration depth and failure area. It can be observed that in the high-speed range of 670-767m/s, the impact resistance of the specimen improves as the rebar ratio increases, leading to different failure modes under the same impact conditions.

In more detail, scabbing limit was observed at 600-670 m/s for a rebar ratio of 0-1.6%, and at 670-713 m/s for a rebar ratio of 2.5-3.4%. Similarly, perforation limit was found at 670-713 m/s for a rebar ratio of 0-1.6%, and at 713-767 m/s for a rebar ratio of 2.5-3.4%. Moreover, for a rebar ratio of 3.4%, the perforation limit was reached at 767 m/s.

4.2.2. Mass loss of specimen

The mass loss of the test specimen was measured before and after the collision test using electronic scales to determine the extent of mass loss during the impact, which could help evaluate the damage sustained by the test piece. The results obtained were plotted in Figure 4.7, which clearly shows that the overall mass loss of the specimen increased with increasing impact velocity.

Additionally, it was observed that the mass loss of the specimen decreased as the rebar ratio increased when tested under the same impact velocity. This suggested that as the amount of reinforcement in the RC target was increased, fragments due to spalling or scabbing decreased, which led to a decrease in the mass loss of the specimen.

These findings have important implications for the design and construction of RC structures subjected to high-velocity impacts, as they highlight the importance of selecting an appropriate rebar ratio to improve the impact resistance of the structure.

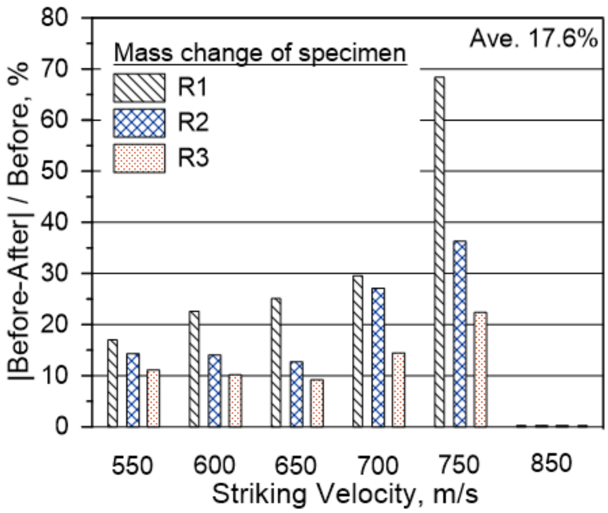

Figure 4.7 Mass loss of specimens after impact test

Table 4.4 Mass loss details of specimens after impact test

velocity, m/s	I.D.	mass of specimen, mm		|A-B|/A, %
		Before(A)	After(B)	
550	R1D37V550	441.5	366.5	17.0
	R2D37V550	454.5	389.5	14.3
	R3D37V550	472.5	420	11.1
600	R1D37V600	438	339	22.6
	R2D37V600	452	388.5	14.0
	R3D37V600	468	420.5	10.1
650	R1D37V650	441.5	330.8	25.1
	R2D37V650	453.5	395.8	12.7
	R3D37V650	467	424	9.2
700	R1D37V700	441.5	311	29.6
	R2D37V700	454	331	27.1
	R3D37V700	467	399.5	14.5
750	R1D37V750	439.5	139	68.4
	R2D37V750	453.5	289	36.3
	R3D37V750	467.5	363	22.4
850	R0D12V850	418.5	417.5	0.2
	R1D12V850	436	435	0.2
	R2D12V850	450	449	0.2
	R3D12V850	467.5	466.5	0.2
Average				17.6

4.2.3. Mass and length loss of projectile

This chapter investigates the mass and length change of projectiles under high-velocity impact and its correlation with impact velocity and rebar ratio.

Figure 4.8 showed that the mass loss of the projectiles slightly increased from 1.7% to 3.0% as the impact velocity increased. Furthermore, it was observed that the mass loss of small-caliber projectiles was relatively large compared to larger-caliber ones. In addition to the mass change, the length change of the projectiles was also analyzed as shown in Figure 4.9. It was observed that the length loss slightly increased from 3.2% to 8.8% as the impact velocity increased. Furthermore, the small-caliber projectiles experienced relatively large length losses.

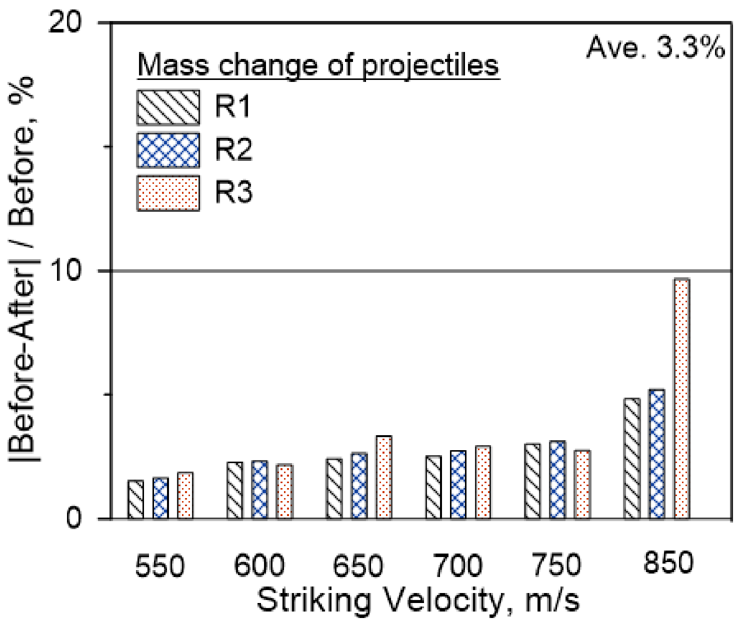

Figure 4.8 Mass loss of projectiles after impact test

Table 4.5 Mass loss details of projectiles after impact test

velocity, m/s	I.D.	mass of specimen, mm		|A-B|/A, %
		Before(A)	After(B)	
550	R1D37V550	839.54	826.69	1.5
	R2D37V550	839.31	825.48	1.6
	R3D37V550	839.18	823.58	1.9
600	R1D37V600	839.4	820.34	2.3
	R2D37V600	839.33	819.81	2.3
	R3D37V600	839.44	821.16	2.2
650	R1D37V650	839.73	819.39	2.4
	R2D37V650	839.55	817.4	2.6
	R3D37V650	839.06	811.1	3.3
700	R1D37V700	839.29	818.15	2.5
	R2D37V700	839.44	816.45	2.7
	R3D37V700	839.28	814.78	2.9
750	R1D37V750	838.83	813.59	3.0
	R2D37V750	839.22	813.03	3.1
	R3D37V750	839.52	816.47	2.7
850	R0D12V850	26.9	25.4	5.6
	R1D12V850	26.9	25.6	4.8
	R2D12V850	26.9	25.5	5.2
	R3D12V850	26.9	24.3	9.7
Average				3.3

However, the projectiles' overall mass and length loss were very small, and the effect of rebar ratio on mass and length loss needed to be clarified.

The increase in mass and length loss with increasing impact velocity can be attributed to the increased energy transferred to the projectiles during the impact. The relatively large loss observed in small-caliber projectiles can be attributed to their lower resistance to deformation and fragmentation than larger-caliber ones. The unclear effect of rebar ratio on mass and length loss may be because the effect of reinforcement on loss is negligible compared to other factors, such as projectile size and impact velocity.

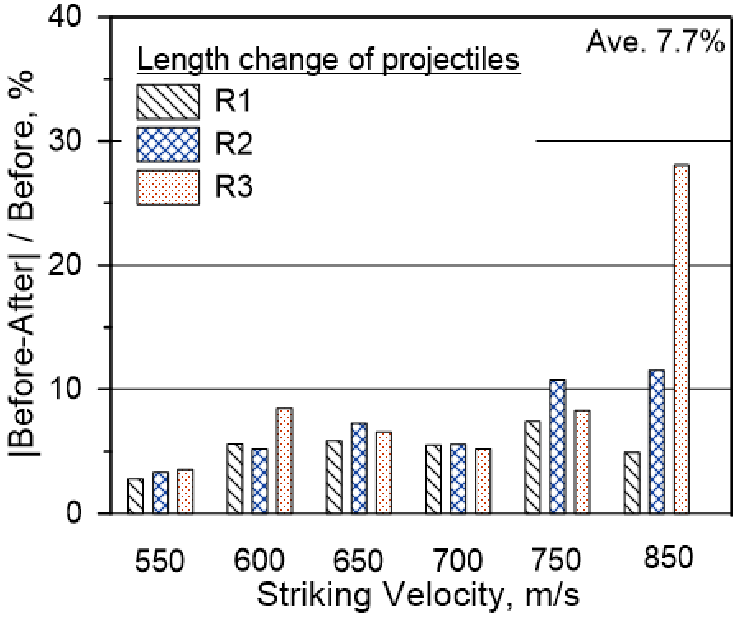

Figure 4.9 Mass loss of specimens after impact test

In summary, the results indicate that projectiles' mass and length loss slightly increases with increasing impact velocity and that small-caliber projectiles exhibit relatively large mass loss. However, the overall loss of projectiles was very small, and the effect of rebar ratio on mass loss needed to be clarified.

Therefore, the deformation and loss of the projectile before and after the impact was considered negligible, and it could be categorized as a hard type of projectile.

Table 4.6 Length loss details of projectiles after impact test

velocity, m/s	I.D.	mass of specimen, mm		|A-B|/A, %
		Before(A)	After(B)	
550	R1D37V550	123	119.57	2.8
	R2D37V550	123	118.93	3.3
	R3D37V550	123	118.66	3.5
600	R1D37V600	123	116.12	5.6
	R2D37V600	123	116.6	5.2
	R3D37V600	123	112.55	8.5
650	R1D37V650	123	115.81	5.8
	R2D37V650	123	114.06	7.3
	R3D37V650	123	114.91	6.6
700	R1D37V700	123	116.24	5.5
	R2D37V700	123	116.14	5.6
	R3D37V700	123	116.58	5.2
750	R1D37V750	123	113.88	7.4
	R2D37V750	123	109.74	10.8
	R3D37V750	123	112.81	8.3
850	R0D12V850	43.4	39.06	10.0
	R1D12V850	43.4	41.27	4.9
	R2D12V850	43.4	38.39	11.5
	R3D12V850	43.4	31.22	28.1
Average				7.7

4.3. Assessment of penetration depth

Before measuring the penetration depth, the yawing of the projectile upon collision with the target was checked. The largest penetration depth occurred when the projectile collided perpendicular to the target surface, and a penetration depth decreased as yawing increased. For the 37mm projectile, as shown in Figure 4.10 and Table 4.7, the collision angle of the projectile was maintained at an average of 1.6 degrees, indicating good straightness of the projectile in most of the 17 tests (#1-#17) conducted. As the collision velocity decreased, a tendency for the collision angle to increase was observed for the 37mm projectile.

For the 12.7mm projectile, the collision angle of the projectile was at an average of 2.8 degrees in the 4 tests (#18-#21) conducted, and the deviation in collision angle was greater than that of the 37mm projectile. This is presumed to be due to the weight of the projectile, which is approximately 3% lighter than that of the 37mm projectile, resulting in a relatively more significant influence of sabot separation. In summary, both types of projectiles had a small amount of yawing, ranging from 1.6 to 2.8 degrees, and the problem of straightness was considered to be negligible.

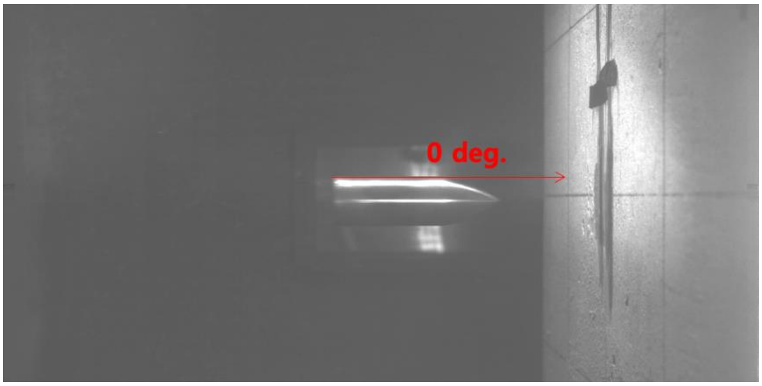

(a)

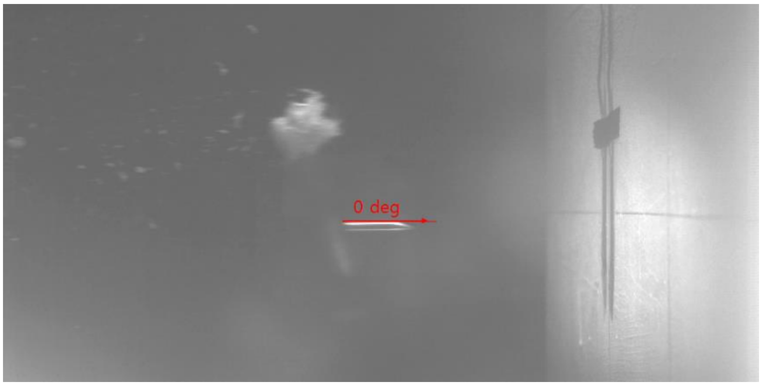

(b)

Figure 4.10 Yawing check of the projectile: (a) 37mm; (b) 12.7mm

Table 4.7 Yawing of the projectile

	Designation	Yaw(°)	Direction
#1	R0D37V550	1.3	upward
#2	R1D37V550	6.4	downward
#3	R2D37V550	5.1	upward
#4	R3D37V550	0.9	downward
#5	R1D37V600	1.6	upward
#6	R2D37V600	1.4	upward
#7	R3D37V600	0	-
#8	R0D37V650	-	-
#9	R1D37V650	0.9	upward
#10	R2D37V650	3.9	downward
#11	R3D37V650	0	-
#12	R1D37V700	0	-
#13	R2D37V700	1.4	upward
#14	R3D37V700	1.4	downward
#15	R1D37V750	1.9	upward
#16	R2D37V750	0	-
#17	R3D37V750	0	-
#18	R0D12V850	0	-
#19	R1D12V850	9.6	downward
#20	R2D12V850	0	-
#21	R3D12V850	1.7	upward

In this study, the penetration depth of the 37mm projectile was measured in 12 out of 17 experiments, excluding the cases of complete destruction and penetration. The measured data were then compared with the four main local damage prediction equations (ACE, UKAEA, Conwep, and NDRC) recommended by military standards and guidelines for military facilities in Table 2.1. The prediction accuracy was evaluated and presented in Figures 4.11-4.12.

The results indicate that the Conwep formula had the highest predictive accuracy for the depth of penetration among the equations. It was observed that Conwep could predict the penetration depth of the 37mm projectile with an accuracy of approximately 95%, which was higher than the accuracy of the other equations.

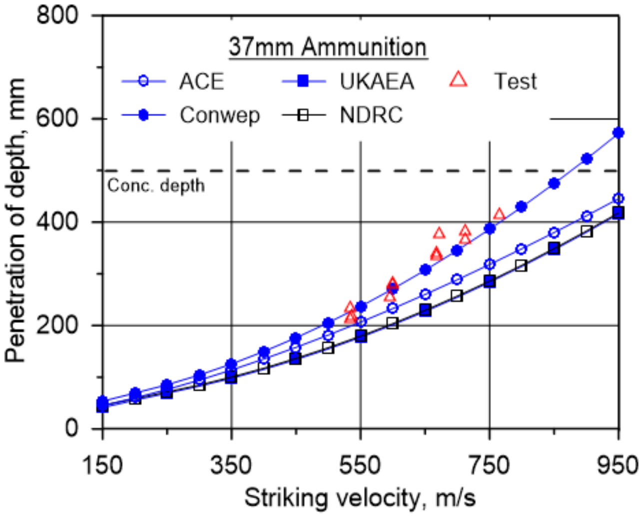

Figure 4.11 Comparison of penetration depth with empirical formulae: 37mm

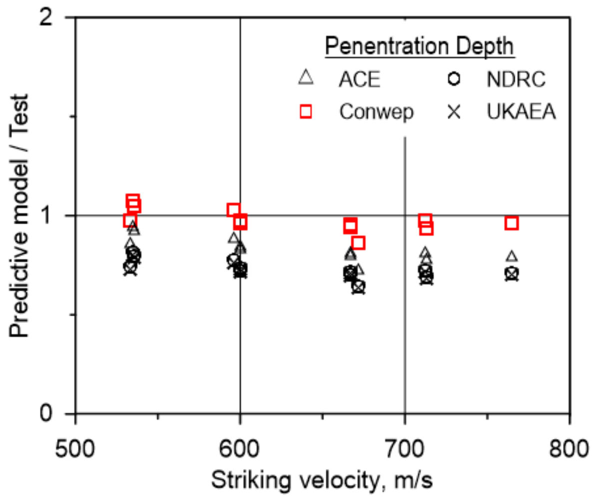

Figure 4.12 Predictive accuracy of penetration depth with empirical formulae: 37mm projectile

These findings suggest that Conwep is a suitable and reliable method for predicting the depth of penetration of projectiles for military facilities. However, it should be noted that the accuracy of the prediction equations may be affected by various factors, such as the type of target material, impact velocity, and the angle of incidence. Therefore, further studies are needed to validate the accuracy of these equations under various conditions and for different types of projectiles.

4.4. Assessment of scabbing & perforation limit

This chapter compares the accuracy of thresholds for scabbing and perforation against experimental results using the main existing local damage equations. Specifically, it uses prediction equations recommended by military facilities standards, such as DOE-STD-3014-2006, ACI 349-13, and NEI 07-13 for nuclear power plant structures, and compares their performance as shown in Table 2.2.

According to the rebar ratio, there is a difference in the scabbing limit values, with the scabbing limit occurring within the velocity range of 575 m/s to 630 m/s for specimens with a rebar ratio of 1.6 or lower and within the velocity range of 630 m/s to 670 m/s for specimens with a rebar ratio of 2.5 or higher.

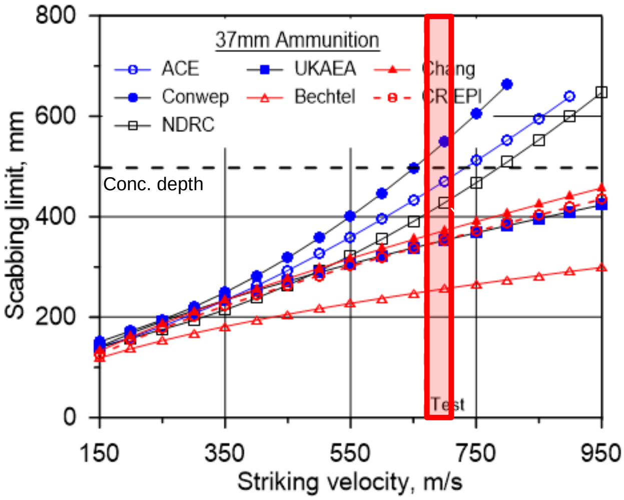

Figure 4.13 Comparison of scabbing limit with empirical formulae

Among various design criteria's local damage prediction equations, the Conwep equation provides the most accurate empirical prediction for the test. In contrast, the other equations predicted that penetration would occur when a projectile of that velocity impacts a 500 mm wall thickness, which does not align with the experimental results.

There are differences in the perforation limit values depending on the rebar ratio, similar to the scabbing limit. For specimens with a rebar ratio of 1.6 or lower, the perforation limit occurs within the velocity range of 670 m/s to 713 m/s. In contrast, for specimens with a rebar ratio of 1.6 to 2.5, the perforation limit occurs within the velocity range of 713 m/s to 770 m/s. For specimens with a rebar ratio of 3.4, the perforation limit occurs at a velocity of 765 m/s. Figure 4.14 shows the occurrence of perforation within the velocity range of 713 m/s to 767 m/s.

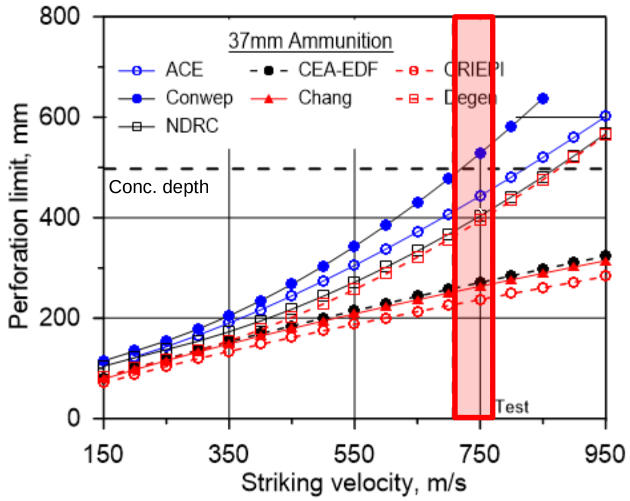

Figure 4.14 Comparison of perforation limit with empirical formulae

The Conwep equation is the most accurate empirical prediction among the local damage prediction equations recommended by various design criteria, similar to the scabbing limit. On the other hand, the other equations predict that penetration or scabbing will occur when a projectile with that velocity impacts a 500 mm wall thickness, which is inconsistent with the experimental results.

4.5. Effect of reinforcement on impact resistance

In this chapter, the impact resistance of structures was examined with a focus on how the rebar ratio affects this property. The first aspect discussed was the depth of penetration (DOP), explored through experimental results presented in Table 4.5. These results reveal that the DOP decreases as the rebar ratio increases for a given impact velocity.

Furthermore, Figure 4.15 compares the experimental results and the primary predictive equations in terms of rebar ratio, highlighting the accuracy of these predictive models. Overall, this chapter provides insights into how rebar ratios can impact the structural integrity of materials in the face of impacts.

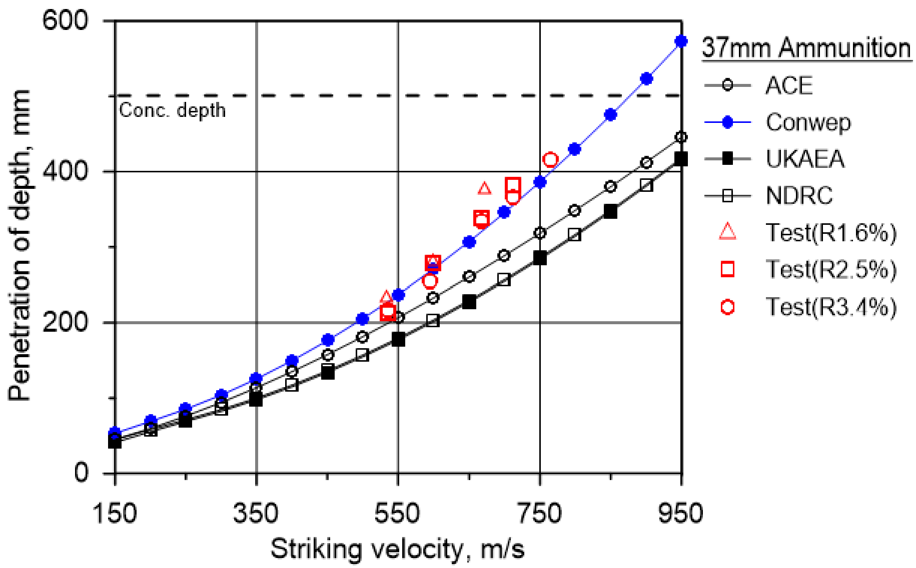

Figure 4.15 Comparison of DOP with effect of rebar ratio

As shown in the graph and table, the penetration depth decreased somewhat as the rebar ratio increased for the same impact velocity for the penetration depth. In addition, the decrease in penetration depth when the rebar ratio increased from 1.6% to 2.5% was 6.6% on average, but the decrease when the rebar ratio increased to 3.4% was only 2.6% on average, so the difference was relatively small. In other words, in general, the penetration depth decreased with the increase in rebar ratio. However, at a certain level of rebar ratio, the effect on the penetration depth decreased somewhat.

Table 4.8 Comparison of penetration depth

Designation		Striking Velocity(m/s)	Failure mode	DOP (mm)	DOP reduction (%)
#1	R0D37V550	535	Pen.	-	-
#2	R1D37V550		Pen.	232	0
#3	R2D37V550		Pen.	212	8.6
#4	R1D37V550		Pen.	217	6.5
#5	R1D37V600	600	Pen.	281	0
#6	R2D37V600		Pen.	277	1.4
#7	R3D37V600		Pen.	261	7.1
#8	R0D37V650	670	Scab.	-	-
#9	R1D37V650		Scab.	376	0
#10	R2D37V650		Pen.	339	9.8
#11	R3D37V650		Pen.	334	11.2
#12	R1D37V700	713	Perf.	-	-
#13	R2D37V700		Scab.	382	0
#14	R3D37V700		Scab	365	4.5
#15	R1D37V750	767	Perf.	-	-
#16	R2D37V750		Perf.	-	-
#17	R3D37V750		P.Limit	415	0

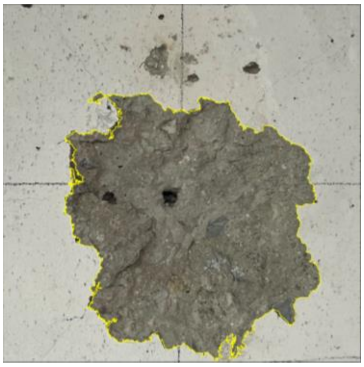

R0(#18): 34,851 mm^2

R1(#19): 28,633 mm^2

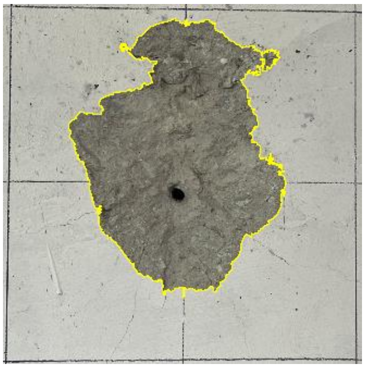

R2(#20): 22,383 mm^2

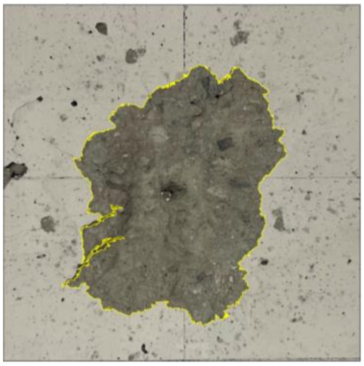

R3(#21): 26,835 mm^2

Figure 4.16 Spalling area of impact surface at 12.7mm projectile

Figure 4.16 shows the spalling area at the front of the specimen due to the impact of a 12.7 mm projectile. The 12.7 mm projectile was only tested for a single impact velocity of 850 m/s to examine the effect of rebar ratio on projectile size. As shown in Figure 4.17, no significant difference in the size of the frontal spalling area with increasing rebar ratio was found for this projectile.

This is different from the impact test of the 37mm projectile, and it is presumed that the relative size of the test object and the projectile has some influence on the impact resistance performance according to the rebar ratio. However, at a certain level of rebar ratio, the effect on the penetration depth decreased somewhat.

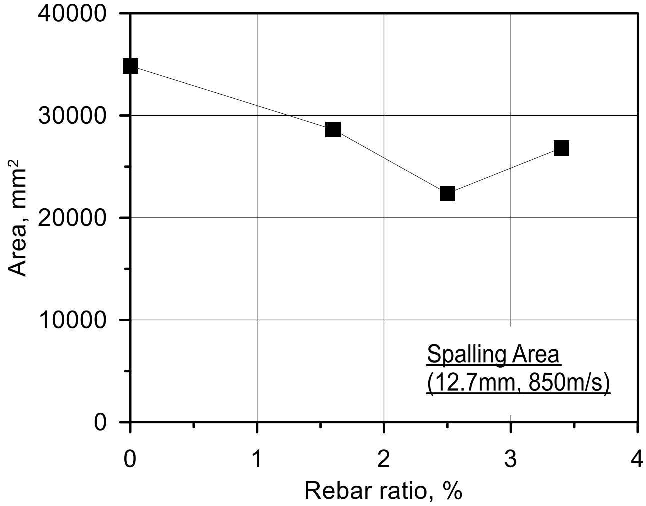

Figure 4.17 Spalling area of impact surface at 12.7mm projectile(850m/s)

4.6. Modification of empirical formula

4.6.1. Suggestion of modified impact formula

For the empirical formula modification, test data was initially gathered to assess the prediction accuracy of the current empirical formula. A modification was then proposed, incorporating a term considering the effect of reinforcement. This modification was based on the empirical formula that demonstrated the highest accuracy per the regression analysis with test data.

Subsequently, the proposed equation was re-evaluated using the collected experimental data and the results of this experiment. This process aimed to refine and optimize the empirical formula's predictive accuracy, particularly concerning reinforcement.

As shown in Chapters 4.3 and 4.4, comparing the test results of this study with the empirical formulas recommended by the military facility design standards showed that the Conwep equation had the highest prediction accuracy, so it was adopted as the basic structure. As introduced in Chapter 2, the expressions defining the penetration depth, scabbing limit, and perforation limit according to the Conwep formula are shown in Equations 4.1 to 4.5.

$$G = 4.7 \times 10^{-5} \frac{N^* M}{d\sqrt{f_c}} \left(\frac{V_0}{d} \right)^{1.8} \tag{4.1}$$

$$N^* = 0.72 + 0.25(CRH - 0.25)^{0.5}$$

$$\frac{h_{pen}}{d} = 2G^{0.5} \quad (G \le 1) \tag{4.2a}$$

$$\frac{h_{pen}}{d} = G + 1 \quad (G > 1) \tag{4.3b}$$

$$\begin{aligned} \frac{h_{scab}}{d} &= 7.91\left(\frac{h_{pen}}{d}\right) - 5.06\left(\frac{h_{pen}}{d}\right)^2 \quad \text{for } \frac{h_{pen}}{d} \le 0.65 \\ \frac{h_{scab}}{d} &= 2.12 + 1.36\left(\frac{h_{pen}}{d}\right) \quad \text{for } 0.65 < \frac{h_{pen}}{d} \le 11.75 \end{aligned} \tag{4.4}$$

$$\begin{aligned} \frac{h_{per}}{d} &= 3.19\left(\frac{h_{pen}}{d}\right) - 0.718\left(\frac{h_{pen}}{d}\right)^2 \quad \text{for } \frac{h_{pen}}{d} \le 1.35 \\ \frac{h_{per}}{d} &= 1.32 + 1.24\left(\frac{h_{pen}}{d}\right) \quad \text{for } 1.35 < \frac{h_{pen}}{d} \le 13.5 \end{aligned} \tag{4.5}$$

The values for the scabbing limit and perforation limit in Equations 4.4 and 4.5 are dependent on the penetration depth detailed in Equation 4.1. Therefore, the modifications to the empirical equations initially targeted the penetration depth. Given that the ConWep equation does not account for a rebar variable, other empirical equations incorporating a value for rebar were scrutinized. Suitable candidates were found in the CEA-EDF and UKAEA equations, listed in Table 4.9. These equations are widely accepted and used for predicting the limit velocity of penetration in the design criteria for nuclear power plant structures. A term for $\gamma + 0.3$, used in both equations, was combined with the ConWep equation to create the form of the modified equation, where γ is the percentage of reinforcement described by the percentage each way in each face (% , EWEF)

Table 4.9 Empirical formulas with consideration of reinforcement

Empirical formulas	Perforation limit velocity
CEA-EDF (1991)	$V_p = 1.3\rho_c^{1/6} f_c^{1/2} \left(\frac{pH^2}{\pi M}\right) (\gamma + 0.3)^{1/2}$
UKAEA (1991)	$V_p = \begin{cases} V_a \; for \; V_p \geq 70 \; m/s \\ V_a \left[1 + \left(\frac{V_a}{500}\right)^2\right] \; for \; V_p < 70 \; m/s \end{cases}$ Where, $V_a = 1.3\rho_c^{1/6} f_c^{1/2} \left(\frac{pH^2}{\pi M}\right) (\gamma + 0.3)^{1/2} \left[1.2 - 0.6\left(\frac{c_r}{H}\right)\right]$

Informed by the test results, an adapted ConWep model has been proposed. This modified model incorporates a term for rebar ratio, and its structure has been derived via regression analysis, as depicted in Equation 4.6.

$$\frac{h_{pen}}{d} = 2G^{0.5} \quad (G \leq 1), \quad \frac{h_{pen}}{d} = G + 1 \quad (G > 1)$$
$$\text{where} \quad G = 4.8 \times 10^{-5} \frac{N * M}{d\sqrt{f_c}} \left(\frac{V_0}{d}\right)^{1.8} \left(\frac{1}{\gamma + 0.3}\right)^{0.16} \tag{4.6}$$

The results of predicting the penetration depth according to the impact velocity using the modified empirical model and comparing it with the experimental results are shown in Figure 4.18.

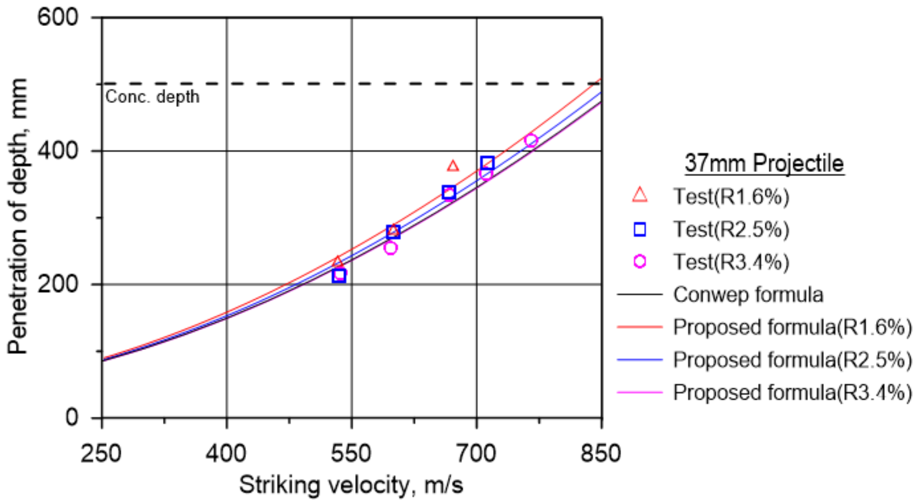

Figure 4.18 Comparison between test results and proposed formula

The modified model, which considers the rebar ratio's effect, exhibits improved compliance with the test data compared to the extant ConWep model.

4.6.2. Verification of developed impact formula

To verify the validity of the proposed model, it is necessary to validate the model through the collected research data. Table 4.10 includes a total of 187 test data collected from various experiments. Data with impact velocities of 100 m/s or less were filtered out, aiming to concentrate on the highest velocity range, mainly involving hard-type rigid projectiles and RC test objects. It was found during the data collection process that publicly available experimental data for RC structures at high impact speeds above 500 m/s was quite limited.

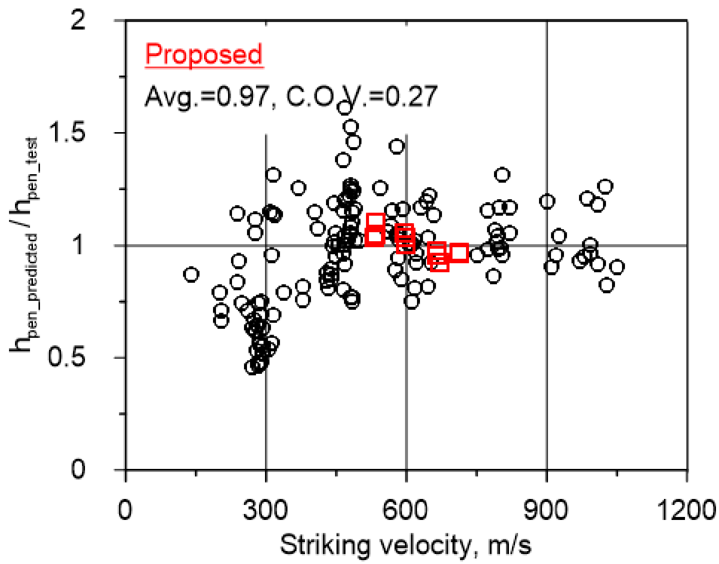

Figure 4.19 Comparison between collected data and proposed formula

Table 4.10 Collected test data for DOP comparison

Tests	Data (ea)	Projectile						Concrete Target		
		Shape	Mass (kg)	Diameter (mm)	Velocity (m/s)	CRH (R/D)	L/D	C. Strength (MPa)	Depth (m)	Type
	187	**Ogive,**	**0.064-485**	**12.9-76**	**132-1050**	**1.69-6**	**3-15**	**21.6-152**	**0.76-2.44**	**Plain,RC**
Magnusson(2001)	45	Ogive	6.28, 44.76	75	484-653	1.69, 3	3	35-152	0.8-2	Plain, RC, fiber
Gran-Frew(1997)	3	Ogive	2.3	51	316-320	3	7	43	1.22	Plain
Forrestal et al.(2003)	15	Ogive	12.9-13.2	76	139-456	3, 6	7	23, 39	1.22-1.83	Plain
Frew et al.(1998)	14	Ogive	0.478-1.62	20.3, 30.5	442-1009	3	8.5	58.4	0.94-2.28	Plain
Forrestal et al.(1994)	17	Ogive	0.9-0.912	26.9	277-800	2	9	32.4-108	0.76-1.83	Plain
Forrestal et. al.(1996)	24	Ogive	0.064-1.61	12.9, 30.5	450-1050	3-4.25	6.89-10	21.6-62.8	0.76-2.44	Plain
Abdel-Kader ea.al.(2014)	8	Blunt	0.175	23	201-354	0.5	3	26	100	RC
Xueyan Zhang et.al.(2020)	5	Ogive	5	64	430-439	3	4.5	30-36	800	RC
Dancygier et.al.(2007)	39	Ogive	1.5	49	203-314	1.5	4	40-117	200	RC
Current Study(2022)	**17**	**Ogive**	**0.84**	**37**	**550-750**	**3**	**3.3**	**52.5**	**0.5**	**RC**

After the collected data where perforation occurred, and the depth of penetration could not be determined were filtered out, the predictive accuracy of the proposed equation was evaluated. The remaining 153 data points were used for this purpose. The equation demonstrated an impressive average predictive accuracy of 0.97, with a coefficient of variation of 0.27, as shown in Figure 4.19. This provides evidence that the proposed equation, which considers the reinforcement effect, exhibits a high degree of accuracy in this study and in other experimental environments.

Table 4.11 and Figure 4.20 show the results of our review of the predictive accuracy of the experimental data collected for the primary empirical expressions introduced in Chapter 2.3. It can be seen that the BRL(1941), Conwep(1992), UMIST(R2001), and Petry(1910) equations have reasonable predictive accuracy with an average of 0.91, 0.83, 0.83, and 0.89, respectively. Still, they are lower than the 0.97 predictive accuracy of the proposed formula in this study.

Table 4.11 Predictive accuracy results by researcher

Tests	Data (ea)	$h_{pen\_predicted}$ / h_{pen_test}									
		BRL	ACE	NDRC	UKAEA	H & H	Hughes	Conwep	Petry	UMIST	**Proposed**
Magnusson (2001)	36	0.98	0.83	0.75	0.74	0.49	0.58	0.94	0.82	0.93	1.08
Gran-Frew (1997)	3	1.22	0.97	0.89	0.87	0.83	0.97	1.02	1.37	0.8	1.2
Forrestal et al. (2003)	15	1.05	0.77	0.64	0.63	0.58	0.71	0.78	1.73	0.63	0.79
Frew et al. (1998)	14	0.86	0.67	0.65	0.65	0.56	0.62	0.79	1.49	0.66	0.98
Forrestal et al. (1994)	17	1.09	0.83	0.67	0.67	0.59	0.72	0.86	2.05	0.72	1.05
Forrestal et. al. (1996)	24	0.94	0.73	0.71	0.71	0.84	0.85	0.88	1.47	0.76	1.07
Xueyan Zhang et.al. (2020)	5	0.94	0.73	0.65	0.64	0.61	0.75	0.77	0.88	0.78	0.85
Dancygier et.al. (2007)	27	0.51	0.49	0.54	0.51	0.38	0.45	0.56	0.62	0.74	0.61
Current Study (2022)	12	1.03	0.83	0.73	0.72	0.61	0.96	0.97	0.92	0.65	1.01
Average	153	0.91	0.74	0.69	0.68	0.52	0.67	0.83	0.89	0.83	0.97
COV		0.29	0.26	0.24	0.24	0.27	0.3	0.26	0.41	0.26	0.27

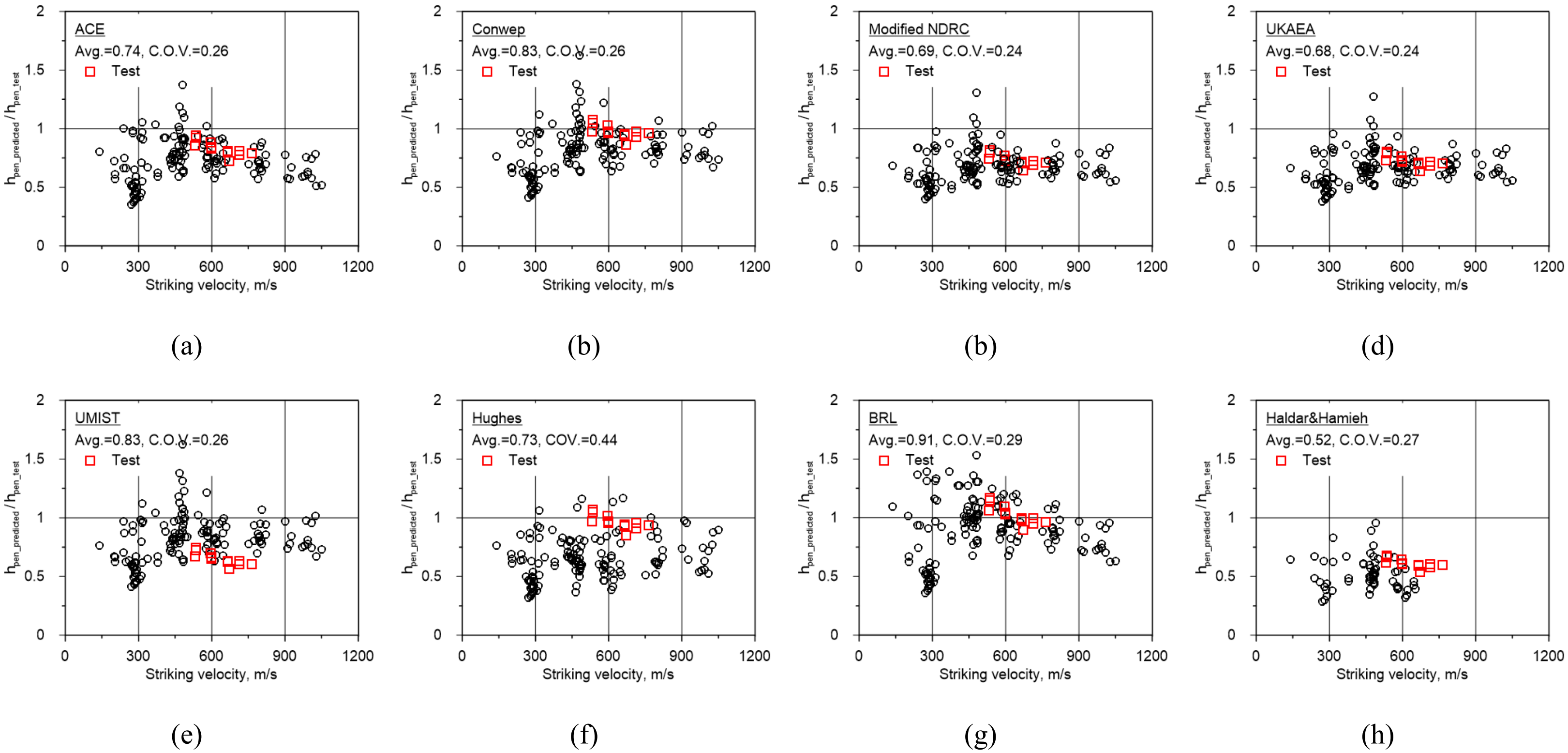

Figure 4.20 Predictive accuracy results with various empirical formulae

4.7. Concluding remarks

In this chapter, the experimental program's results are analyzed for damage assessment, penetration depth, scabbing & perforation limit, and the effect of rebar on the impact resistance performance. Based on the results, a modified empirical equation that considers the effect of rebar is proposed, and the prediction accuracy of the modified empirical equation proposed in this study is verified for 153 experimental data.

The outcomes of the experimental program were analyzed, focusing on damage assessment, penetration depth, scabbing & perforation limits, and the influence of rebar. The experiments evidenced that distinct failure modes were influenced by the rebar ratio and that the impact resistance of RC targets was improved as the rebar ratio increased. Furthermore, the rebar ratio was observed to substantially affect scabbing and perforation limits.

In the experiments, it was noted that an increase in the rebar ratio lessened the mass loss of the specimen, even though the reduction in the mass and length of the projectile was found to be insufficient.

The prediction accuracy of existing formulae in a high-velocity range was assessed. Among the empirical formulas recommended by existing military facility standards, Conwep's model demonstrated prediction accuracy most akin to the tests for Depth of Penetration (DOP) and scabbing & perforation limits. However, low prediction accuracy in the 550m/s-750m/s velocity range was shown by the empirical formulae suggested by Nuclear Power Plant (NPP) design criteria. Of course, the empirical equations recommended in the NPP design criteria assume an aircraft collision situation, and the application range is the collision speed range of 300m/s or less, so caution should be exercised in utilizing the empirical equations recommended in the NPP design criteria for the military aircraft collision situation in this study.

Based on these findings, a modified empirical equation incorporating the rebar's effect was proposed. The prediction accuracy of the proposed formula was validated using a total of 153 experimental data points, and it exhibited superior performance compared to other recommended empirical formulas.

It is important to note that although an increase in the rebar ratio generally resulted in improved impact resistance of RC targets, this was not significantly manifested in the case of a 12.7mm projectile, where the penetration depth and failure area due to reinforcement were not substantial. This shows the possibility that the impact of rebar ratio on the impact resistance performance may decrease when the relative size of the test specimen and projectile decreases below a certain level.

Ultimately, the importance of considering the rebar ratio in predicting and enhancing the impact resistance of structures is emphasized by this study. The superiority of the proposed formula in achieving high predictive accuracy is also validated, providing a foundation for further research and potential practical applications.

5. Analytical Study

5.1. Introduction

Finite element analysis (FEA) has become an essential tool for engineers and researchers to analyze and optimize the behavior of complex structures under different loading conditions. One of the most challenging types of structural analysis is the simulation of collision and explosion problems, which involves complex dynamic behavior and requires advanced modeling techniques.

LS-DYNA is a commercial FEA software. It is known for its specialization in deformation problems, particularly for impact and explosion analysis. The software is widely used in the automotive, aerospace, and defense industries and has been applied to various problems, from car crash simulations to blast analysis. LS-DYNA can accurately model a wide range of materials, from metals to composites, and can simulate the behavior of structures under dynamic loads with high accuracy.

This study utilized LS-DYNA to model the impact resistance of reinforced concrete (RC) structures subjected to high-velocity impacts. The RC structures were modeled using a combination of solid elements for concrete and beam elements for reinforcement. The effect was simulated using an explicit dynamic analysis, and the results were compared to experimental data to validate the analysis's accuracy.

5.2. Description of impact test for RC target

To verify the effect of the rebar and the modified empirical formula suggested in Chapter 4, the numerical analysis of the impact test was conducted in this section. The FEA model was established using LS-DYNA.

5.2.1. Modeling details

Figure 5.1 presents the components and boundary conditions used in the finite element analysis (FEA) model. The model incorporated the projectile, the RC beam, and the upper and lower supports. The projectile was modeled using 1–3mm solid elements, and the concrete of RC beams was modeled using 10 mm solid elements. For the upper and bottom supports, 5mm solid elements were used. All solid elements were eight-node solid elements with poor aspect ratios featuring full integration (ELFORM=-1) that no hourglass stabilization needed. In addition, the reinforcing bars were depicted using Hughes-Liu beam elements of 5mm (ELFORM=1), and a perfect bond was assumed between the concrete and reinforcing bars using the Constrained Beam in the Solid option. The boundary condition was input to the nodes on the support plane. Both the upper and lower boundary planes of the supports had their nodes constrained in all directions.

The projectile's initial velocity was input to the FEA model considering the impact velocity in the tests. As for the contact conditions, the Automatic Surface to Surface option was utilized among the RC beam, projectile, and support parts, with a friction coefficient set at 0.2. The FEA was terminated at about 2500 msec after the collision of the projectile with the RC target.

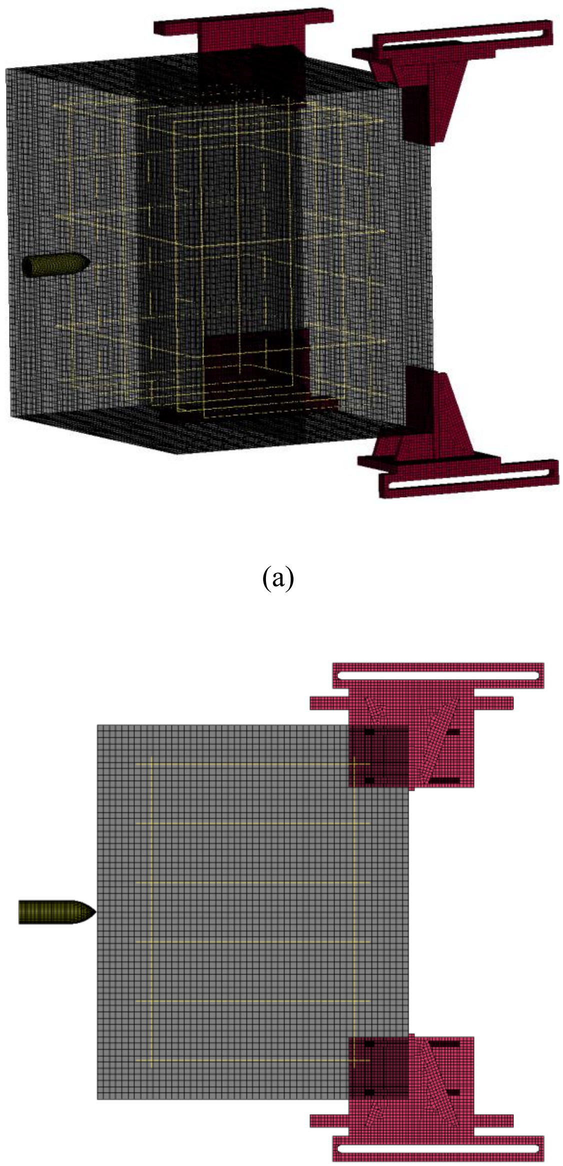

(a)

(b)

Figure 5.1 Modeling parts and boundary conditions

5.2.2. Material model for concrete

The KCC model, specifically the MAT 72R3, is extensively utilized in finite element analysis (FEA) for concrete structures subjected to impact and blast loads. This model effectively captures various characteristics of concrete behavior, including its dependency on pressure, lode angle, and strain rate. An additional advantage of the KCC model is that it allows incorporation of a user-defined curve for the DIF (Damage Initiation and Failure) model. By utilizing the DIF model, the KCC model enhances the representation of failure surfaces and retards damage accumulation. Therefore, for this study, the KCC model was chosen as the appropriate constitutive model for concrete.

The compressive strength of the specimen was determined to be 52.5 MPa based on material test results. The density and Poisson's ratio were set to 2350 kg/m3 and 0.18, respectively. The static properties in Table 3.7 were used to determine the material model parameters. The tensile strength was determined using Equation (5.1).

$$f_t = 0.3\left(f_c - \Delta f \right)^{2/3} \tag{5.1}$$

where $\Delta f = 8$ MPa .

The tensile strength (f_t) was calculated using the uniaxial tensile strength formula in the fib MC2010 (fib bulletin 65, 2012).

Kong et al. (2017) stated that the default $\eta - \lambda$ relationship led to overestimating concrete stiffness during the hardening phase and underestimating residual strength during the softening phase. Thus, the $\eta - \lambda$ relationship proposed by Markovich et al. (2011) was used in the FEA. This relationship, represented by Markovich et al.'s (2011) yield scale coefficient (η), has a characteristic of appropriately increasing during the hardening phase and decreasing during the softening phase, compared to the default values.

The model parameters and equation of state (EOS) were chosen using recommended or auto-generated values, following the methodology of Wu and Crawford (2015). The default EOS model was scaled down to align the initial bulk modulus with the bulk modulus derived from the material test. The input model parameters are presented in Tables 5.1 and 5.2. The tabulated compaction model (EOS 8) was utilized for the EOS model, and the EOS parameters can be found in Table 5.3, where ε_v and K_u denote the volumetric strain and unloading bulk modulus, respectively.

Compressive DIF models of ACI 349-13(γ_{ACI349}),ACI 370R-14($\gamma_{ACI370R}$), fib MC2010 (γ_{fib}), UFC 3-340-02 were considered in the FEA. Eq. (5.2-5.4) indicates the DIF model of the design codes and guidelines. Figure 5.2 shows the considered compressive DIF models.

In this study, the Dynamic Increase Factor (DIF) model from UFC 3-340-02 was utilized, as recommended by military design criteria. Furthermore, the tensile DIF model of tensile strength used the approach proposed by Xu and Wen (2013).

$$\gamma_{ACI349} = \min\left[0.9 + 0.1\{\log_{10}\dot{\varepsilon} + 5\}, 1.25\right] \geq 1 \tag{5.2}$$

$$\gamma_{ACI370R} = \begin{cases} 0.00965\log_{10}\dot{\varepsilon} + 1.058 \geq 1 \text{ for } \dot{\varepsilon} \leq 63.1 \text{ s}^{-1} \\ 0.758\log_{10}\dot{\varepsilon} - 0.289 \leq 2.5 \text{ for } 63.1 \text{ s}^{-1} < \dot{\varepsilon} \end{cases} \tag{5.3}$$

$$\gamma_{fib} = \begin{cases} \left(\dot{\varepsilon} / \dot{\varepsilon}_0\right)^{0.014} & \text{for } 3\times10^{-5} \text{ s}^{-1} \leq \dot{\varepsilon} \leq 30 \text{ s}^{-1} \\ 0.012\left(\dot{\varepsilon} / \dot{\varepsilon}_0\right)^{1/3} & \text{for } 30 \text{ s}^{-1} < \dot{\varepsilon} \leq 300 \text{ s}^{-1} \end{cases} \tag{5.4}$$

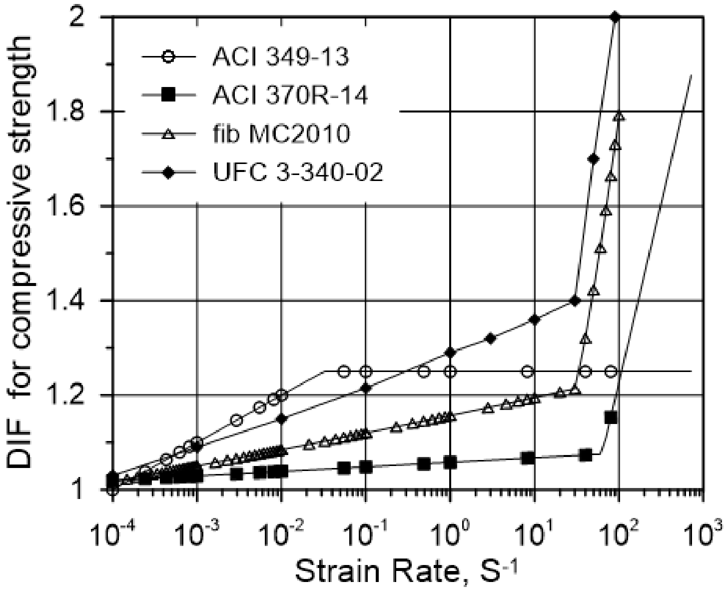

Figure 5.2 DIF models of compressive strength

Table 5.1 Concrete model parameter details (unit: ton, mm, sec)

Description	Symbol	Parameter value
Density	ρ_s	2.35×10^{-9}
Poisson's ratio	ν_s	0.18
Uniaxial tensile strength	f_t	4.06
Maximum failure surface parameters	a_0	15.5
	a_1	0.4463
	a_2	0.001540
Yield failure surface parameters	a_{0y}	14.68
	a_{1y}	0.8989
	a_{2y}	0.001305
Residual failure surface parameters	a_{1f}	0.4417
	a_{2f}	0.0021
Associativity parameter	ω	0.5
Localization width	w_{lz}	25
Damage scaling factors	b_1	1.465
	b_2	1.786
	b_3	1.15

Table 5.2 Default yield scale factor (η)–damage function (λ) relationship

λ	η
0	0
2.8×10^{-5}	0.7
5.0×10^{-5}	0.9
9.0×10^{-5}	1
1.7×10^{-4}	0.9
3.0×10^{-4}	0.75
5.5×10^{-4}	0.54
1.0×10^{-3}	0.33
1.65×10^{-3}	0.14
2.5×10^{-3}	0.09
3.5×10^{-3}	0.032
7.0×10^{-3}	0.005
1.0×10^{10}	0

Table 5.3 EOS model parameters

ε_v	p , MPa	K_u , MPa
0	0	18431
-0.0015	28	18431
-0.0043	60	18689
-0.0101	97	19625
-0.0305	184	23356
-0.0513	277	27088
-0.0726	393	30819
-0.0943	602	33637
-0.174	3514	75672
-0.208	5375	92157

Since the KCC material model in LS-Dyna does not have Element Failure Criteria, the *MAT_ADD_EROSION keyword was employed to eradicate elements where excessive deformation transpires to maintain convergence.

The *MAT_ADD_EROSION in LS-DYNA incorporates erosion failure criteria into the material model. These criteria determine when the material will 'fail' or 'disappear' under load. This failure criterion can be based on strength, deformation, energy, etc. The reason for setting a failure criterion is to accurately track the point at which the material completely breaks down during the modeling process. This functionality is incredibly crucial in scenarios such as collisions, impacts, and fractures.

According to Luccioni et al. (2013), the most commonly used conditions are MXEPS and EPSSH. MXEPS, short for maximum principal strain, is another failure criterion grounded on the strain. Should the material strain exceed the MXEPS threshold, the material is regarded as having failed. EPSSH stands for equivalent plastic strain at shear failure. This criterion is typically applied to ductile materials, which can undergo significant plastic deformation before failing. When the equivalent plastic strain reaches the EPSSH threshold, the material is considered to have failed.

It's imperative to recognize that these failure criteria must be calibrated based on experiments or reliable references to represent the material behavior accurately. Referring to the studies conducted by Luccioni et al. (2013), the Maximum Principal Strain at Failure (MXEPS) was tracked within the range of 0.1 - 0.3, and the Shear Strain at Failure (EPSSH) was traced within the scope of 0.1 - 0.9, based on experimental results in this study, to ensure reliability.

5.2.3. Material model for reinforcing steel

The constitutive model chosen for the reinforcing steels was the piecewise linear plasticity model (MAT 24). The linear properties were presumed to be inherent characteristics of reinforcing bars, as detailed in Table 3.8.

The hardening models were established based on the coupon test results and incorporated as user-defined curves. Regarding the strain-hardening models of reinforcing bars, the Malvar formula (Malvar, 1998; Malvar and Crawford, 1998) is among the most frequently utilized DIF models for supporting bars. It is recognized and adopted in ACI 370R-14, fib MC2010, and UFC 3-340-02 standards. The yield strength of rebars as per the Malvar formula is demonstrated in Equation (5.5).

$$\gamma_y = \left(\frac{\dot{\varepsilon}}{10^{-4}}\right)^{0.074-0.040\frac{f_y}{414}} \tag{5.5}$$

where γ_y is the DIF of yield strength; f_y is yield strength of rebar in the unit of MPa; and $\dot{\varepsilon}$ is strain rate in the unit of s^{-1}. Meanwhile, the piecewise linear plasticity model uses $\sqrt{\dot{\varepsilon}_{ij}\dot{\varepsilon}_{ij}}$ as the strain rate for a DIF.

5.2.4. Material model for projectile

As shown in the experimental results from Chapter 3, the projectile was assumed to be a rigid body using the rigid model (MAT 20), considering the minimal post-collision mass loss of the projectile, which was only 3.3%. The model parameters for the contact condition are presented in Table 5.4. The linear elastic model was applied for the material model of the upper and lower supports, and the material model parameters were established based on the standard characteristics of steel, as shown in Table 5.5.

Table 5.4 Material properties of the projectile

Elastic modulus, GPa	Density, kg/m^3	Poisson's ratio
207	7830	0.28

Table 5.5 Material properties of the upper and bottom supports

Elastic modulus, GPa	Density, kg/m^3	Poisson's ratio
205	7850	0.26

5.2.5. Data acquisition

The FEA outputs included the scaled damage measure (SDM) contour. The SDM is articulated as per Equation (5.6) proposed by Wu and Crawford(2015).

$$\delta = \frac{2\lambda}{\lambda + \lambda_m} \tag{5.6}$$

When the stress state of an element remains elastic, the SDM is zero, and it begins to escalate once the stress state meets the yield failure surface. When the stress state aligns with the maximum failure surface, the SDM equals 1. As the stress state ascends to the residual failure surface, the SDM nears 2.

5.3. Numerical analysis results

5.3.1. Overview of FEA analysis

In the context of Finite Element Analysis (FEA), the mesh test is a critical component of any FEA simulation to ensure the results' accuracy and reliability. The mesh test involves executing the simulation multiple times, varying the mesh size (number of elements) with each run. The objective is to ascertain whether the simulation results converge or become less reliant on the mesh size.

A mesh test was conducted to determine the mesh size. Given the 37mm size of the projectile, which is relatively small compared to the 600mm size of the test specimen, the mesh size for the projectile was adjusted within the 1-3mm range. Subsequently, a mesh test was conducted with variations in the mesh size of the test specimen.

The mesh size of the test specimen varied between 3, 6, 10, 12, 15, 20, 30, and 60 mm, as shown in Figure 5.3, resulting in a total of eight cases. The results are presented in Figure 5.4. Comparing the crash test outcomes and the analytical results for penetration depth, the test specimen's mesh size was set to 10 mm, given the highest similarity in results was observed at this mesh size.

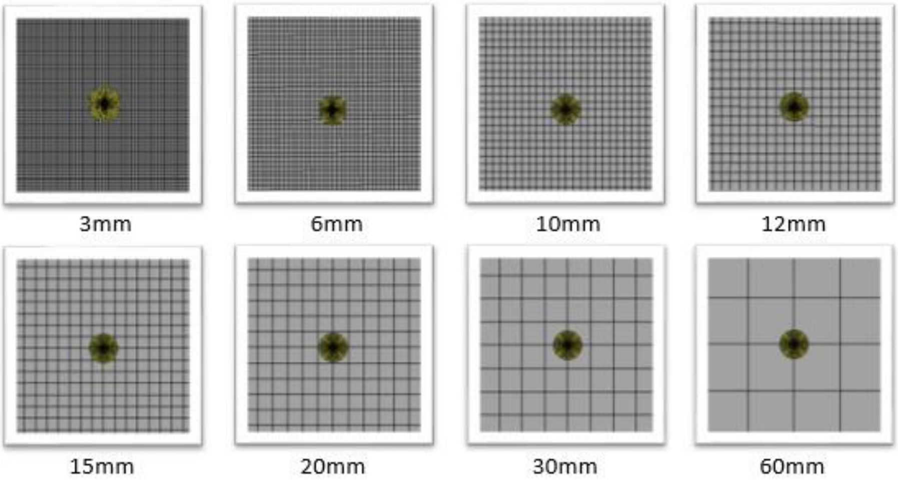

Figure 5.3 Mesh size of specimen for mesh test: total 8 case

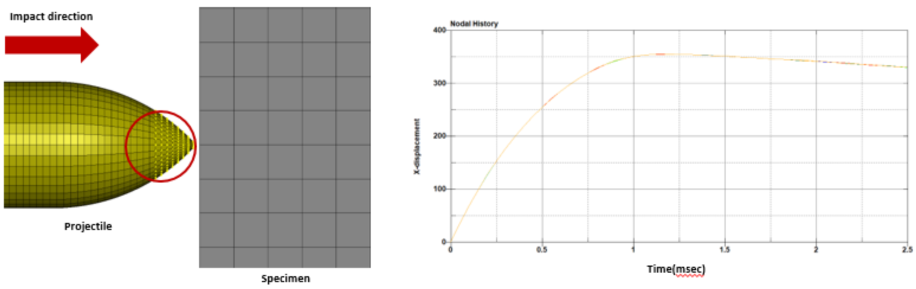

Figure 5.4 Measurement of DOP

To achieve a quantitative assessment of convergence during the mesh test, the DOP by evaluating the maximum displacement of the nodes within the warhead was obtained as shown in Figure 5.4. By comparing the maximum displacements across different mesh sizes, it is possible to gauge the convergence and identify the optimal mesh size that yields accurate and reliable results.

It was common for the depth of penetration (DOP) to increase as the mesh size decreases in a mesh test as shown in Figure 5.5. The specimen mesh size of 10mm was determined to be the most similar to the test results. This suggests that the simulation results obtained with a mesh size of 10mm exhibit the closest convergence and accuracy to the actual behavior. Therefore, the following analyses were performed with a 10mm mesh size.

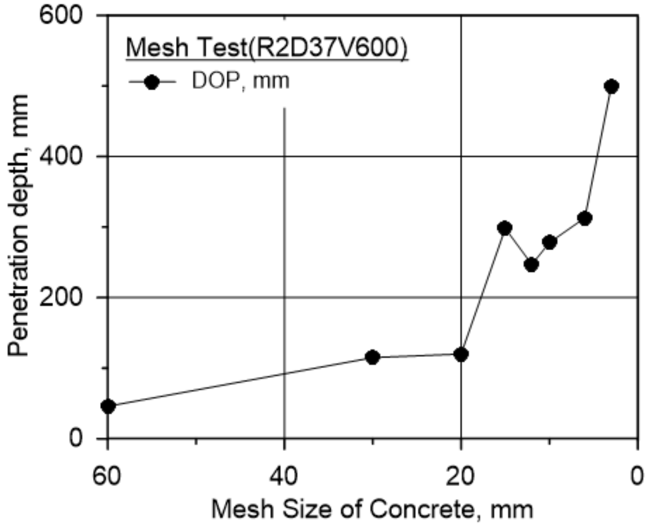

(a)

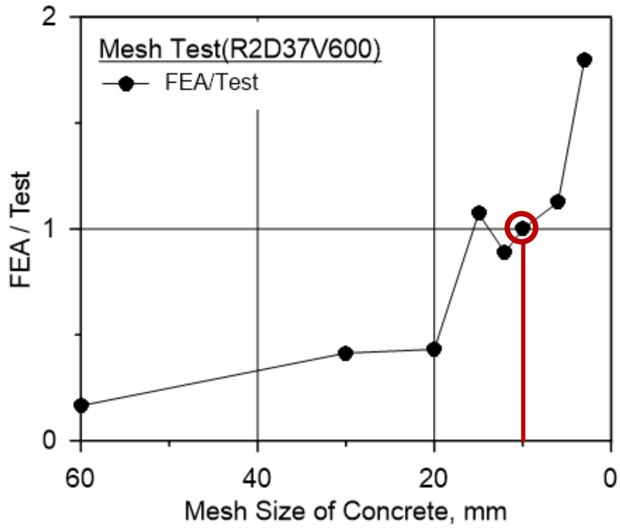

(b)

Figure 5.5 Result of mesh test

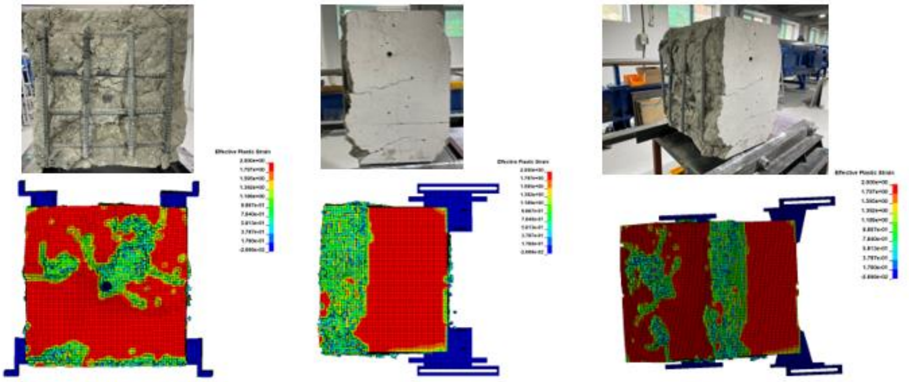

Figure 5.6 Comparison of failure mode with FEA (R1D37V550)

Figure 5.6 shows the 550 m/s impact test results on a specimen with a 1.6% rebar ratio. The damage contours from the finite element analysis predicted the frontal and lateral failure relatively closely, and the shape and extent of the failure confirmed the similarity between FEA and the test.

5.3.2. Effect of reinforcement

In this chapter, the effects of reinforcement were analyzed in terms of DOP, scabbing limit, and perforation limit, using Finite Element Analysis (FEA) results. The sensitivity analysis revealed that the prediction accuracy of DOP depends on the erosion conditions, with a shear strain at failure (SSEPH) of 0.9 showing higher accuracy for velocities up to 700m/s and SSEPH of 0.8 showing higher precision for velocities above 700m/s. In all velocity ranges analyzed, the Maximum Allowable Plastic Strain (MXEPS) value was set to 0.3.

DOP is a significant metric for objectively comparing analysis results. The average accuracy of the DOP predictions was 5.5%, as depicted in Figure 5.7. This result is a reliable indicator, showcasing the interpretation's credibility and reliability.

The failure mode was generally accurately predicted, as evidenced by Table 5.6. However, it was noted that in some cases, FEA tends to overestimate the failure mode of the scabbing limit compared to the experimental result. This phenomenon can be attributed to the conditions associated with erosion. Depending on the degree of scabbing, low, medium, and high were denoted as scabbing. L, scabbing.M, and scabbing. H, respectively.

The findings of FEA also confirm the improved impact resistance as the rebar ratio increases. The analysis showed that the DOP decreases by an average of 6% and up to 15% with an increasing rebar ratio. Additionally, the scabbing and perforation limits increased as the rebar ratio increased. as shown in Table 5.6.

To summarize, it was found that the FEA predicts the experimental results well, and in particular, the improvement of the impact resistance performance due to the increase of the rebar ratio was also confirmed in the FEA.

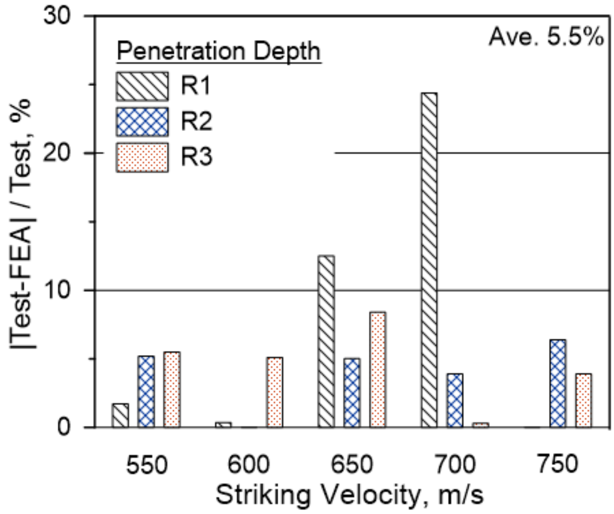

Figure 5.7 Comparison of failure mode with FEA (DOP)

Table 5.6 FEA results and comparison with test

Striking Velocity [m/s]	Designation	Failure mode			Penetration depth [mm]		
		Test	FEA	Match St.	Test(A)	FEA(B)	|A-B|/A, %
535	R1D37V550	Penetration	Scabbing.M	△	233	229	1.70%
	R2D37V550	Penetration	Penetration	O	212	223	5.20%
	R3D37V550	Penetration	Penetration	O	217	229	5.50%
600	R1D37V600	Penetration	Scabbing.M	△	281	280	0.40%
	R2D37V600	Penetration	Scabbing.L	△	278	278	0.00%
	R3D37V600	Penetration	Penetration	O	254	267	5.10%
670	R1D37V650	Scabbing	Scabbing.H	O	376	329	12.50%
	R2D37V650	Penetration	Scabbing.M	△	339	322	5.00%
	R3D37V650	Penetration	Scabbing.L	△	334	306	8.40%
713	R1D37V700	Perforation	Scabbing.H	X	500	378	24.40%
	R2D37V700	Scabbing	Scabbing.H	O	382	397	3.90%
	R3D37V700	Scabbing	Scabbing.H	O	366	367	0.30%
765	R1D37V750	Perforation	Perforation	O	500	500	0.00%
	R2D37V750	Perforation	Perf. limit	O	500	468	6.40%
	R3D37V750	Perf. limit	Scabbing.H	△	415	399	3.90%

5.4. Concluding Remarks

This chapter presents an experimental program in which FEA (Finite Element Analysis) was used to examine damage assessment, penetration depth, scabbing & perforation limit, and the effect of rebar on impact resistance performance using the LS-Dyna program.

The prediction accuracy of the Depth of Penetration (DOP) was reasonably in line with the experimental results, with an average difference of around 5.5%. The erosion conditions influenced the accuracy of these predictions. For situations with velocities of 700m/s or less, a Shear Strain at Failure SSEPH value of 0.9 resulted in better predictive accuracy. On the other hand, for velocities exceeding 700m/s, predictions were more accurate with an SSEPH value of 0.8. However, it was noticed that the FEA tended to overestimate the scabbing limit failure mode compared to the experimental data.

Additional studies confirmed that an increase in the rebar ratio had a significant positive effect on impact resistance. The results showed a decrease in DOP by an average of 6% and by as much as 15% as the rebar ratio increased. The scabbing and perforation limits were also found to grow with the rise in the rebar ratio.

The FEA results, which were consistent with the experimental results, confirmed the reliability of the analysis. Furthermore, the FEA further verified that an increase in the rebar ratio improves the impact resistance performance of the RC target.

6. Conclusion

6.1. Summary and major findings of this study

In this study, the impact resistance of reinforced concrete (RC) targets at a high-velocity range of over 300m/s was investigated, and a modified empirical formula that considers the effect of rebar was suggested. The impact resistance of RC structures is essential for ensuring their safety and durability, especially in regions with a high risk of blast and impact loads, such as military facilities, power plants, and transportation infrastructures.

Experimental tests were conducted using a 12.7mm and 37mm diameter steel projectile with velocities ranging from 550 to 850 m/s to evaluate the accuracy of existing formulae for predicting the impact resistance of RC targets. The test specimens were reinforced with different rebar ratios, ranging from 0% to 3.4%, and the impact resistance was evaluated based on the depth of penetration (DOP), scabbing area, crack size, perforation limit, and mass loss. The test results showed that Conwep's model had the highest prediction accuracy for DOP(Conwep 0.97, ACE 0.83, NDRC 0.73, UKAEA 0.72), scabbing, and perforation limits. In contrast, the equations based on the nuclear power plant design criteria developed for aircraft collision situations are beyond the scope of application, such as collision speeds above 300 m/s, and therefore show over 1.6 times limit velocity low accuracy compared to the experimental results of this study simulating military ammunition collision situations, so caution should be exercised when considering military ammunition collision situations.

Moreover, the effect of rebar on the impact resistance of RC targets was investigated by comparing the test results of specimens with different rebar ratios. The results showed that the impact resistance of RC targets improved as the rebar ratio increased. Specifically, the DOP was reduced by up to 11% and, on average, by 7%, and the size of the crack and scabbing area on the exit surface and the mass loss of specimens were reduced. The scabbing and perforation limits were also increased 50~70m/s as the rebar ratio increased.

Based on the collected test data 153ea, a modified empirical formula that considers the effect of rebar was suggested. The modified formula was verified by comparing its prediction results with the test data, and it showed good accuracy at a high-velocity range(Proposed formula 0.97, Conwep 0.83, ACE 0.74, NDRC 0.69, UKAEA 0.68). In addition, FEA simulations were conducted to verify and apply the modified formula and rebar effect for impact tests on RC targets. The suggested empirical formula and rebar effect was verified through collected test data and additional FEA simulations.

Considering the rebar's effect, the suggested modified empirical formula can be used to predict the impact resistance of RC targets at a high-velocity range. The results of this study provide valuable insights into improving the accuracy of existing formulae and enhancing the impact resistance of RC structures. Further studies are needed to investigate the applicability of the modified empirical formula to different types of RC structures and impact scenarios and further to improve the accuracy and reliability of the formula.

6.2. Recommendations for further studies

There are several recommendations for further studies to improve the understanding and prediction of the impact resistance of reinforced concrete (RC) structures.

Firstly, this research concentrated on the impact resistance of RC targets, using mainly a 37mm projectile for the experiments. Expanding this investigation to other RC structures, such as beams, columns, and walls, and comparing their impact resistance with RC targets is necessary. Also, collision experiments involving ogive-nose steel projectiles of varying sizes and masses are recommended, as experimental data were scarce on the rebar ratio at high impact speeds in the existing literature. A broader and more diverse collection of experimental data is required for a comprehensive review.

Secondly, this research employed a modified empirical formula accounting for the effect of rebar on the impact resistance of RC targets. However, the rebar ratio's effects on the test object's relative size and projectile merit investigation. While the effect of the rebar ratio was confirmed for a 37mm projectile, its impact was not evident for a 12.7mm projectile. There might be an effect of the rebar ratio on impact performance based on relative size. Therefore, the impacts of other factors, including concrete strength, thickness, boundary conditions, and relative dimensions of the specimen and projectile, should be further explored to enhance the formula's accuracy and reliability.

Lastly, numerical simulation techniques, such as finite element analysis (FEA), provide a comprehensive investigation of the impact resistance of RC structures. Combining experimental and numerical approaches could enhance our understanding of RC structures' impact resistance and predictive capabilities.

In conclusion, further research should focus on various projectile sizes and masses, the impact of rebar ratios at high impact speeds, and the role of relative size in the effectiveness of the rebar ratio on the impact resistance of RC structures. Furthermore, additional investigation is necessary to explore the impact resistance of various types of RC structures, the effects of diverse factors on their impact resistance, and the utility of numerical simulations in improving the prediction and design of RC structures subjected to impact loads.

Reference

Kennedy RP. A review of procedures for the analysis and design of concrete structures to resist missile impact effects. Nuclear Engineering and Design. 1976. 37(2): p.183-203.

DMFC 2-20-10. Design codes on blast and bullet resistance. ROK Defense Installations Agency. 2017.

ESL-TR-87-57. Protective construction design manual. Florida. US Air Force Engineering Services Laboratory. 1987

Army T. Fundamentals of protective design for conventional weapons, Report TM 5-855-1. US Department of the army. 1986.

A. Amirikian. Design of protective structures, Report NT-3726. Bureau of Yards and Docks. US Department of the Navy. 1950.

Michael D, Norval D, Joseph PC. Structures to resist the effects of accidental explosions, ARLCD-SP-84001. 1987.

Hwarang-dae Research Institute. Design Standards for Protective Structures. ROK Ministry of National Defense. 1998

Mays GC, Williams MS. Assessment, strengthing, harding, repair and demolition of structures, military engineering, vol. IX. London: Ministry of Defence; 1992.

Li QM, Reid SR, Wen HM, Telford AR. Local impact effects of hard missiles on concrete targets. International Journal of Impact Engineering. 2005. 32(1): p.224-84.

Kim S, Kang TH, Do Yun H. Evaluation of impact resistance of steel fiber-reinforced concrete panels using design equations. ACI Structural Journal. 2017;114(4):911.

ACE. Fundamentals of Protective Structures, Report AT120 AT1207821. Army Corps of Engineering. 1946.

Hyde D. ConWep: Conventional weapons effects (Application of TM 5-855-1). US Army Corps of Engineers, Waterways Experiment Station, Vicksburg, MS. 1992.

Beth RA. Penetration of projectiles in concrete. PPAB Interim Report No. 3, November 1941.

NDRC. Effects of Impact and Explosion (Summary Technical Report of Division 2): National Defense Research Committee. 1946.

Berriaud C, Sokolovsky A, Gueraud R, Dulac J, Labrot R. Comportement local des enceintes en beton sous l'impact d'un projectile rigide: Local behaviour of reinforced concrete walls under missile impact. Nuclear Engineering and Design. 45(2): p.457-69. 1978.

Barr P. Guidelines for the design and assessment of concrete structures subjected to impact. Report, UK Atomic Energy Authority, Safety and Reliability Directorate, HMSO, London. 1990.

Degen PP. Perforation of reinforced concrete slabs by rigid missiles. J Struct Div. ASCE. 1980.

Chang WS. Impact of solid missiles on concrete barriers. J Struct Div. ASCE. 1981.

BPC. Design of structures for missile impact, Topical Report BC-TOP-9-A. Bechtel Power Corporation. 1974.

Jankov ZD, Shanahan JA, White MP. Missile tests of quarter-scale reinforced concrete barriers. Proceedings of a symposium on tornadoes, assessment of knowledge and implications for man. Lubbock, TX: Texas Technical University; June 1976.

Sliter GE. Assessment of empirical concrete impact formulas. J Struct Div . ASCE. 1980.

Kojima I. An experimental study on local behaviour of reinforced concrete slabs to missile impact. Nucl Eng Des ; 130:121–32. 1991.

ACI Committee 349. Code Requirements for Nuclear Safety-Related Concrete Structures (ACI 349-13) & Commentary. American Concrete Institute. Farmington Hills, MI. 2014.

Erin Engineering & Research, Inc. Methodology for performing aircraft impact assessments for new plant designs. Erin Engineering & Research, Inc. California. 2009.

U.S. Department of Energy. Accident analysis for aircraft crash into hazardous facilities. Washington D.C., U.S: Department of Energy Standard DOE-STD-3014-2006; 2006.

Hansson H. A note on empirical formulas for the prediction of concrete penetration. FOI-Swedish Defence Research Agency, Weapons and Protection, SE-147. 2003.

Kennedy RP. Effects of an Aircraft Crash Into a Concrete Reactor Containment Building: Holmes & Narver. 1966.

Adeli H, Amin A. Local effects of impactors on concrete structures. Nuclear Engineering and design. 1985.

Forrestal MJ, Altman BS, Cargile JD, Hanchak SJ. An empirical equation for penetration depth of ogive-nose projectiles into concrete targets. International Journal of Impact Engineering. 1994. 15(4): p.395-405.

Forrestal M, Frew D, Hanchak S, Brar N. Penetration of grout and concrete targets with ogive-nose steel projectiles. International Journal of Impact Engineering. 1996. 18(5): p.465-76.

Frew DJ, Hanchak SJ, Green ML, Forrestal MJ. Penetration of concrete targets with ogive-nose steel rods. International Journal of Impact Engineering. 1998. 21(6): p.489-97.

Forrestal MJ, Frew DJ, Hickerson JP, Rohwer TA. Penetration of concrete targets with deceleration-time measurements. International Journal of Impact Engineering. 2003. 28(5): p.479-97.

Williams MS. Modeling of local impact effects on plain and reinforced concrete. Structural Journal. 1994. 91(2): p.178-87.

Abdel-Kader M, Fouda A. Effect of reinforcement on the response of concrete panels to impact of hard projectiles. International Journal of Impact Engineering. 2014. 63: p.1-17.

Sangho L, Chunghyeon K, Yongjae Y, Jae-Yeol C. Effect of Reinforcing Steel on the Impact Resistance of Reinforced Concrete Panel Subjected to Hard-Projectile Impact. International Journal of Impact Engineering. 2020.

MIL-STD-662F. Department of defense test method standard : V50 Ballistic test for armor. Department of defense. 1997.

TM 9-1904. Ammunition Inspection Guide. United States Department of War. 1944.

ASTM C39. Standard test method for compressive strength of cylindrical concrete specimens. ASTM International. West Conshohocken, PA, U.S. 2020.

ASTM E8M. Standard test method for tension testing of metallic materials. ASTM International. West Conshohocken, PA, U.S. 2016.

Magnusson J, Unosson M, Carlberg A. High performance concrete" HPC"-field experiments and production. Totalförsvarets forskningsinstitut. 2001.

Gran JK, Frew DJ. In-target radial stress measurements from penetration experiments into concrete by ogive-nose steel projectiles. International Journal of Impact Engineering. 1997. 19(8): p.715-26.

Dancygier AN, Yankelevsky DZ, Jaegermann C. Response of high performance concrete plates to impact of non-deforming projectiles. International Journal of Impact Engineering. 2007. 34(11):1768-79.

Zhang X, Wu H, Zhang S, Huang F. Projectile penetration of reinforced concrete considering the effect of steel reinforcement: Experimental study and theoretical analysis. International journal of impact engineering. 2020. 144:103653.

Unified Facilities Criteria (UFC) 3-340-02. Structures to Resist the Effects of Accidental Explosions. Department of Defense. Washington D.C., U.S. 2008.

Xu, H., and H.M. Wen. Semi-empirical equations for the dynamic strength enhancement of concrete-like materials. International Journal of Impact Engineering, 2013. 60: p. 76-81.

Markovich, N., E. Kochavi, and G. Ben-Dor. An improved calibration of the concrete damage model. Finite Elements in Analysis and Design, 2011. 47(11): p. 1280-1290.

Wu, Y., and J.E. Crawford. Numerical modeling of concrete using a partially associative plasticity model. Journal of Engineering Mechanics, 2015. 141(12): p. 04015051.

Kong, X. Q. Fang, Q.M. Li, H. Wu, and J.E. Crawford. Modified K&C model for cratering and scabbing of concrete slabs under projectile impact. International Journal of Impact Engineering, 2017. 108: p.217-228.

Luccioni BM, Aráoz GF, Labanda NA. Defining Erosion Limit for Concrete. International journal of protective structures. 2013. 4(3):315-40.

Bishop, R. F., Hill, R., & Mott, N. F. The theory of indentation and hardness tests. Proceedings of the Physical Society. 1945. 57(3), 147.

Hill, R. A theory of earth movement near a deep underground explosion. Armament Research Establishment, Memo. 1948. (21-48).

Hopkins, H. G. Dynamic expansion of spherical cavities in metals. Progress in solid mechanics.1960. 1(3), 5-16.

H. Wu, Q. Fang, Y. Peng, Z. M. Gong, and X. Z. Kong, Hard projectile perforation on the monolithic and segmented RC panels with a rear steel liner, International Journal of Impact Engineering, Vol. 76. 2015.

Joy, S., & Ehrgott, J. Q. Material Characterization of SAC-5 Concrete. In Private communication. US Army Waterways Experiment Station Vicksburg.1993. MS 39180-6199.

Hanchak, S. J., Forrestal, M. J., Young, E. R., & Ehrgott, J. Q. Perforation of concrete slabs with 48 MPa (7 ksi) and 140 MPa (20 ksi) unconfined compressive strengths. International Journal of Impact Engineering. 1992. 12(1), 1-7.

Reid SR, Wen HM. Predicting penetration, cone cracking, scabbing and perforation of reinforced concrete targets struck by flat-faced projectiles. UMIST Report ME/AM/02.01/TE/G/018507/Z, 2001.

Fullard K, Baum MR, Barr P. The assessment of impact on nuclear power plant structures in the United Kingdom. Nucl Eng Des 1991.

Forrestal MJ, Tzou DY. A spherical cavity-expansion penetration model for concrete targets. International Journal of Solids and Structures. 1997.

Appendix A

Experimental Results of Unconfined Compression Tests

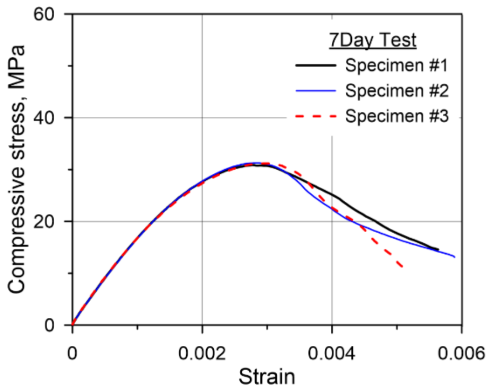

(a)

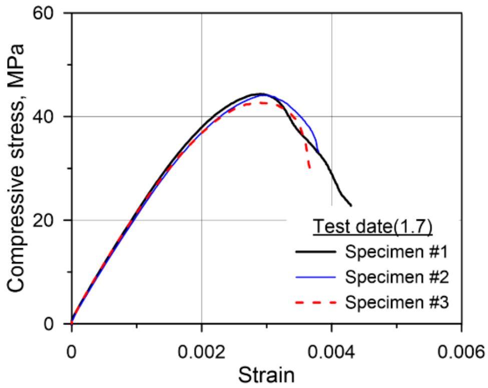

(b)

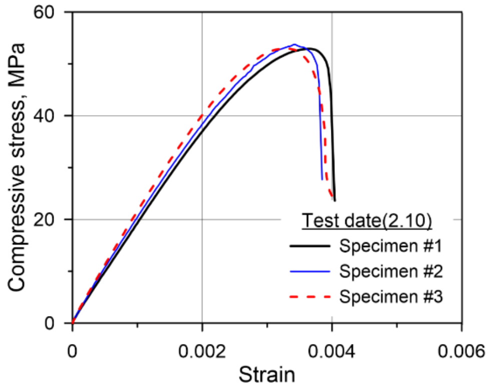

(c)

Figure A.1 Stress-strain curve for concrete cylinder;

(a) 7days; (b) 28days; (c) 65days

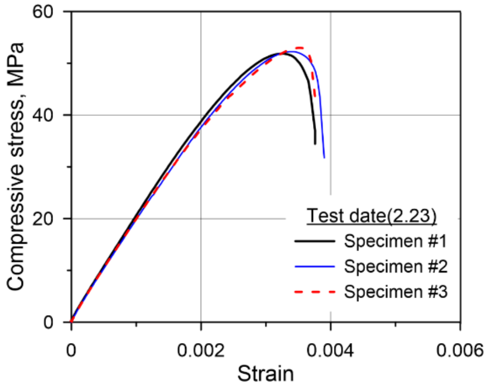

(a)

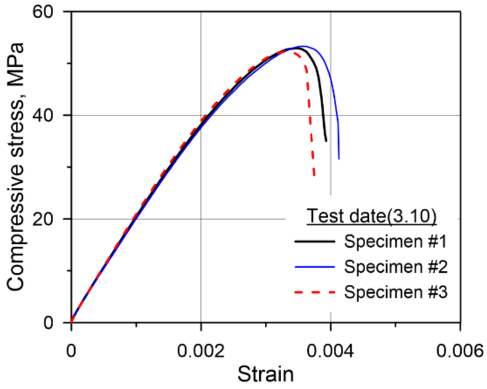

(b)

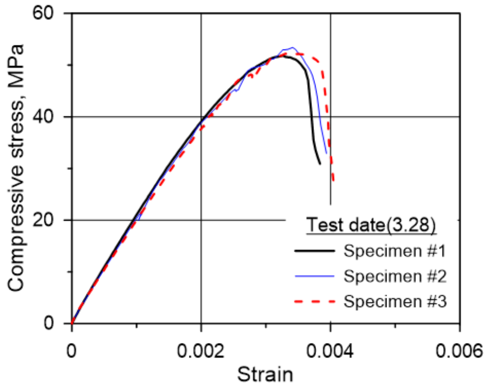

(c)

Figure A.2 Stress-strain curve for concrete cylinder; (a) 78days; (b) 93days; (c) 111days

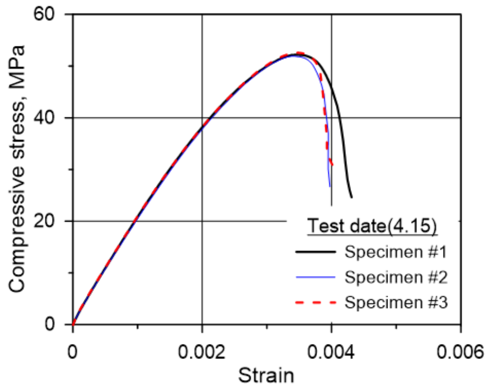

(a)

Figure A.3 Stress-strain curve for concrete cylinder; (a) 129days

Appendix B

Experimental Results of Strain of Rebar

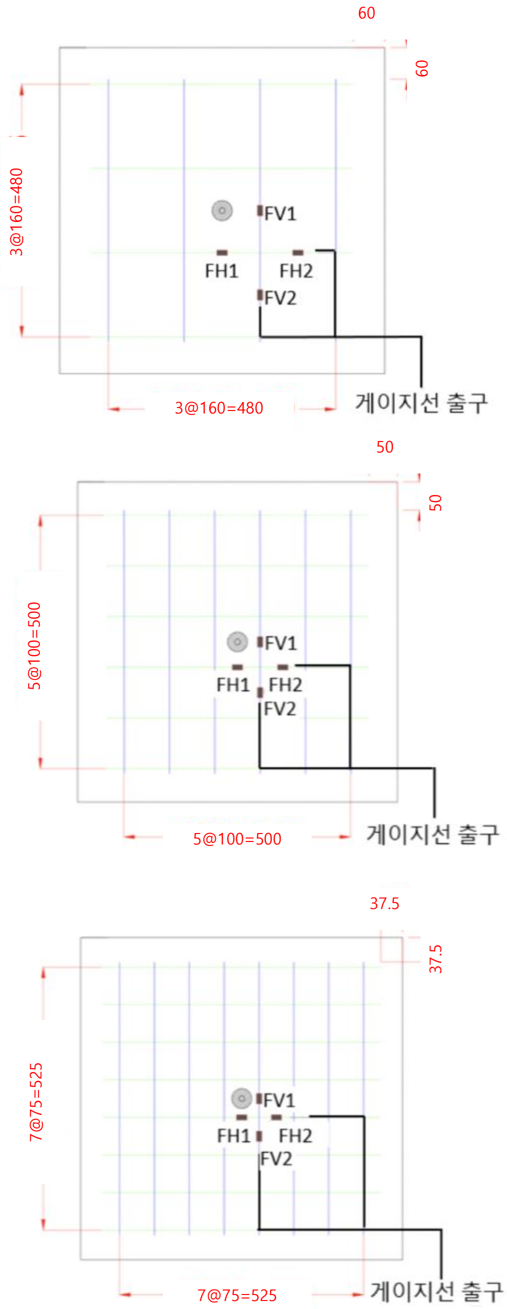

Figure B.1 Rebar Strain Gauge Attachment Location

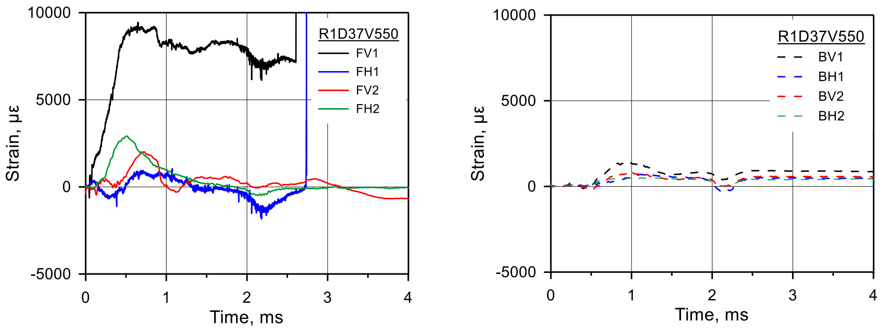

(a) (b)

Figure B.2 Time-strain curve for rebar(R1D37V550); (a) Front; (b) Back

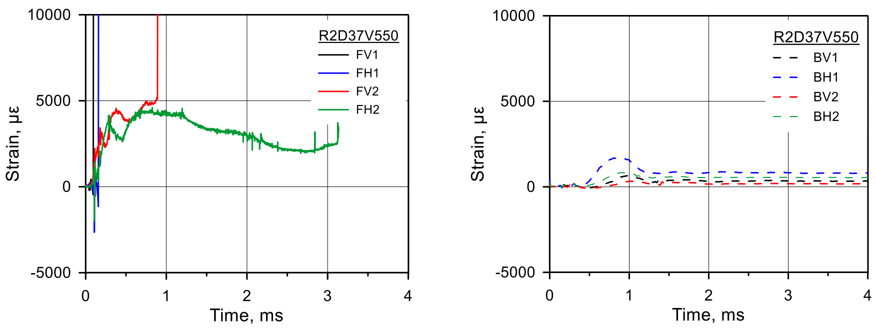

(a) (b)

Figure B.3 Time-strain curve for rebar(R2D37V550); (a) Front; (b) Back

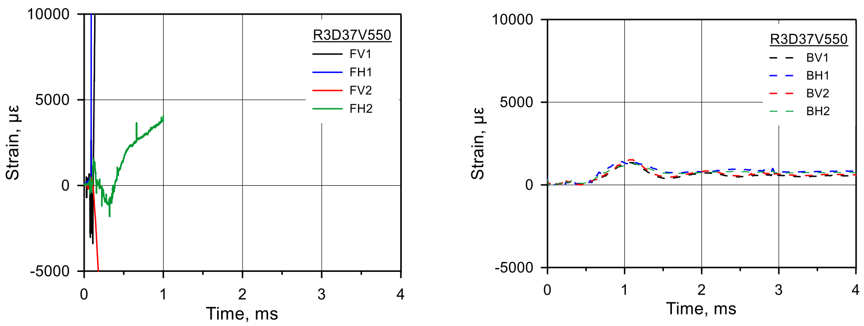

(a) (b)

Figure B.4 Time-strain curve for rebar(R3D37V550); (a) Front; (b) Back

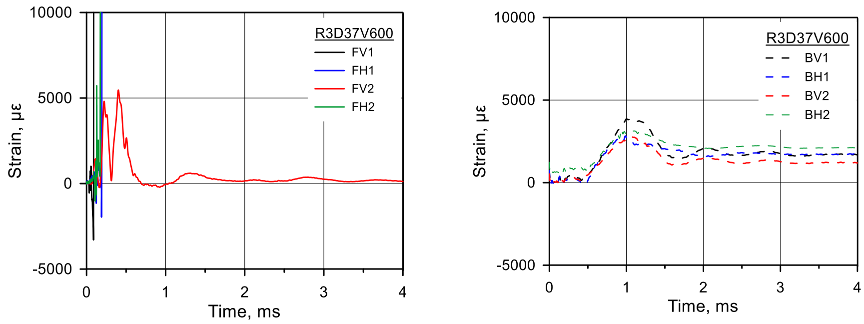

(a) (b)

Figure B.5 Time-strain curve for rebar(R1D37V600); (a) Front; (b) Back

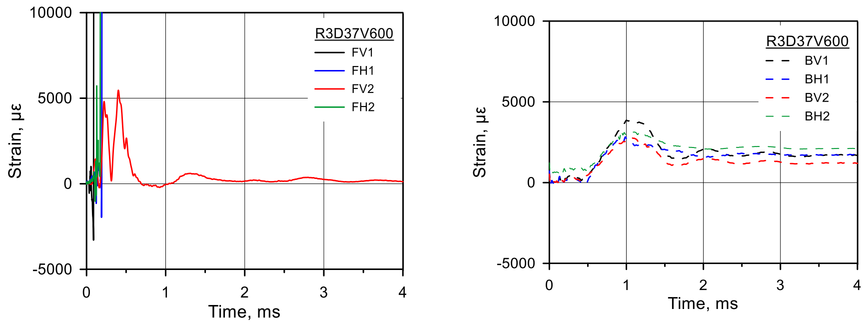

(a) (b)

Figure B.6 Time-strain curve for rebar(R2D37V600); (a) Front; (b) Back

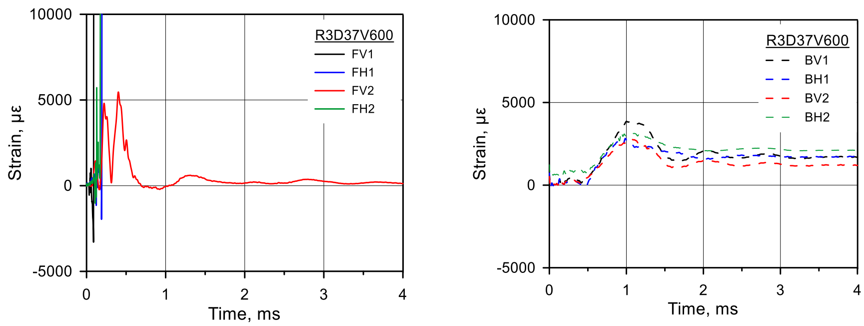

(a) (b)

Figure B.7 Time-strain curve for rebar(R3D37V600); (a) Front; (b) Back

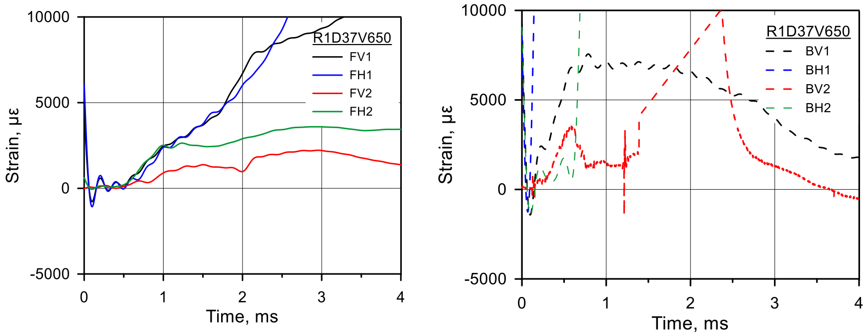

(a) (b)

Figure B.8 Time-strain curve for rebar(R1D37V650); (a) Front; (b) Back

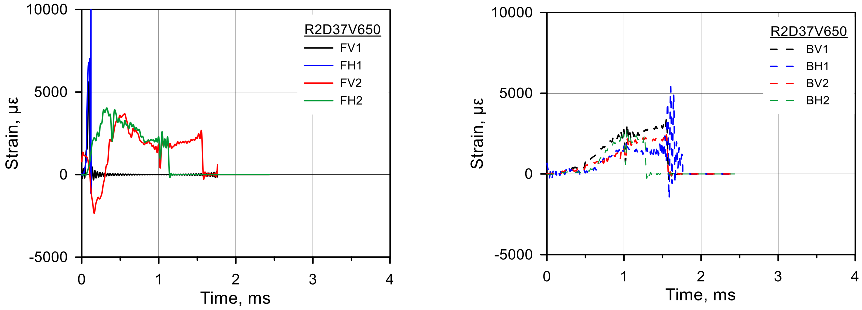

(a) (b)

Figure B.9 Time-strain curve for rebar(R2D37V650); (a) Front; (b) Back

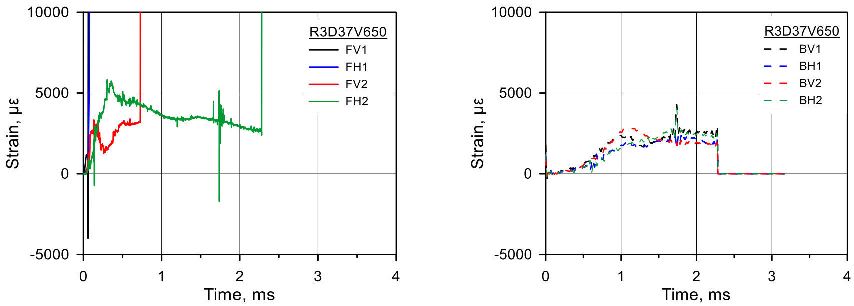

(a) (b)

Figure B.10 Time-strain curve for rebar(R3D37V650); (a) Front; (b) Back

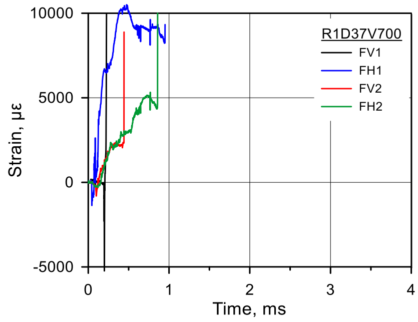

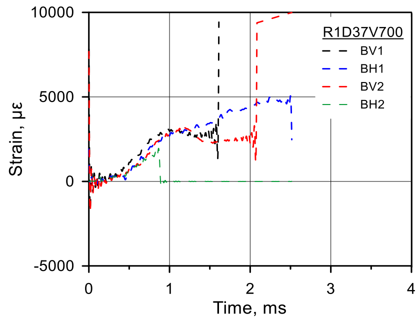

(a) (b)

Figure B.11 Time-strain curve for rebar(R1D37V700); (a) Front; (b) Back

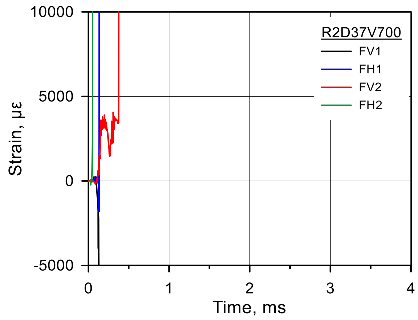

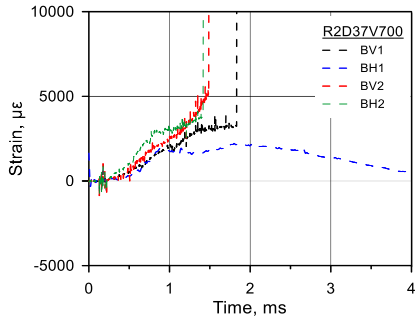

(a) (b)

Figure B.12 Time-strain curve for rebar(R2D37V700); (a) Front; (b) Back

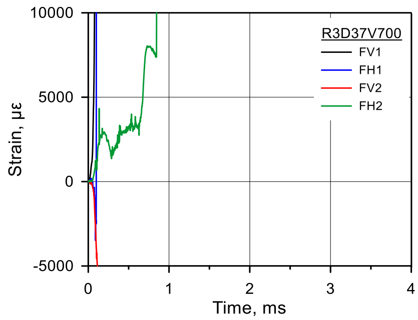

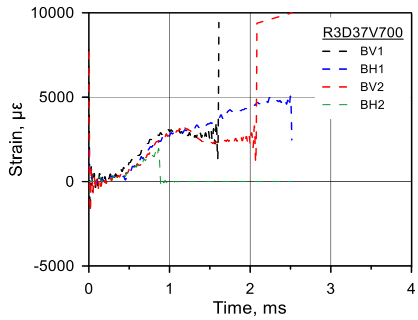

(a) (b)

Figure B.13 Time-strain curve for rebar(R3D37V700); (a) Front; (b) Back

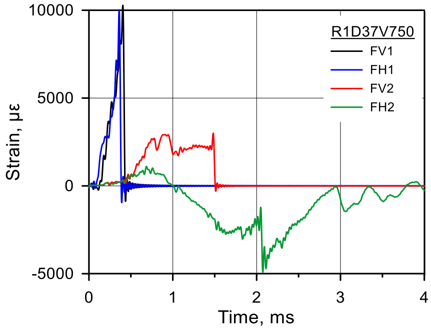

(a)

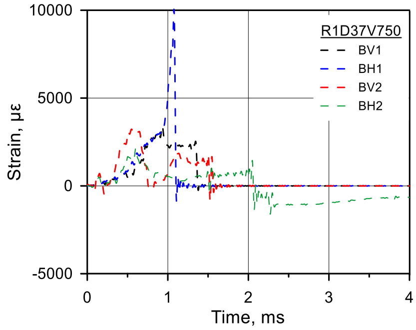

(b)

Figure B.14 Time-strain curve for rebar(R1D37V750); (a) Front; (b) Back

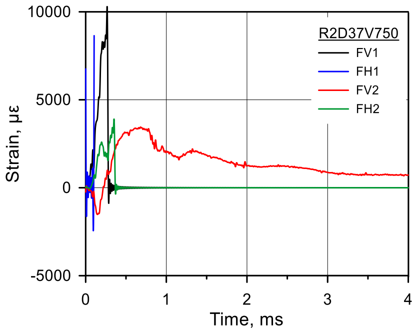

(a)

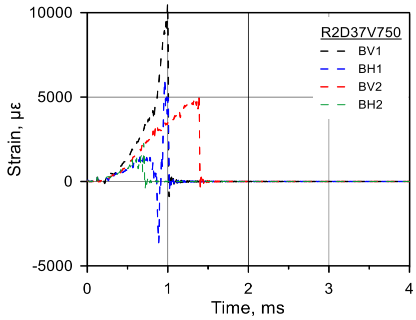

(b)

Figure B.15 Time-strain curve for rebar(R2D37V750); (a) Front; (b) Back

Appendix C

Experimental Results of Using 3D Scanner

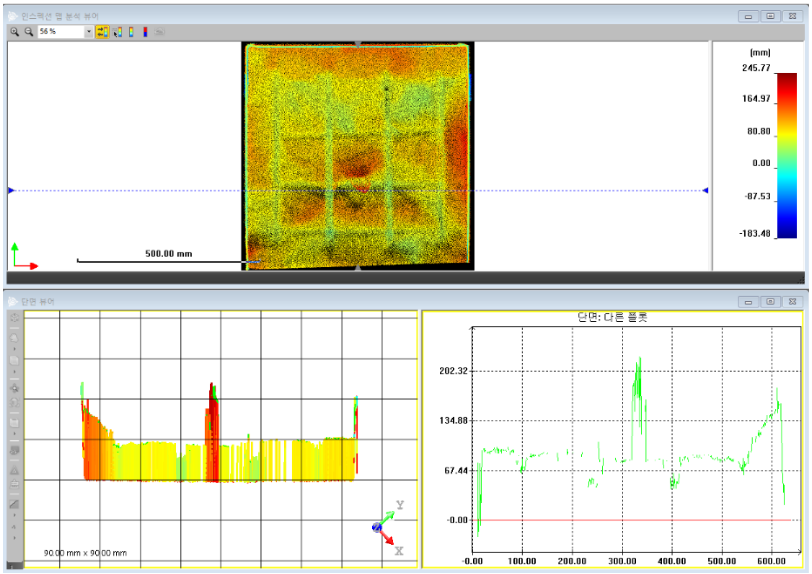

(a)

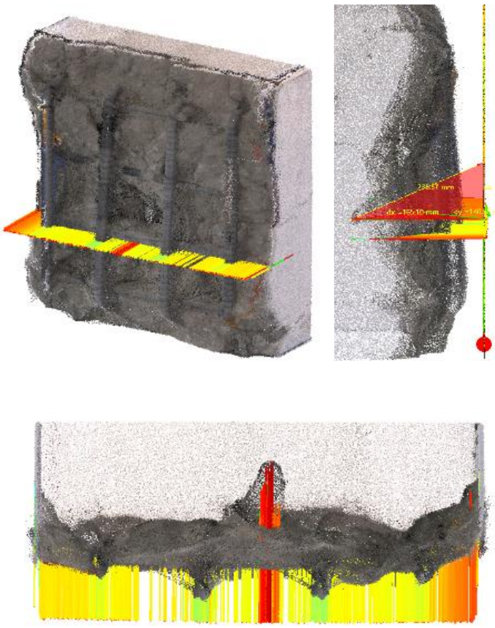

(b)

Figure C.1 3D Scanner analysis images; R1D37V550

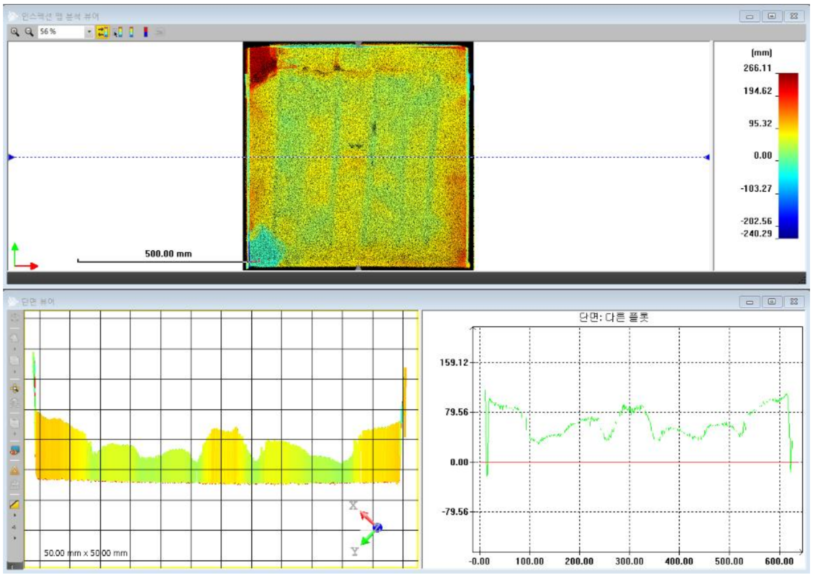

(a)

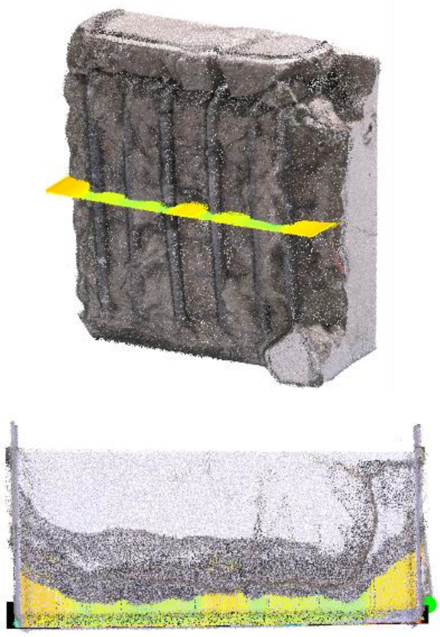

(b)

Figure C.2 3D Scanner analysis images; R2D37V550

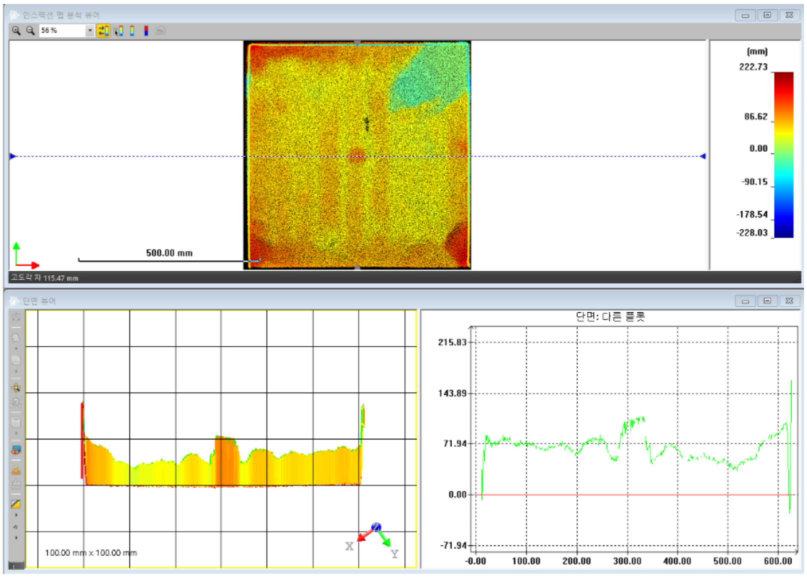

(a)

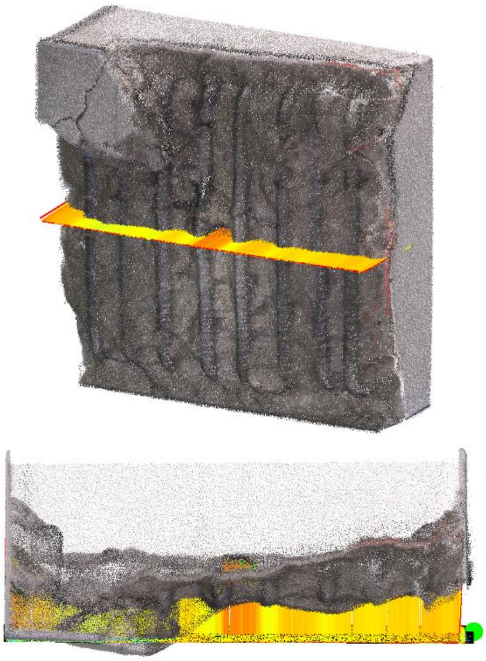

(b)

Figure C.3 3D Scanner analysis images; R3D37V550

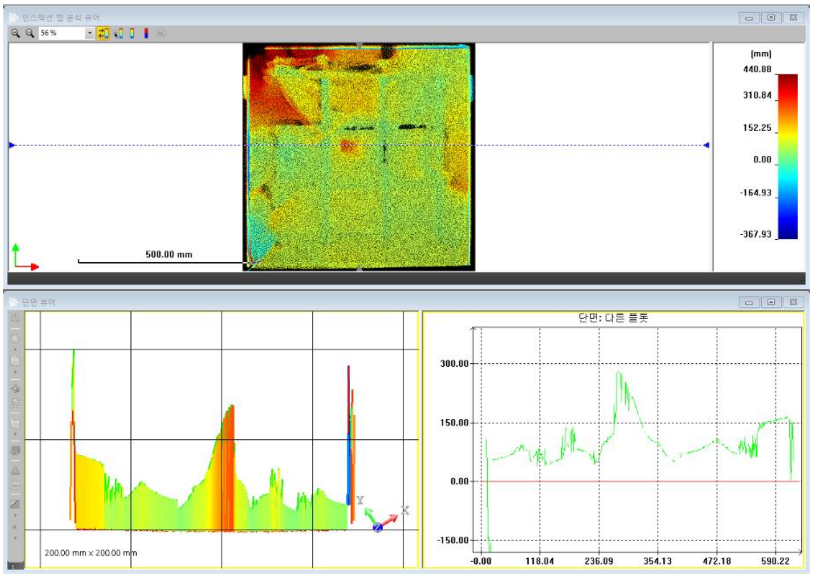

(a)

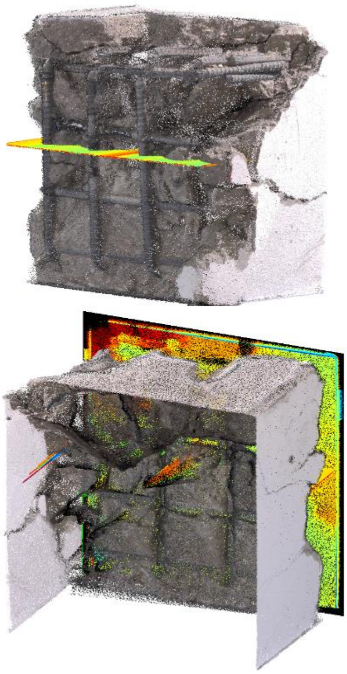

(b)

Figure C.4 3D Scanner analysis images; R1D37V600

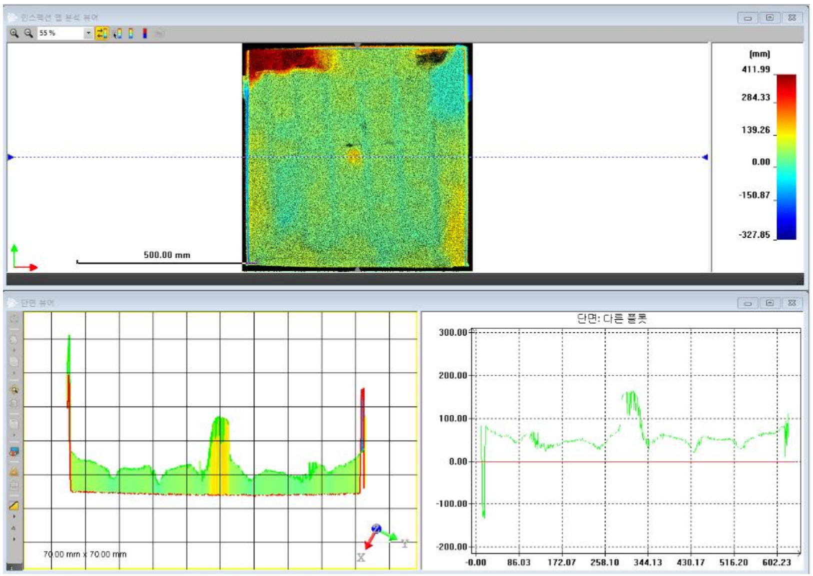

(a)

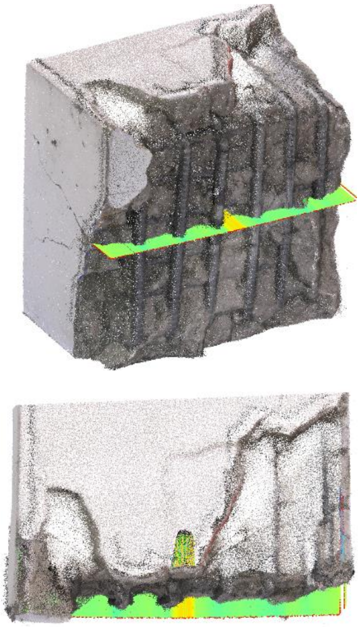

(b)

Figure C.5 3D Scanner analysis images; R2D37V600

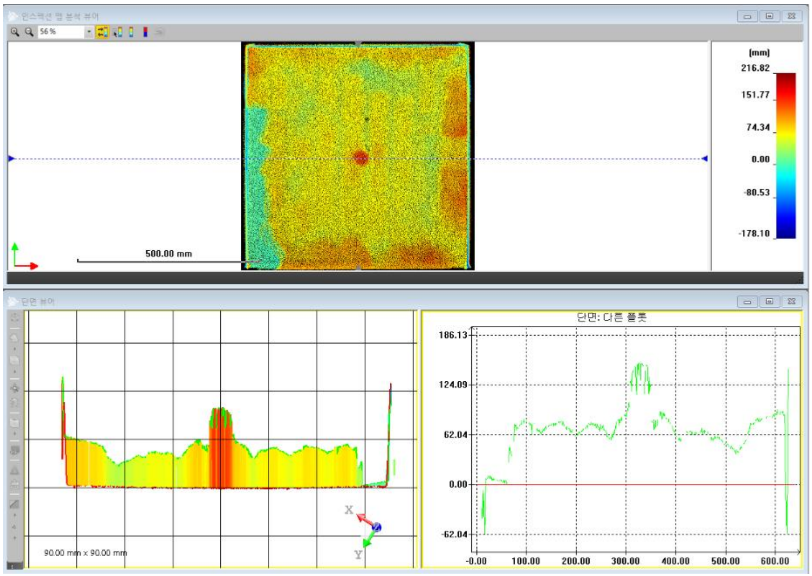

(a)

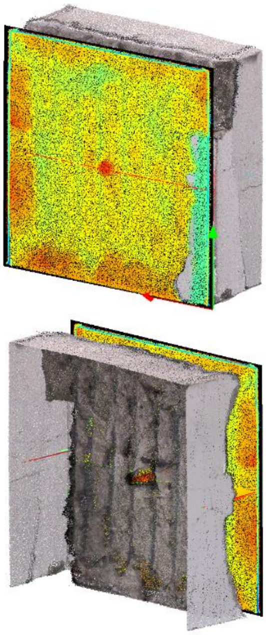

(b)

Figure C.6 3D Scanner analysis images; R3D37V600

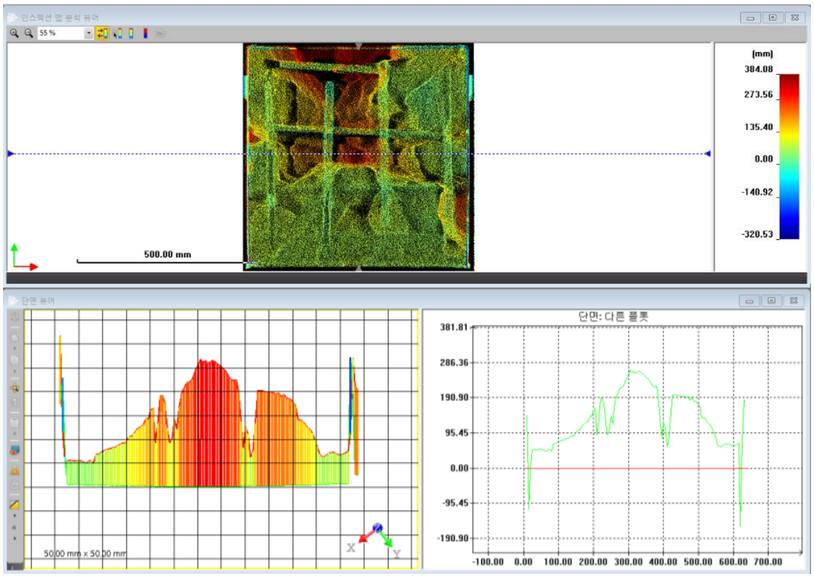

(a)

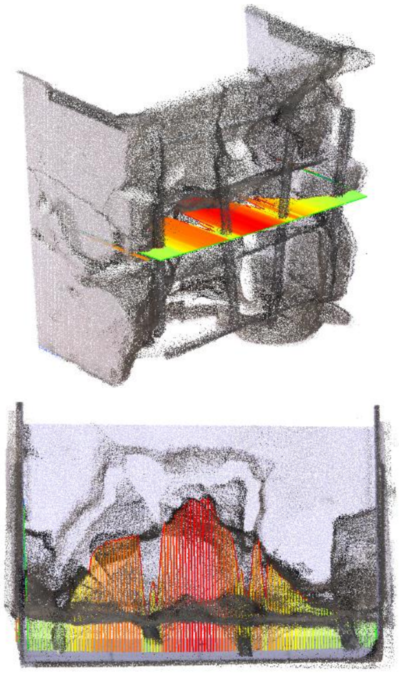

(b)

Figure C.7 3D Scanner analysis images; R1D37V650

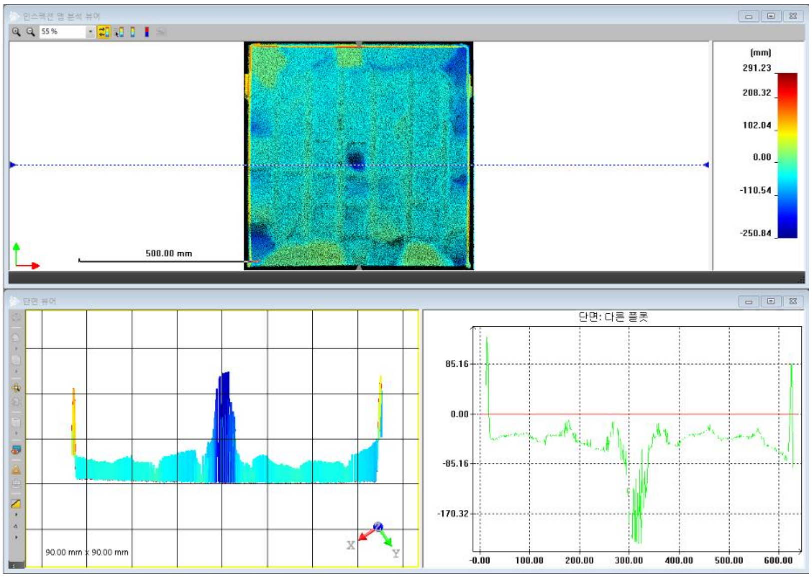

(a)

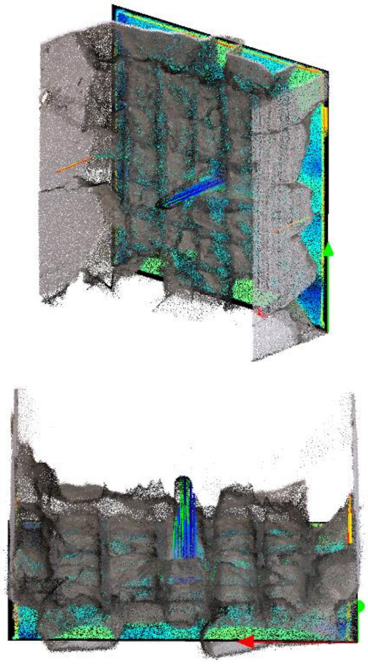

(b)

Figure C.8 3D Scanner analysis images; R2D37V650

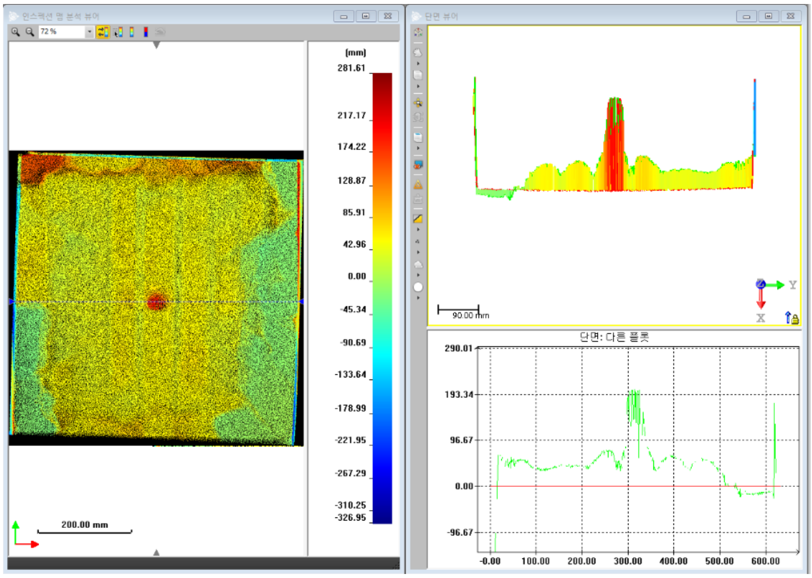

(a)

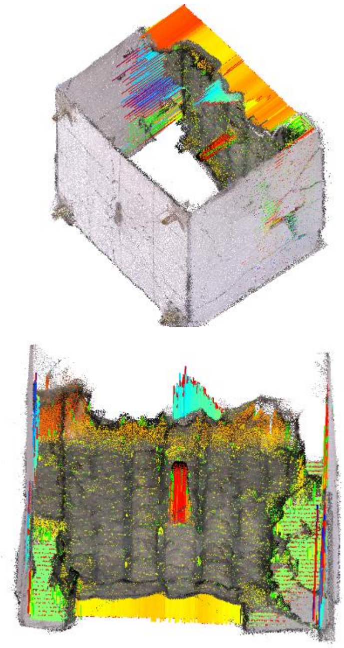

(b)

Figure C.9 3D Scanner analysis images; R3D37V650

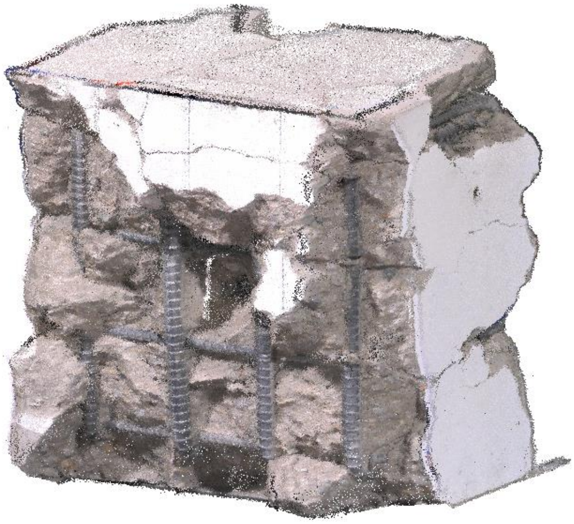

(a)

(b)

Figure C.10 3D Scanner analysis images; R1D37V700(Perforation)

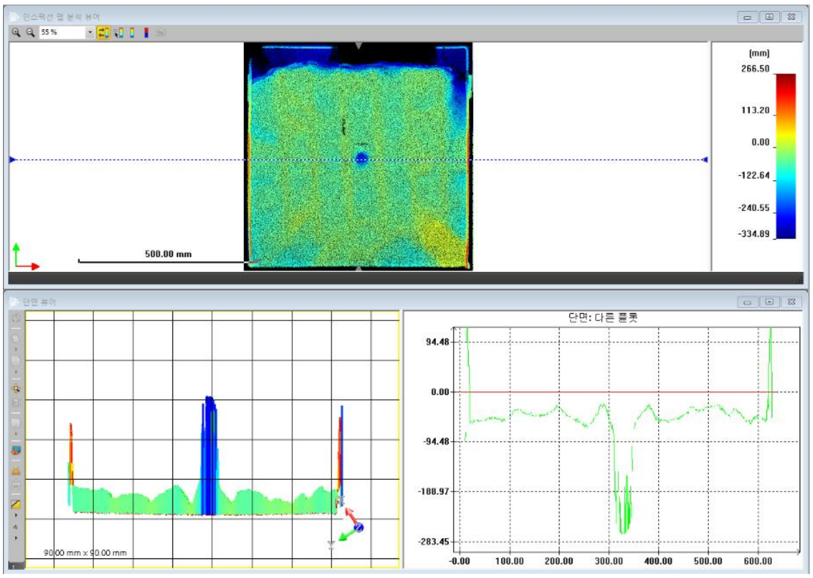

(a)

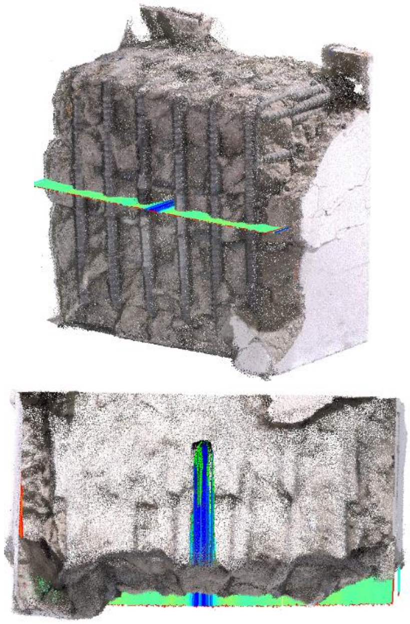

(b)

Figure C.11 3D Scanner analysis images; R2D37V700

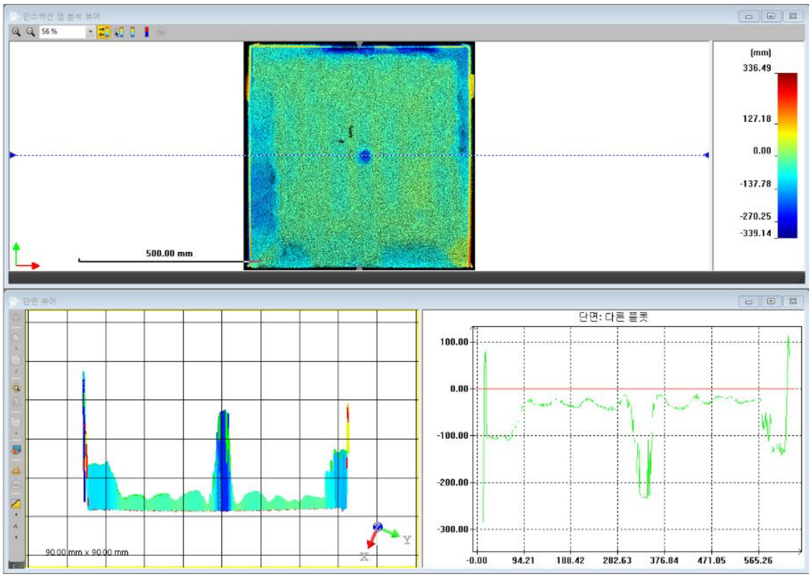

(a)

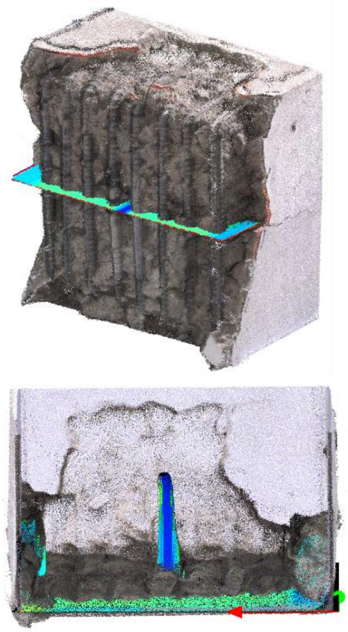

(b)

Figure C.12 3D Scanner analysis images; R3D37V700

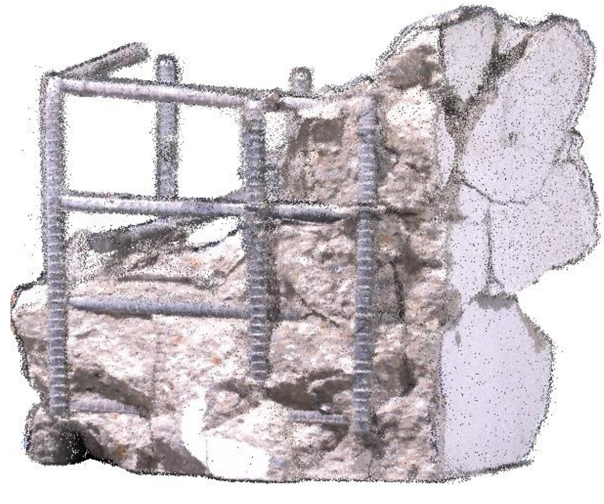

(a)

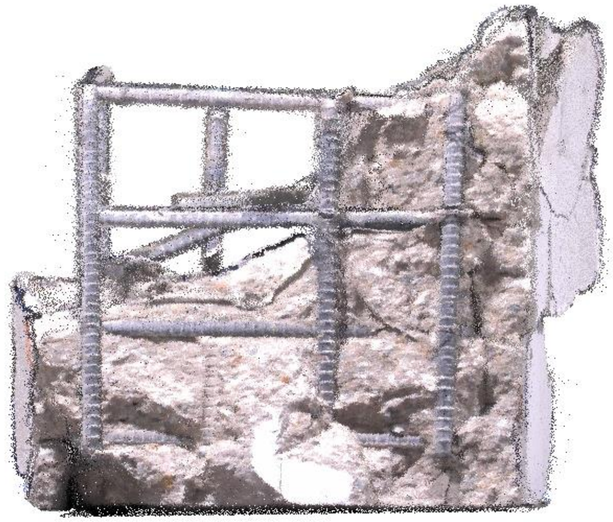

(b)

Figure C.13 3D Scanner analysis images; R1D37V750(Perforation)

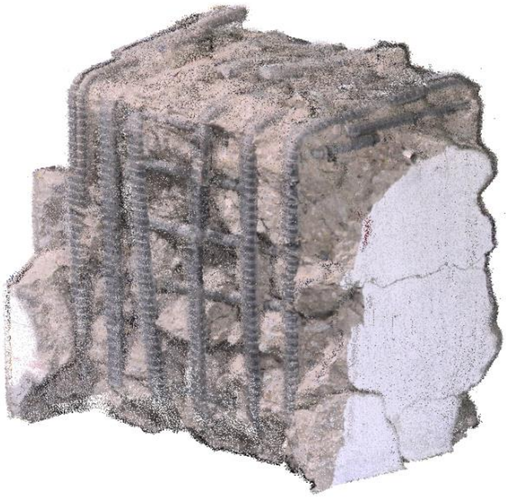

(a)

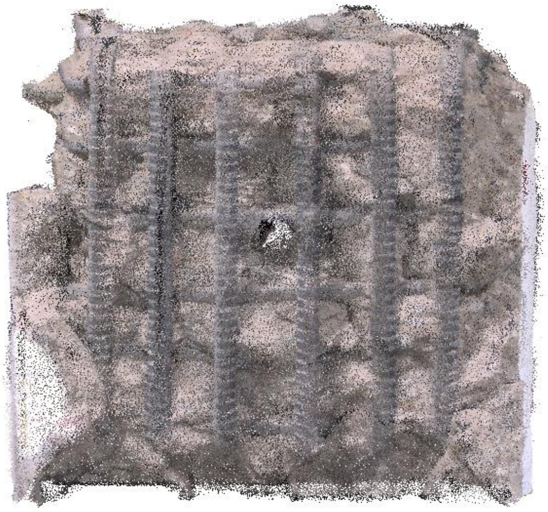

(b)

Figure C.14 3D Scanner analysis images; R2D37V750(Perforation)

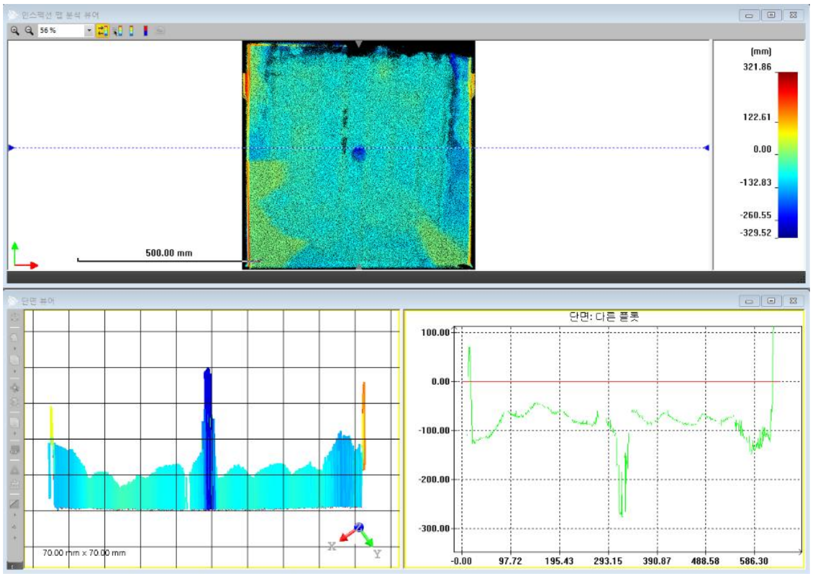

(a)

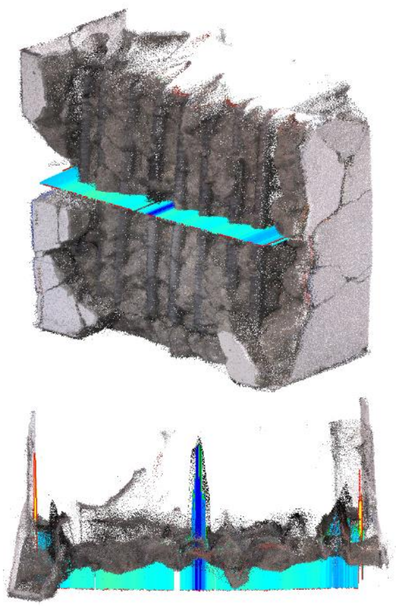

(b)

Figure C.15 3D Scanner analysis images; R3D37V750

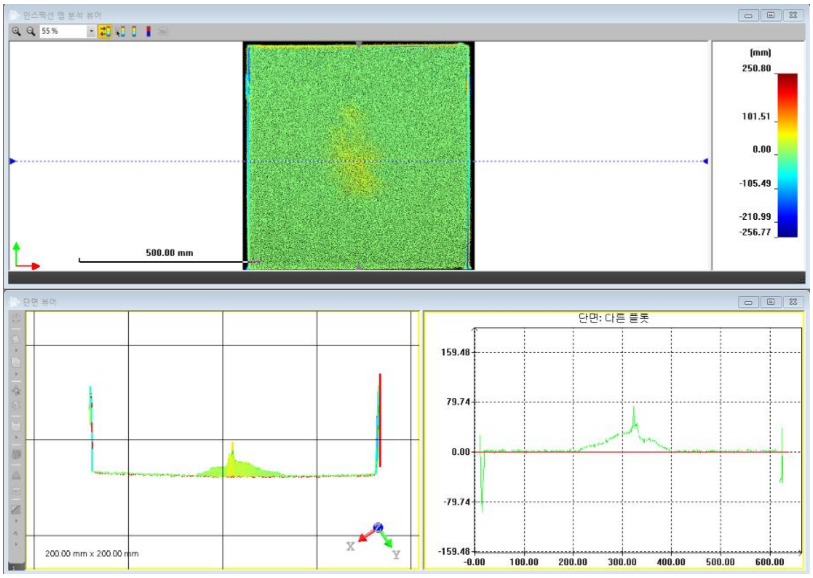

(a)

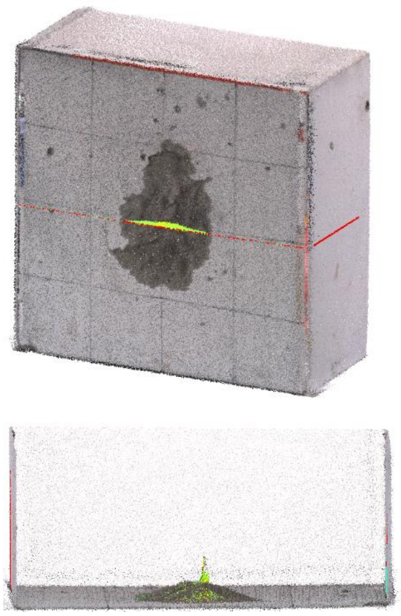

(b)

Figure C.16 3D Scanner analysis images; R0D37V850

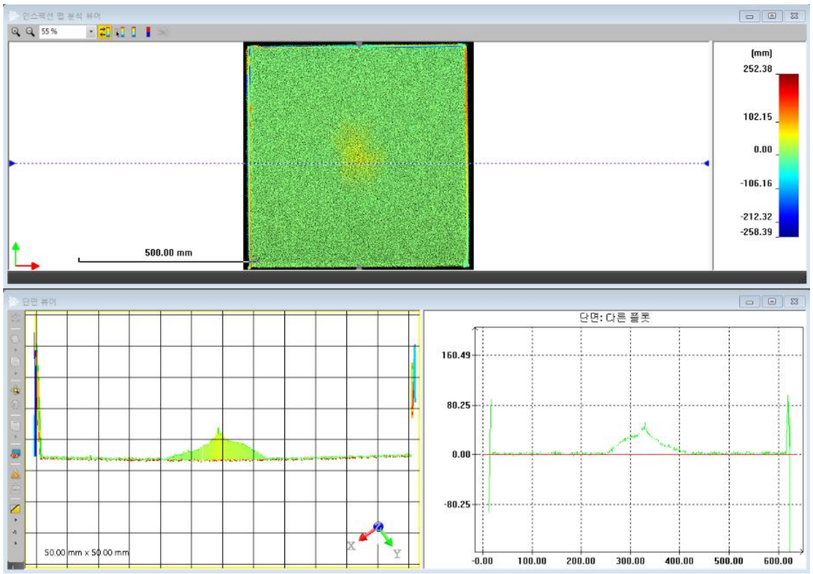

(a)

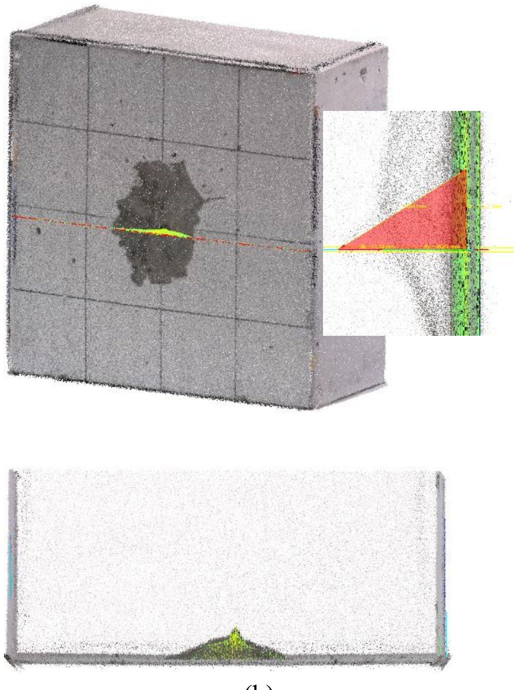

(b)

Figure C.17 3D Scanner analysis images; R1D37V850

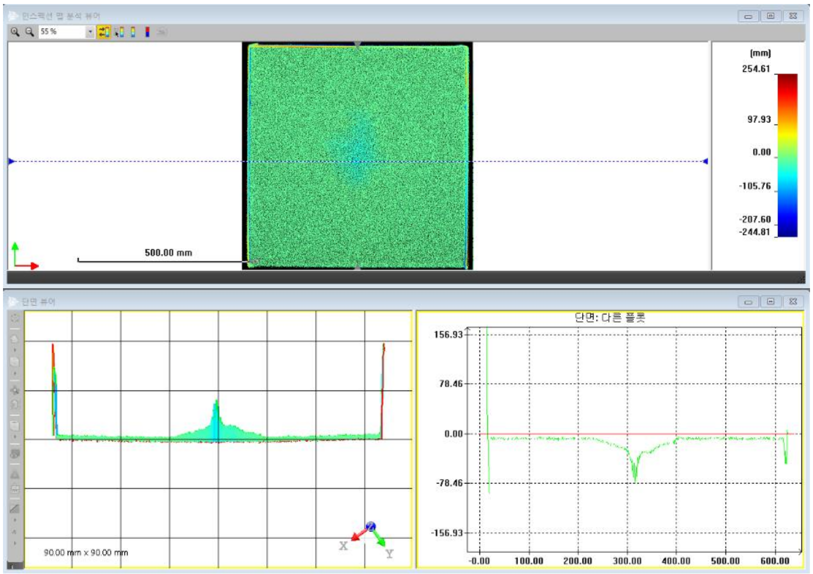

(a)

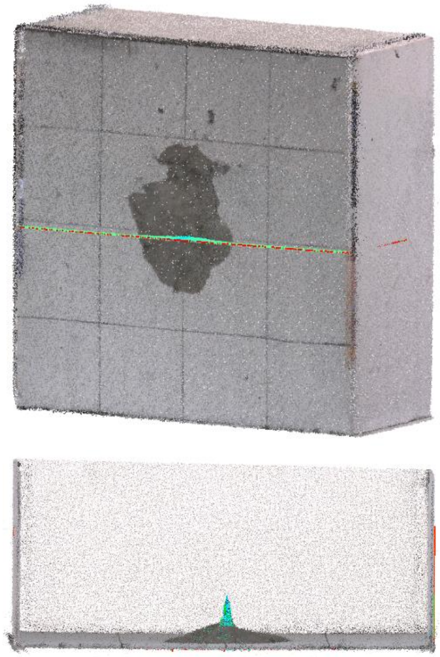

(b)

Figure C.18 3D Scanner analysis images; R2D37V850

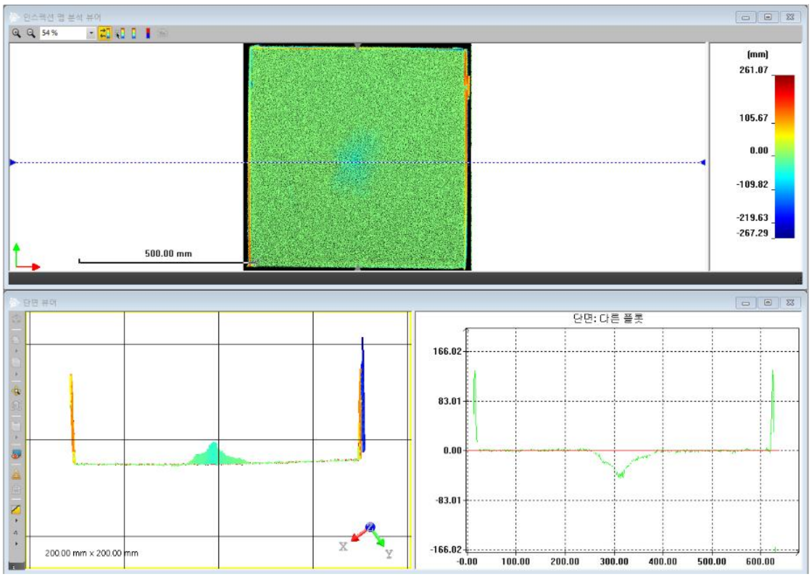

(a)

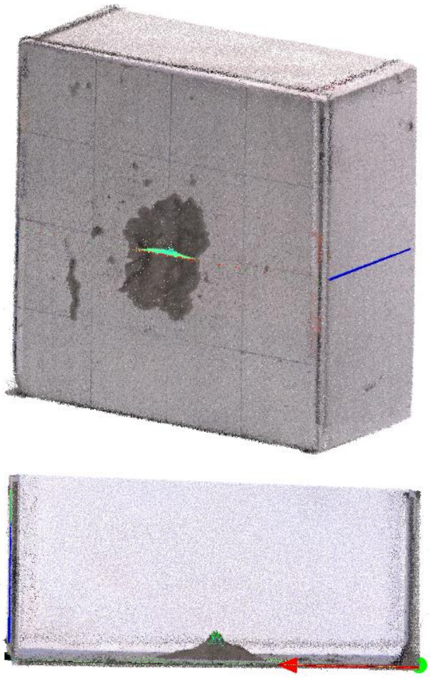
(b)

Figure C.19 3D Scanner analysis images; R3D37V850

국문초록

철근콘크리트 구조체의 방탄 성능에 철근보강이 미치는 영향

안 진 호

철근콘크리트(RC)는 높은 강도와 내구성으로 인해 널리 사용되는 건축재료이다. 그러나 철근콘크리트 구조물은 미사일 충돌이나 폭발 하중과 같은 고속 충격을 받으면 국부손상이 발생되기 쉽다. 이러한 국부손상은 구조물의 완전한 파괴를 발생하지 않더라도 내부 시설 및 인명에 상당한 피해를 입힐 수 있다. 따라서 국부손상을 고려해야하는 구조물의 경우 충격 하중 하에서 RC 구조물의 내충격 거동을 이해하는 것이 중요하다.

철근비는 RC 구조물의 거동에 영향을 미치는 주요 요소 중 하나이며, 이는 콘크리트 대비 철근의 비율을 의미한다. 일반적으로 철근비가 높을수록 철근의 양이 많아짐에 따른 RC 구조물의 휨성능이 향상되며, 이는 충격이나 폭발과 같은 극한하중에 대한 내구성에도 역시 일정한 영향을 미칠 것으로 예상되지만 주요 시설기준에서 제안하는 예측식에서는 철근비의 영향을 고려하고 있지 않다.

본 연구에서는 철근비와 충돌속도를 주요변수로 하여 RC 구조물에 강체발사체로 제작된 미사일이 고속으로 충돌하는 상황을 모사하여 일련의 충돌시험을 수행하였다. 그로부터, 관입깊이와 배면파쇄, 그리고 관통한계 등의 내충격성능에 대한 영향을 분석하였다. 이를 통해, 군사시설 및 원전구조물 설계에 활용되는 각종 설계기준에서 권장하는 기존 경험식들의 예측정확성에 대하여 실험적으로 검증하고, 실험결과를 바탕으로 철근비가 고려된 수정식을 제안하였다.

총 21 개의 시험체를 4 개의 서로 다른 철근비(0%, 1.6%, 2.5%, 3.4%)와 600mm x 600mm x 500mm 의 일정한 크기로 제작하였다. 시험체는 52 MPa 압축강도의 콘크리트와 D19 SD400 의 이형철근으로 제작하였다. 충돌실험은 서울대학교 EPTC 의 60 mm Single stage gas gun 을 사용하여 수행하였으며, 이는 헬륨 가스의 압력을 통해 D37, D12.7mm 의 강체발사체를 발사하였다. 이 때, 충돌속도는 550m/s-850m/s 범위에서 50m/s 간격으로 수행하였으며, 실험 후 관입깊이, 파쇄한계, 관통한계, 파괴모드 등의 데이터를 획득하였다.

그 결과 기존 경험식 중 Conwep 식의 예측정확도가 가장 높은 것으로 확인되었으며(Conwep 0.97, ACE 0.83, NDRC 0.73, UKAEA 0.72), 철근비가 높아질수록 RC 타겟의 내충격성능이 향상되는 것을 확인하였다. 구체적으로 관입깊이는 최대 11%, 평균 7%까지 감소했으며, 충돌후면의 균열 및 딱지 발생 면적과 시편의 질량

손실이 감소하였다. 또한, 철근비 증가에 따라 배면파쇄 및 관통한계속도도 50~70m/s 증가하였다.

이를 바탕으로 철근비에 대한 변수를 고려하는 국부손상 예측 수정식을 제안하였다. 그리고 제안한 예측모델의 유효성을 검증하기 위해 153 개의 기존 실험데이터와 LS-Dyna 프로그램을 활용한 유한요소해석을 통해 그 타당성을 검증하였다. 그 결과 제안한 수정식의 관입깊이에 대한 예측 정확도가 가장 우수함을 확인하였다(수정식 0.97, Conwep 0.83, ACE 0.74, NDRC 0.69, UKAEA 0.68).

본 연구에서는 시험체의 철근비와 발사체의 충돌속도에 따른 다양한 하중조건에서 철근콘크리트(RC) 타겟의 응답을 실험적, 해석적으로 분석하였다. 그 결과 철근비가 충격하중을 받는 RC 타겟의 내충격 성능에 상당한 영향을 미칠 수 있음을 보여주었으며, 본 연구에서 제안된 철근비를 고려한 경험적 공식의 수정식은 이러한 영향을 정량적으로 예측하는데 보다 유용한 자료로 활용될 수 있다.

주요어: 고속충돌실험, 철근콘크리트 구조체, 방탄 성능, 철근비, 국부손상예측 모델

학번: 2019-38662